

國立臺灣大學生物資源暨農學院生物環境系統工程學系

博士論文

Department of Bioenvironmental Systems Engineering

College of Bio-Resources and Agriculture

National Taiwan University

Doctoral Dissertation

衛星遙測應用於環境評估之研究

Application of Remote Sensing Techniques to  
Environmental Assessment



指導教授：鄭克聲 博士

Advisor: Ke-Sheng Cheng, Ph.D.

A Dissertation Presented to the Graduate School of National Taiwan  
University in Partial Fulfillment of the Requirements for the Degree of  
Doctor of Philosophy

中華民國 98 年 1 月

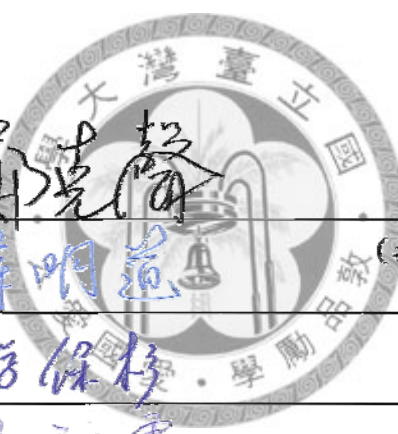
January, 2009

國立臺灣大學博士學位論文  
口試委員會審定書

衛星遙測應用於環境評估之研究  
Application of remote sensing techniques to environmental  
assessment

本論文係蘇元風君（學號：d93622004）在國立臺灣大學生物環境系統工程研究所完成之博士學位論文，於民國九十七年十二月二十四日承下列考試委員審查通過及口試及格，特此證明

口試委員：



鄭克聲 (簽名)  
蘇明燕 (指導教授)  
游保松  
陳祖憲  
黃文政  
系主任、所長 吳宏斌 (簽名)

## 謝誌

首先由衷感謝鄭克聲教授多年來的悉心指導與照顧。老師治學嚴謹、處事有方、待人親切的態度，都是值得學習的榜樣。本論文得以完成，除感謝鄭克聲教授在英文論文寫作上的指導與建議外，並感謝論文口試委員黃文政教授、蘇明道教授、游保杉教授與陳昶憲教授對於論文的寶貴意見與建議。

回首研究所期間，感謝領我入門的黃文政教授以及聯合指導的鄭克聲教授奠定獨立研究的基礎。在博士修課期間感謝生工系蘇明道教授、童慶彬教授、張斐章教授、土木系李天浩教授、財金系葉小蓁教授、顏月珠教授、郭瑞祥教授、生機系林達德教授、電機系林巍聳教授對於各專門知識的指導。

生工系就像一個大家庭，在攻讀博士期間給了我許多溫暖，感謝系辦陳秀美小姐、珍珠姐、軍廷大哥、吳明裕大哥與農工學會的佳芬與芳瑜，在生活上總是時時關懷照顧且不時提供協助。感謝研究室的每一位成員，很開心有你們的陪伴。感謝介倫學長與淑萍學姊對於後學的照顧，俊志學長對於研究的熱忱與幽默風趣的談吐值得晚輩學習。如真學姊有如姐姐一般關心、照顧每一位研究室成員，有妳在總是讓人安心且充滿歡樂。感謝會計總管漢蓓對於本論文文字修改的貢獻以及日常生活的照顧與提攜。感謝研究室的學弟妹們，維均對於研究室事務總是細心謹慎，宜珍個性開朗，與如真學姊是共同論戰俊志學長的最佳夥伴。方慈活潑大方，是球場上令人放心的夥伴。建文體貼直率、勤儉孝順是個值得信賴的軍人。感謝每位曾一同上山下海的夥伴們，建文、昀靜、世駿、品妤、以婷、淑媚、琮勛、哲瑜，有你們的幫忙才會有這本論文的產生。

最後感謝支持著我一路走來的父母親，默默為家庭付出的兄弟與大嫂，以及自大學時期一路陪伴我的女友，孟蓉，感謝有妳一起體驗生活的酸甜苦辣，一起努力朝屬於我們的幸福前進。

## Abstract

With the fast advancement of remote sensing technology, efficient and timely monitoring of environmental changes has become a reality. Among all kinds of environmental monitoring, climate changes and water resources are of most concern due to their extensive and potentially devastating impact. In this dissertation, feasibilities of three types of environmental monitoring – coastal water quality monitoring, effect of landcover changes on ambient air temperature, and forest drought monitoring using remote sensing techniques are investigated.

A multivariate water quality estimation model which can take into consideration the combined effect of various seawater constituents on water surface reflectance was proposed. The multivariate model was found to be superior to traditional univariate models. Changes in coverage ratio of individual landcover types within a NOAA pixel affect the NOAA-pixel average air temperature. Forest drought monitoring involves drought classification using NDVI derived from SPOT images. Seasonal variations of NDVI and ambient air temperature were assessed using multispectral SPOT images and NOAA thermal images.

**Keywords:** environment monitoring and assessment, remote sensing, water quality, multivariate model, landcover change, air temperature, drought.

## 摘要

隨著衛星遙測科技的進步，科學家可更有效率的監測與評估自然環境的變化。在各項環境監測中，全球氣候變遷與水資源議題廣受矚目，其所造成的影響廣泛而深遠，水資源議題(例如洪水、乾旱、水質)與全球氣溫升高均造成嚴重的災害與難以估計的損失。本文應用衛星於環境監測與評估分為三個部份，第一部份是以 SPOT 衛星監測員山子分洪隧道出口海域水質變化，評估分洪對於該海域水質的影響。研究中提出水體表面反射率反算程序，此程序適用於小區域尺度的遙測應用。傳統海域水質監測多以單變量模式建立推估式，然而水中所含物質例如懸浮顆粒、有機溶解物質與藻類等同時影響水體的光譜反射特性，吾人提出多變量模式可更有效推估水質變數，且符合水質變數物理特性，推估結果明顯優於單變量模式，最後繪製水質變數海域分布圖，供決策單位使用。第二部份，探討土地利用變遷對於週遭空氣溫度改變的評估。普遍而言，土地利用變遷趨勢反映區域環境生態特性，然而土地利用變遷影響週遭空氣溫度，本文以 AVHRR 影像推估地表溫度，提出新的方式評估 AVHRR 像元內土地利用類別比例對空氣溫度的影響。第三部份是評估乾旱造成林地植生生理特性改變的監測，使用 SPOT 衛星計算植生指標，提出以植生指標所定義的林地乾旱等級；同時以 NOAA 衛星探討林地於植生指標與地表溫度特徵空間的季節變動特性。環境評估須大量資料綜合評估，然而衛星資料提供決策者快速而全面的資訊，為決策與防治程序中有效率之工具之一。

關鍵詞：環境監測與評估、衛星遙測、水質、多變數模式、土地利用變遷、空氣溫度、乾旱。

# Contents

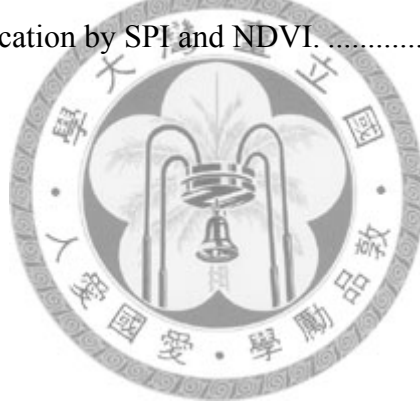
Abstract .....	i
摘要 .....	ii
Contents.....	iii
List of Tables.....	v
List of Figures .....	vi
Chapter 1 Introduction .....	1
1.1 Environmental monitoring and remote sensing techniques.....	1
1.2 Objectives .....	3
1.3 Structure.....	4
References.....	4
Chapter 2 Water quality monitoring using remotely sensed data.....	7
2.1 Introduction.....	7
2.2 Study area and materials.....	12
2.3 Retrieval of reflectance.....	15
2.4 Water quality estimation model assessment.....	26
2.5 Conclusions.....	35
References.....	38
Chapter 3 Assessing the effect of landcover changes on air temperature using remote sensing images .....	43
3.1 Introduction.....	43
3.2 Energy exchange between the land surface and the atmosphere .....	46
3.3 Study area and remote sensing data set.....	49
3.4 Land surface temperature estimation using NOAA images.....	49
3.5 Estimating the landcover-specific surface temperatures.....	54
3.6 Pixel-average air temperature estimation.....	61
3.7 Effect of landcover types on ambient air temperatures .....	65
3.8 Conclusions.....	72
References.....	73
Chapter 4 Forest Drought Monitoring.....	77
4.1 Introduction.....	77
4.2 Study Area and Materials.....	80
4.3 Drought indices.....	86

4.4 Results and discussion .....	90
4.4.1 Drought classification using SPOT image.....	91
4.4.2 Comparison between NDVI values derived from SPOT and AVHRR.....	95
4.4.3 Using AVHRR images for drought assessment .....	100
4.5 Conclusions.....	108
References.....	110
Chapter 5 Summary and future work.....	113
簡歷 .....	115



## List of Tables

Table 2-1 Univariate models.....	11
Table 2-2 Methods of water quality analysis.....	19
Table 2-3 Dates of water sampling and SPOT image acquisition.....	19
Table 2-4 Statistical properties of water quality variables.....	19
Table 2-5 Measurements of surface reflectance in the radiometric control area.....	27
Table 2-6 Scene reflectance calibration ratios of SPOT multispectral images.....	27
Table 2-7 Comparison of water quality estimation models.....	34
Table 3-1 Confusion matrix of landcover classification using training data.....	60
Table 3-2 Estimated landcover-specific surface and air temperatures (°C).....	60
Table 4-1 SPOT images used in this study.....	82
Table 4-2 Selected AVHRR images with less cloud cover.....	82
Table 4-3 Drought classification by SPI and NDVI.....	99





## List of Figures

Figure 2-1 Reflectance factor of water surface with varied Chlorophyll-a concentration.....	10
Figure 2-2 Study area in northern Taiwan.....	16
Figure 2-3 The radiometric control area. ....	16
Figure 2-4 Box plots of water quality data of no-diversion and post-diversion periods.....	17
Figure 2-5 Empirical relationships among different water quality parameters .....	18
Figure 2-6 Major paths of solar radiation reaching the satellite sensor. ....	22
Figure 2-7 Variable spectral radiometer (VSR) used for reflectance calibration.....	28
Figure 2-8 Calibrated wavelength-dependent RCA-average reflectances and band-average reflectances. ....	28
Figure 2-9 Scatter plots of water quality measurements versus band-dependent sea surface reflectances.....	31
Figure 2-10 Scatter plots of interval-average water quality measurements versus sea surface reflectances.....	31
Figure 2-12 Water quality measurements versus estimates.....	33
Figure 2-12 Spatial distribution of secchi disk depth. ....	36
Figure 2-13 Spatial distribution of turbidity. ....	36
Figure 2-14 Spatial distribution of total suspended solids.....	37
Figure 2-15 Photos of the Yin-Yang Sea area taken during water sampling campaigns. ....	37
Figure 3-1 Flowchart for assessing the effect of landcover changes on ambient air temperature. ....	45
Figure 3-2 Location map and pseudo-color SPOT image of the study area.....	50
Figure 3-3 Orthorectified aerial photos of the study area and the field sampling route. ....	50
Figure 3-4 (a) and (b): spatial variation of apparent surface temperatures derived from NOAA AVHRR images. Brighter pixels have higher apparent temperatures. (c) Area A with paddy and other vegetation. (d) Area B with residential and factory buildings.....	55
Figure 3-5 Results of landcover classification using multispectral SPOT images. ....	59
Figure 3-6 Comparison of pixel-average surface temperatures derived by the	

split window technique ( $T_{\text{SWT}}$ ) and estimated using landcover-specific surface temperatures ( $\bar{T}$ ).	59
Figure 3-7 Vertical temperature profiles of different landcover types.	63
Figure 3-8 Landcover-specific empirical relationship between the air temperature at 2m height ( $T_a$ ) and surface temperature ( $T_s$ ).	63
Figure 3-9 Schematic illustration of procedures of calculation of pixel-average air temperature over a NOAA pixel.	64
Figure 3-10 Empirical relationships between within-pixel coverage ratios of different landcover types and pixel-average air temperature.	69
Figure 3-11 Illustrative example of the prevalent, blind and forced conversion.	71
Figure 4-1 Northern Taiwan and the upstream basin of the Shihmen reservoir.	81
Figure 4-2 False-color representations of SPOT images from 1999 to 2004.	83
Figure 4-3 The proposed cloud screening procedure.	87
Figure 4-4 A schematic three-by-three window for texture calculation.	88
Figure 4-5 Example of cloud screening using the image acquired on 2004/02/10.	88
Figure 4-6 Schematic plot of VI-Ts space.	92
Figure 4-7 The SPI series for Gao Yi station with a 10-day period time scale from 1999 to 2004.	93
Figure 4-8 Classified SPOT image of the study area from 1999 to 2004.	96
Figure 4-9 NDVI histograms of the six years.	97
Figure 4-10 Trends of mean NDVI and cumulative SPI values.	97
Figure 4-11 Mean NDVI and cumulative SPI values.	98
Figure 4-12 Comparison of SPOT and AVHRR images (a) SPOT false-color image, (b) classified SPOT image, (c) NDVI map derived from AHVRR, (d) NDVI map derived from SPOT, (e) filtered NDVI map derived from SPOT.	101
Figure 4-13 The regression result of NDVI values derived from AHVRR images and filtered SPOT images.	102
Figure 4-14 Relationships between the NDVI value and the coverage ratios of vegetation and built-up areas.	102
Figure 4-15 Comparison of drought year and non-drought year for 12 months.	105
Figure 4-16 Vegetation dynamics of 2002 in VI-Ts space.	107
Figure 4-17 Vegetation dynamics of 2004 in VI-Ts space.	107

Figure 4-18 An upgraded version of the schematic plot of VI-Ts space..... 109



# Chapter 1 Introduction

## 1.1 Environmental monitoring and remote sensing techniques

Rapid development of remote sensing techniques helps scientists monitor environment resources in an efficient way. In natural resources, water resource and global warming are two major issues that are highly concerned. In the dissertation, three kinds of environment resources monitoring and assessment – water quality estimation, the effect of landcover change on air temperature, and drought effect on forest – are specifically discussed.

Water resource studies can be divided into two groups which mainly concern water quantity and quality. The former group measures and monitors the spatial distribution and the movement of water as it progresses through the hydrologic cycle; the latter group adopts remotely sensed data to estimate water quality and yields a distribution map of water quality. The later kind of application is usually difficult to obtain regional spatial information using *in situ* observations because the poor availability of *in situ* data limits the ability to assess the regional water quality. However, the advantages of remotely sensed satellite data, a repetitive coverage and synoptic view over the area of interest, are able to resolve this problem.

Besides water issues, air temperature is another important environmental factor directly affecting human life. In recent years, global warming and urbanization are considered as major cause of air temperature rising. Urbanization, in general, converts water bodies and vegetated surface into paved road or built-up area, coming in the wake of ambient air temperature rising. Cheng *et al.* (2008) and Yokohari *et al.* (2001) reported that change of land-cover/ land-use from paddy fields into buildup results in rise of ambient air temperature about 2-3°C. Land surface temperature can be

remotely sensed by detecting the thermal infrared electromagnetic radiation in the 3 – 14  $\mu\text{m}$  portion of the spectrum. The AVHRR (Advanced Very High Resolution Radiometer) operated by the NOAA (National Oceanic and Atmospheric Administration) is capable of calculating surface temperature by channel 4 and channel 5. Air temperature can further be calculated by an empirical relationship between land and air temperature. Concerning the details of how to assess the effect of landcover change on air temperature by multi-resolution remote sensing images, please refer to chapter three.

Drought is an insidious natural hazard that originates from a long-lasting deficiency of precipitation (Wilhite, 2005; Wilhite and Glantz, 1985). During drought progress, in the view of agriculture, insufficient water supply to vegetation results in reduction of yield. In the end part of drought progress, water shortage depletes the supply for domestic and industrial purposes and consequently results in vast cost of society and economy.

Insufficient water supply to vegetation will reduce the rate of photosynthesis process and keep stomata close from water loss. Consequently, air exchange between ambient and plant reduces and it will lead to higher canopy temperature. If air temperature remains high without sufficient water supply, chlorophyll contents will decrease. Drought could change surface bio-physical factors such as, land surface temperature and surface reflectance feature. Combination of these factors may provide useful information for quantitative monitoring of spatial and temporal distribution of drought (Ghulam *et al.*, 2007).

From the temporal viewpoint, drought development is a creeping process which makes detecting the onset time a tough task. From a spatial perspective, the influence

of drought is cumulative and wide-extended without a clear boundary. In the light of the advantages of synoptic spatial coverage and routine availability of satellite images, satellite remote sensing technique is the most appropriate tool to monitor drought effect on forest.

## 1.2 Objectives

The first objective is to estimate water quality by remote sensing data and assess the performance of the estimation models. An integration of remote sensing techniques and water sampling is worth pursuing, since water sampling in vast water bodies is time and labor consuming. We reviewed water quality estimation models using remote sensing images for inland, estuary and coastal water bodies. Most of the estimation models are applied for estimating single water quality variable. However, natural water bodies are mixture of water and other constituents including suspended solids, dissolved organic matters, zooplankton, etc. These constituents affect the reflectance in different wavelength of spectrum. Such wavelength-dependent combined effects should be reflected in water quality estimation model. Therefore, we proposed the multivariate model for water quality estimation by atmospheric-corrected multispectral reflectances. A scheme of retrieval of water surface reflectance with remote sensing images, can be used in a local scale area, is proposed. The concept of a multivariate model for water quality estimation can be applied to inland waters (pounds, lakes, reservoirs), estuary and coastal waters.

The second objective of this study is to quantitatively evaluate the effect of landcover types on ambient air temperature by remote sensing images and to understand the inter-relationships of different landcover types in a region. We showed the theoretical details of the land surface temperature estimation by remotely sensed

thermal infrared energy. We established the landcover-specific empirical relationship between the air temperature at 2m height and surface temperature for the study area. We proposed a new assessment method to evaluate the influence of landcover/landuse changes on ambient air temperatures.

The final objective is to assess drought effect on forest. Six SPOT (Satellite Pour l'Observation de la Terre) satellite images with a spatial resolution of 20 m, taken in each May from 1999 to 2004, are used to classify drought severity. The relationship between NDVI and SPI is established and the drought classification by NDVI is proposed. In addition, series of AVHRR (Advanced Very High Resolution Radiometer) images, taken in year 2002 and 2004, are used to assess seasonal dynamic of forest in the feature space of vegetation index and surface temperature.

### 1.3 Structure

This dissertation is composed of five parts. Chapter 1, introduction, gives readers the rough concept of environmental monitoring and assessment by remote sensing techniques. In this chapter, we clarify the selected issues of environmental monitoring discussed in the dissertation. Chapter 2 elaborates on the application of remote sensing images to water quality estimation. Chapter 3 describes how to assess the influence on ambient air temperature due to landcover change. Chapter 4 shows the application of multi-sensor to drought classification and assessment. The final part is summary and suggestions.

### References

- Cheng, K. S., Su, Y.F., Kuo, F.T., Hung, W.C., Chiang, J.L. (2008). Assessing the effect of landcover changes on air temperature using remote sensing images - A pilot study in northern Taiwan. *Landscape and Urban Planning*, 85, 85-96.
- Ghulam, A., Qin, Q., and Zhan, Z. (2007). Designing of the perpendicular drought

index. *Environmental Geology*, 52, 1045-1052.

Wilhite, D. A., and Glantz, M.H. (1985). Understanding the drought phenomenon: The role of definitions. *Water International*, 10(3), 111-120.

Wilhite, D. A., Ed. (2005). *Drought and water crisis: science, technology, and management issues*, Florida: CRC Press.

Yokohari, M., Brown, R.D., Kato, Y., Yamamoto, S. (2001). The cooling effect of paddy fields on summertime air temperature in residential Tokyo, Japan. *Landscape and Urban Planning*, 53, 17-27.



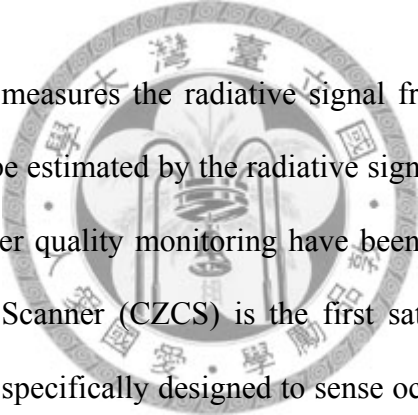




## Chapter 2 Water quality monitoring using remotely sensed data

### 2.1 Introduction

Conventional water quality monitoring depends on taking water sample *in situ* and analyzing it in laboratory. This procedure is not only time and labor consuming but to get distributed point data in a study area. Remotely-sensed data acquired from satellite can provide a cost-effective procedure for mapping water quality. The advantages of satellite data over conventional sampling procedures include repetitive coverage of an interesting area in a short period, and a synoptic view which provides almost instantaneous spatial data over the area of interest and is unobtainable by conventional procedure.

A circular diagram with a grey border containing the text '國立臺灣大學' (National Taiwan University) at the top and '水質監測' (Water Quality Monitoring) at the bottom. Inside the circle, there is a stylized illustration of a water droplet falling into a container, with a scale of justice and a balance scale positioned behind it, symbolizing the measurement and monitoring of water quality.

The sensor on satellite measures the radiative signal from a water surface to the sensor. Water quality can be estimated by the radiative signal. The studies of applying remote-sensed data to water quality monitoring have been proposed before 30 years ago. Coastal Zone Color Scanner (CZCS) is the first satellite launched by United States of America in 1978 specifically designed to sense ocean color. In the past three decades, many countries launched their own satellites for ocean color monitoring including SeaWiFS, MODIS etc. However, most of the ocean color observation satellites have spatial resolution of 1 km. The image data of this spatial scale limits the capability of monitoring inland water or near shore coastal water monitoring. Under this situation, a satellite with meter-scale spatial resolution, such as SPOT or Landsat, is more adapted for the application.

In general, water quality study can be divided into two categories, inland waters and ocean waters. Reservoirs and lakes are kind of inland waters which are easily affected by land-source substance. Suspended solid material carried in by upstream

inflow trapped in impounded water bodies may have long-lasting effect on impounded water quality. The constituents of inland waters are more complex than ocean waters. Besides suspended solid material, nutrients such as phosphate and nitrogen are other major constituents in impounded water bodies. Inland water quality will be affected by settling of sand particles and eutrophication. Therefore, in inland waters, the data ranges of water quality variables, such as total suspended solids, turbidity and chlorophyll-a concentration, are larger than those in ocean waters. There are many successful applications for inland water quality monitoring (Cheng and Lei, 2001; Giardino *et al.*, 2001; Huang, 2006; Kloiber *et al.*, 2002; Lin, 2005; Östlund *et al.*, 2001; Tan, 2006; Verdin, 1985; Wang *et al.*, 2004; Wu, 2001).

Morel and Prieur (1977) suggested that ocean waters can be divided into two cases according to constituents of ocean waters. The optical property of Case I ocean water is mainly affected by phytoplankton, also named as original open ocean water body. Non-algal particle (NAP) is the dominating factor in Case II ocean water. Near shore water and coastal water quality are constantly affected by upstream flow discharge which may contain high concentration sediments, especially during high-flow periods. Flushed by seawater, suspended solid material in coastal water may be mixed. Thus the characteristics of creeping impact and low immediate effect make it difficult to sense the emerging consequences which may be severely deleterious and irreversible on coastal ecosystem. For example, Tomascik and Sander (1985) and Hoegh-Guldberg *et al.* (2004) reported that change to coastal discharge is one of the most serious threats to coral reef ecosystem. Thus, understanding the long term effect of sediments carried in the upstream discharge on coastal water quality necessitates a routine monitoring scheme.

The optical properties of Case II water shows that when concentration of NAP is

higher the reflectances of visible band and near infrared band will arise; meanwhile, the influence of chlorophyll-a concentration on reflectance will decrease (Doxaran *et al.*, 2002; Lodhi *et al.*, 1997; Oyama *et al.*, 2007). Runquist *et al.* (1996) measured the reflectances of water surface with different chlorophyll-a concentration (156~277 $\mu\text{g/L}$ , 340~2190 $\mu\text{g/L}$ ). The spectral pattern shows that when chlorophyll-a concentration increases, the reflectances of green and near infrared bands increase with it; meanwhile, the reflectance of blue and red bands decrease (Figure 2-1). The spectral pattern is more regular under high chlorophyll-a concentration (340~2190 $\mu\text{g/L}$ ). The minor irregularities in the spectral pattern of lower chlorophyll-a concentration water surface probably occur because overall chlorophyll levels are very low (156~277 $\mu\text{g/L}$ ). In general, chlorophyll-a concentration in Case II water is extreme low (0~3 $\mu\text{g/L}$ ). The spectral pattern in Case II water may be more insignificant. It causes difficulties for monitor water quality by satellite data. Therefore, an appropriate monitoring model is necessary for a synoptic water quality monitoring.

Over the past three decades, the univariate models using only one water quality variable as dependent variable are proposed in many applications (summarized in Table 2-1). However, the water body is a mixture of seawater, suspended solids, color dissolved organic matters, and phytoplankton etc. The sea surface reflectance of a specific wavelength is interworked by those constituents. Some authors mentioned that the complexity of constituents in nature water interferes the spectral identification of water quality and affects the accuracy of estimation model. However, there is no solution suggested in the literature (Giardino *et al.*, 2001; Wang *et al.*, 2004).

Considering the wavelength-dependent combined effect must be reflected in the water quality estimation model, a multivariate model is proposed in this study. The

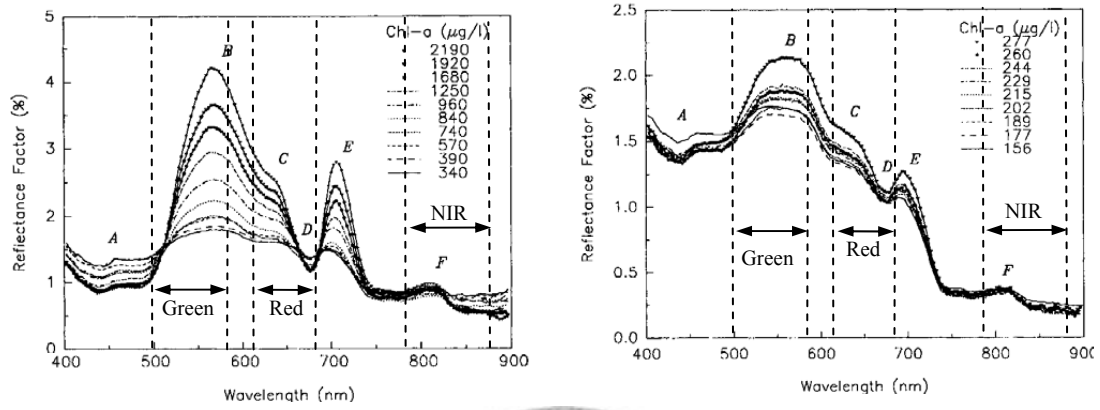


Figure 2-1 Reflectance factor of water surface with varied Chlorophyll-a concentration (Runquist, 1996).



Table 2-1 Univariate models.

Impounded waters				
Study Area	Sensor	Variable	Type	Reference
Flaming Gorge Reservoir	MS	<i>SSD, Chla</i>	Exp, Poly	Verdin, 1985
Moon Lake	MS	<i>TSS</i>	Poly	Ritchie and Cooper, 1988
Iseo Lake, Italy	TM	<i>SDD, Chla</i>	Poly	Giardino <i>et al.</i> , 2001
Yung-He-Shan Reservoir	SPOT	<i>SDD, Chla, Tb, TP</i>	Power, Poly	Wu, 2001
Erken Lake, Sweden	TM, CASI	<i>TSS, Chla</i>	Power, Poly	Östlund <i>et al.</i> , 2001
Four lakes in Finland	AISA*, MERIS	<i>SDD, Tb, Chla</i>	Poly	Koponen <i>et al.</i> , 2002
Lakes in Twin City	TM, MS	<i>SDD</i>	Exp	Kloiber <i>et al.</i> , 2002
Frisian Lakes	TM, SPOT	<i>TSS</i>	Exp	Dekker <i>et al.</i> , 2002
Shenzhen Reservoirs	TM	TOC, BOD, COD	Poly	Wang <i>et al.</i> , 2004
Tseng-Wen Reservoirs	FS II	<i>TSS, Turb, Chla</i>	Poly	Huang, 2006
Coastal water or Estuary water				
Study Area	Sensor	Variable	Type	Reference
San Francisco Bay	MS	<i>TSS, Tb</i>	Poly	Khorram, 1981
San Francisco Bay	Daedalus*	<i>Chla</i>	Poly	Catts <i>et al.</i> , 1985
Neuse River Estuary	MS	<i>SAL, Chla, Tb, TSS</i>	Poly	Khorram and Cheshire, 1985
Adriatic Sea	TM, CZCS	<i>TSS, Chla</i>	Power	Tassan, 1987
Swasea Bay	NERC*	<i>TSS, SAL</i>	Exp	Rimmer <i>et al.</i> , 1987
North Sea	AVHRR	<i>TSS</i>	Power	Prangma and Roozekrans, 1989
New Jersey' coast	TM	<i>Chla</i>	Poly	Bagheri and Dios, 1990
Augusta Bay	TM	<i>SDD, Tb, Chla, Temp</i>	Power	Khorram <i>et al.</i> , 1991
Western Australia Coast	TM	<i>SDD, Chla, Pha</i>	Exp, Poly	Lavery <i>et al.</i> , 1993
Western Australia Coast	TM	<i>SDD, Chla</i>	Exp	Pattiaratchi <i>et al.</i> , 1994
Indonesian seas	TM, SPOT	<i>TSS, PIG</i>	Exp	Populus <i>et al.</i> , 1995
Lakes and Coastal water in Finland	TM, MODIS, MERIS	<i>SDD, TSS, Chla, Turb</i>	Poly	Härmä, <i>et al.</i> 2001
Gironde Estuary	SPOT	<i>TSS</i>	Exp	Doxaran <i>et al.</i> , 2002
New York Harbor	TM, MODIS	<i>SDD, Chla</i>	Power	Hellweger <i>et al.</i> , 2004
Florida near-shore area	SeaWiFS	<i>Chla</i>	Power, Poly	Cannizzaro and Carder, 2006

\*: Airborne Sensor; MS: Landsat Multispectral Scanner; TM: Landsat Thematic Mapper; FS II: Formosat II

Exp: Exponential ; Poly: Polynomial;

*TSS*: Total Suspended Solid; *Tb*: Turbidity; *SDD*: Secchi Disk Depth; *Chla*: Chlorophyll-a concentration

Pha: Phaeophytin; TOC: Total Organic Carbon; BOD: Biochemical Oxygen Demand; COD: Chemical Oxygen Demand;

Temp: Temperature; TP: Total Phosphorus; SAL: Salinity;

atmospheric corrected water surface reflectances of SPOT images are the independent variables in proposed model. The water quality variables selected in this study are secchi disk depth (*SDD*), turbidity (*Tb*), total suspended solids (*TSS*) and chlorophyll-a concentration (*Chla*). *SDD* is a measure of water transparency in seawaters and is related to water turbidity and the radiance onto water surface. Turbidity and total suspended solids are the indicators to show organic and inorganic particle amount in a water body. The chlorophyll-a concentration is well-correlated to the amount of phytoplankton. These four variables are commonly used to assess the water quality in Case II waters.

## 2.2 Study area and materials

Yuan-Shan-Tzu (YST) Diversion Tunnel is designed to divert flood flow from the upper Keelung River Basin to a discharge outlet at the northern tip of Taiwan. The YST tunnel, completed in 2003 with a diameter of 12 m and 2.48 km in total length, is capable of diverting approximately 81% ( $1,310 \text{ m}^3/\text{s}$ ) of the 200-year flood flow ( $1,620 \text{ m}^3/\text{s}$ ) at a cross section near the inlet of YST tunnel. The coastal area near the outlet of the Yuan-Shan-Tzu Diversion Tunnel in northern Taiwan is the typical Case II water and is selected as study area in this article (Figure 2-2). A radiometric control area (RCA) of approximately  $30\text{m}\times 60\text{m}$  is selected in Figure 2-2 for spectral reflectance calibration. The RCA is a horizontal paved open area with homogeneous and stationary surface reflectance and no adjacent obstruction (see Figure 2-3).

During July to November of 2007, a few water sampling campaigns were conducted in a coastal area of tunnel outlet. The sampling dates and relevant storm information are shown in Table 2-2. Water samples were taken within 0 – 20 cm range below the sea surface at eight locations (see Figure 2-2) during each sampling

campaign. Global positioning systems were used to guide the sampling vessel to the desired sampling locations. Considering the west-to-east surface current direction of the season, the sampling area extends from a little northwest of the outlet to about 2 km to the east of the outlet. Sampling point 4 is located within an area known as the Yin-Yang Sea. Geology of the near Yin-Yang Sea area has a large amount of pyrite that does not dissolve easily in water. The Yin-Yang Sea area, just offshore from an old metal mining township, frequently receives runoff containing high iron ion concentration, making the sea surface visually distinct. Secchi disk depth and turbidity were measured *in situ* and water samples were taken to the Environmental Chemistry Lab at the National Taiwan University for analyses of total suspended solids and chlorophyll-a concentration.

The water quality analysis methods used in this study are proposed by the Environmental Analysis Laboratory, EPA, Executive Yuan, R.O.C. Secchi disk depth records the depth that a naked eye cannot see the secchi disk in water. Turbidity is measured by a portable turbidity meter (2100P, HACH, USA) with unit of Nephelometric Turbidity Unit (NTU). Secchi disk depth and turbidity are measured *in situ* during each sampling campaign. Total suspended solids is determined by pouring a carefully measured volume of water through a pre-weighted glass-fiber filter (GF/F, 47mm diameter, 0.7 $\mu$ m pore size), then weighting the filter again after drying to remove all water. The gain in weight divided the volume of sample water is the measure of total suspended solids with unit of mg/l. Chlorophyll-a can be extracted by ethanol from a pre-weighted glass-fiber filter which volume of water already poured through, then measure the absorptions at 665 and 750nm. Chlorophyll-a concentration can be calculated by the absorptions at 665 and 750nm. The methods used for water quality variables are listed in Table 2-2.



A few multispectral images from SPOT satellites with acquisition dates close to the dates of sampling campaign were also collected (see Table 2-3). During and immediately after the Wipha and Krosa typhoon events, the study area were almost completely under cloud cover, and thus no SPOT images were collected. The multispectral SPOT images include images of three spectral bands – green (0.5 – 0.59  $\mu\text{m}$ ), red (0.61 – 0.68  $\mu\text{m}$ ), and near infrared (0.78 – 0.89  $\mu\text{m}$ ), with pixel resolution of 20 m for SPOT-4 or 10 m for SPOT-5.

Table 2-4 summarizes statistical properties of the three water quality variables. Two sampling campaigns (09/20/2007 and 10/08/2007) took place one day after activation of flood diversion. Comparison of the water quality data of the no-diversion and post-diversion periods is shown in Figure 2-4. Differences in medians and ranges of *TSS*, *Tb* and *SDD* are apparent. For example, median of *SDD* drops from 6.8 m of the no-diversion period to 3.8 m of the post-diversion period, whereas median of *TSS* increases from 1.6 mg/L of the no-diversion period to 5.2 mg/L of the post-diversion period. Also, excluding the outliers, the ranges of the water quality variables of the no-diversion and post-diversion periods are almost non-overlapping.

Before pursuing establishment of water quality estimation models using the water quality data and remote sensing images, we conducted a careful check on measurements of water quality variables. The purpose of such data check is to screen out data which might have been contaminated by inappropriate sampling of water samples or erroneous measurement in the lab. In general, the Secchi disk depth, total suspended solids, and turbidity are inter-related, as showed in following equations and demonstrated in Figure 2-5. The points marked by dashed-circles are significantly inconsistent with such correlation, and thus are excluded in subsequent analyses.

Similar relationships between the Secchi disk depth and the turbidity are showed in few researches (Gao *et al.*, 2008; Gryson *et al.*, 1996; Koponen *et al.*, 2002; Lewis, 1996; Pavanelli and Bigi, 2005).

$$\ln(SDD) = 1.71 - 0.5 \ln(Tb) \quad (R^2 = 0.71) \quad (2-1a)$$

$$\ln(TSS) = 0.86 + 0.77 \ln(Tb) \quad (R^2 = 0.52) \quad (2-1b)$$

$$\ln(TSS) = 2.97 - 1.21 \ln(SDD) \quad (R^2 = 0.45) \quad (2-1c)$$

### 2.3 Retrieval of reflectance

Mobley (1994) described the optical properties of natural water are conveniently divided into two mutually exclusive classes: inherent and apparent. Inherent optical properties (IOP's) are those properties that are independent of the ambient light field. The two fundamental IOP's are the absorption coefficient and the volume scattering function which can quantitatively describe the solar radiance transfer process. Apparent optical properties (AOP's) are those properties that depend both on the medium and on the geometric structure of the ambient light field, and that display enough regular features and stability to be useful descriptors of the water body. The spectral remote-sensing reflectance is one of the most important AOP. The spectral remote-sensing reflectance, hereafter which is short as reflectance, is used to construct the experience model in this study.

In satellite remote sensing application, the major paths of solar radiation reaching the sensor are depicted in Figure 2-6. The primary solar radiance (path I) accounts for the solar irradiance onto the target object, and then reflected back to the atmosphere, and finally arrives at the sensor. The downwelled solar radiance (path II) is the atmospheric scattered solar radiance incident on and reflected away from the target object before reaching the sensor. The upwelled solar radiance (path III) is the radiance scattered by the atmosphere and directly reaching the sensor without getting

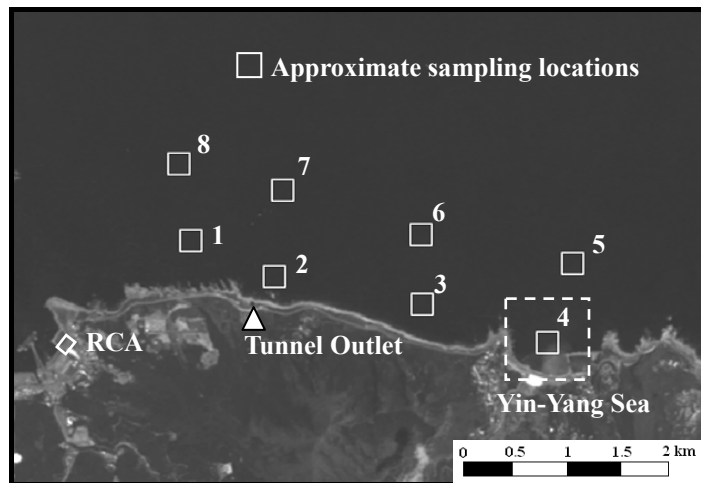
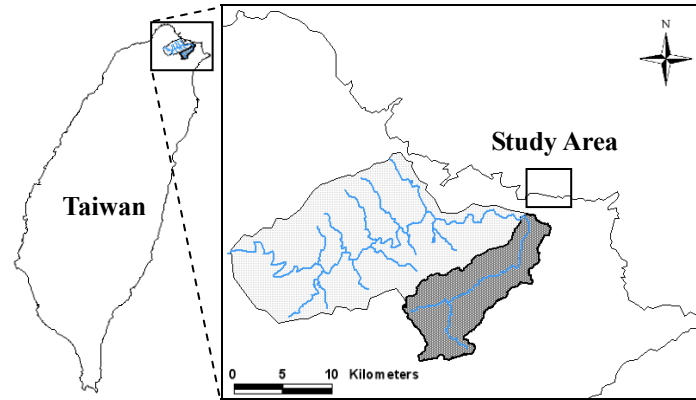


Figure 2-2 Study area in northern Taiwan (The numbers represent the sample sites).



Figure 2-3 The radiometric control area (RCA).

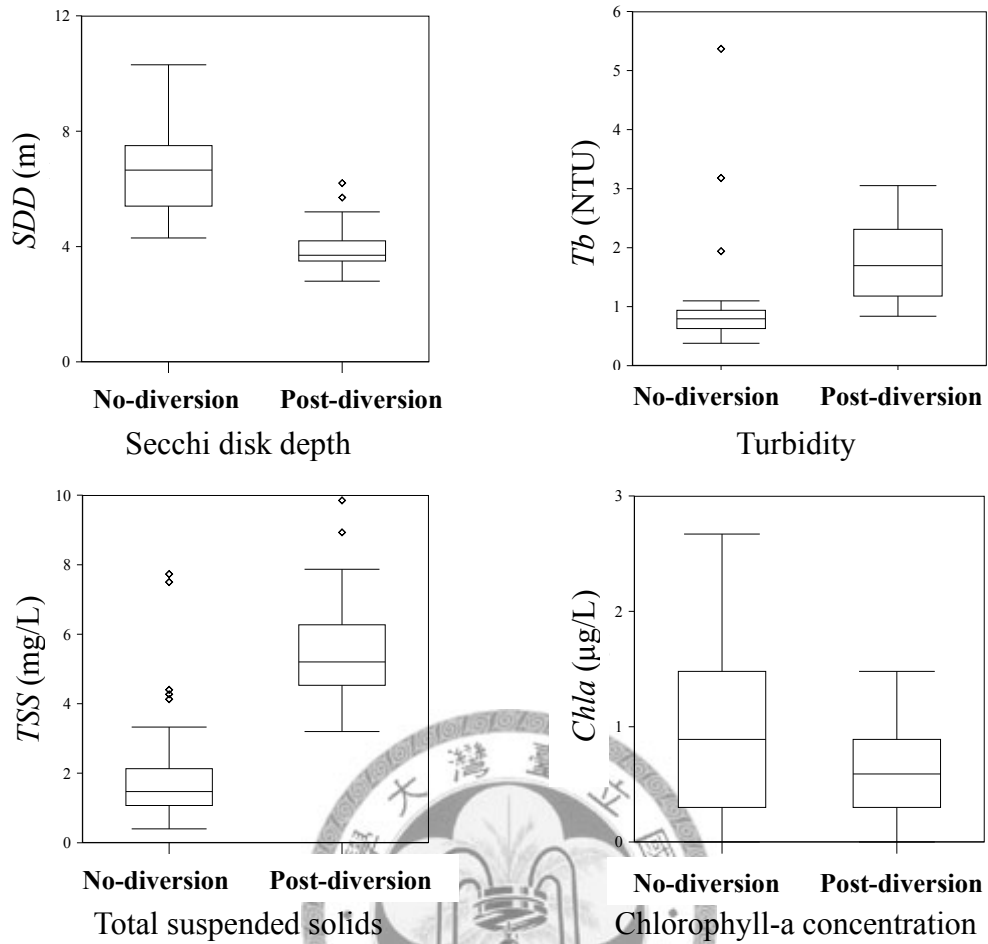


Figure 2-4 Box plots of water quality data of no-diversion and post-diversion periods.

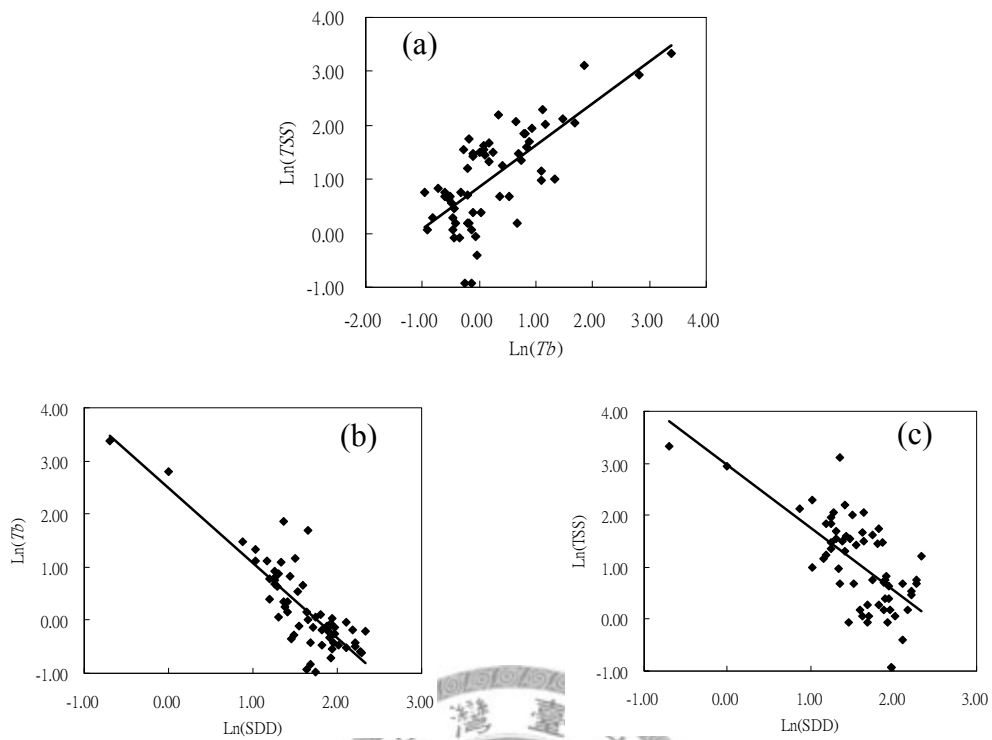


Figure 2-5 Empirical relationships among different water quality parameters (a)  $Tb$  vs.  $TSS$  (b)  $SDD$  vs.  $Tb$  (c)  $SDD$  vs.  $TSS$ .

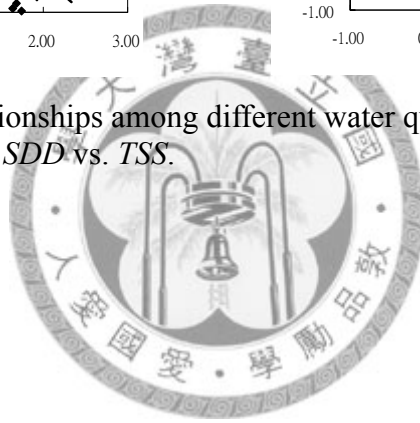


Table 2-2 Methods of water quality analysis.

Water quality variable	Methods	Unit
Chlorophyll-a conc.	NIEA E508.00B	µg/L
Turbidity	NIEA W219.52C	NTU
Secchi disk depth	NIEA W221.50A	m
Total suspended solid	NIEA W210.57A 103 <sup>0</sup> C-105 <sup>0</sup> C	mg/L

Table 2-3 Dates of water sampling and SPOT image acquisition.

Sampling date	SPOT image acquisition date	Relevant storm events	Volume of diverted flow (m <sup>3</sup> )
7/02/2007	7/04/2007 (SPOT-4)	No storm	0
7/18/2007	7/19/2007 (SPOT-4)	No storm	0
8/15/2007	NA <sup>a</sup>	No storm	0
8/23/2007	8/23/2007 (SPOT-5)	Typhoon Sepat (8/16~8/19)	0
9/07/2007	9/03/2007 (SPOT-5)	No storm	0
9/20/2007	NA <sup>a</sup>	Typhoon Wipha <sup>b</sup> (9/17~9/19)	1,051,200
10/08/2007	NA <sup>a</sup>	Typhoon Krosa <sup>b</sup> (10/4~10/7)	16,133,400
11/14/2007	NA <sup>a</sup>	No storm	0

<sup>a</sup>Satellite images were not collected due to high percentage of cloud cover.

<sup>b</sup>Flow diversion activated.

Table 2-4 Statistical properties of water quality variables.

	Mean	Standard deviation	Maximum	Minimum
Secchi disk depth ( <i>m</i> )	5.40	2.13	10.30	0.50
Turbidity ( <i>NTU</i> )	2.20	4.22	29.50	0.38
Total suspended solid ( <i>mg/L</i> )	4.36	4.97	28.00	0.40
Chlorophyll-a conc. ( <i>µg/L</i> )	0.79	0.69	2.67	0.00

Total number of samples: 61

in contact with the target object.

Mobley (1994) defined the spectral remote-sensing reflectance, in this study is called reflectance, as the water-leaving radiance divided by irradiance onto water surface. Spectral remote-sensing reflectance, which is abbreviated as reflectance in this study, is presented as:

$$R_{rs}(\theta, \phi_S, \phi_Z, \sigma, \lambda) = \frac{L(\theta, \phi_S, \phi_Z, \sigma, \lambda)}{E(\lambda)} \quad (2-2)$$

where

- $R_{rs}$  = the water-leaving radiance
- $L$  = the water-leaving radiance
- $\theta$  = view angle in sensor-target direction
- $\phi_Z$  = sensor azimuth angle
- $\phi_S$  = sun azimuth angle
- $\sigma$  = the sun angle
- $E$  = the solar irradiance reaching water surface
- $\lambda$  = wavelength in  $\mu\text{m}$ .

The amount of solar radiance reaching the satellite sensor can be expressed as:

$$L_s(\theta, \phi_Z, \lambda) = L(\theta, \phi_S, \phi_Z, \sigma, \lambda) \cdot \tau_2(\lambda) + L_u(\theta, \phi_Z, \lambda) \quad (2-3)$$

where  $\tau_2$  is the atmospheric transmittance along the target-sensor path and  $L_u$  is upwelled solar radiance ( also known as path radiance). The water-leaving radiance can further expressed as:

$$L(\theta, \phi_S, \phi_Z, \sigma, \lambda) = E_{Top} \cdot \tau_1(\lambda) \cdot \cos \sigma \cdot \frac{R_{rs}(\theta, \phi_S, \phi_Z, \sigma, \lambda)}{\pi} + F \cdot E_D(\lambda) \cdot \frac{R_{rs}(\lambda)}{\pi} \quad (2-4)$$

where

- $E_{Top}$  = the exoatmospheric solar irradiance
- $\tau_1$  = the atmospheric transmittance along the sun-target path
- $E_D$  = the downwelled irradiance from the sky dome onto the target

$F$  = the obstruction factor.

The obstruction factor in equation (2-4) accounts for the proportion of irradiance that may be obstructed by adjacent objects or surface slope of the target. If the target object is on a horizontal surface and free of adjacent object obstruction, the factor  $F$  equals 1. It is also worthy to note that the sun and view angles are defined with reference to the normal of the target surface. If the target is located on a slope, the sun and view angles will need to be adjusted accordingly. Readers are referred to Schott (1997) for detailed calculation of solar radiances arriving at the sensor.

The reflectance  $R_{rs}(\theta, \phi_s, \phi_z, \sigma, \lambda)$  varies with spectral wavelength and orientation angles. If the target object is assumed to be a diffuse reflector with a constant reflectance  $R_{rs}(\lambda)$  in all directions, we then have

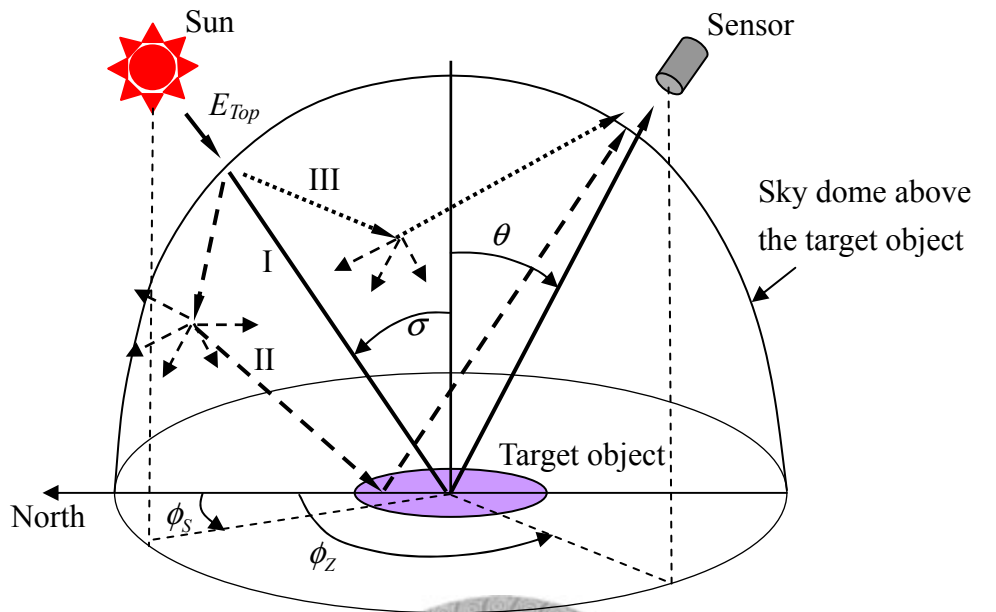
$$L_s(\theta, \phi_z, \lambda) = (E_{Top} \cdot \tau_1(\lambda) \cdot \cos \sigma + F \cdot E_D(\lambda)) \cdot \frac{R_{rs}(\lambda)}{\pi} \cdot \lambda_2(\lambda) + L_u(\theta, \phi_z, \lambda) \quad (2-5)$$

On the right hand side of the above equation, only the reflectance  $R_{rs}(\lambda)$  represents the physical property of the target surface. The upwelled radiance  $L_u$  does not even get into contact with the target.

Environmental monitoring using remote sensing images often requires derivation of physical properties (reflectance, for example) of the target objects from satellite images. Unfortunately, the upwelled radiance  $L_u$ , the atmospheric transmittance  $\tau_1$  and  $\tau_2$ , the downwelled irradiance  $E_D$ , and the exoatmospheric solar irradiance  $E_{Top}$  are generally not available for most applications, and we have to resort to other means for estimation of the reflectance.

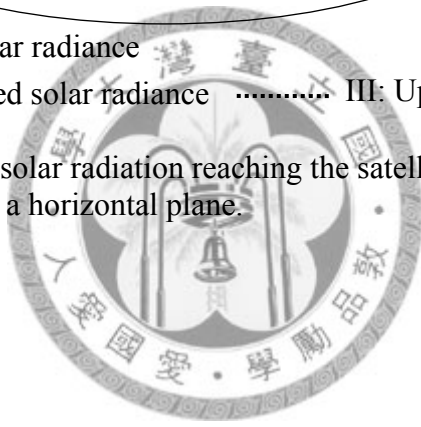
For most local-scale environmental monitoring applications,  $L_u$ ,  $\tau_1$ ,  $\tau_2$ ,  $E_D$ , and





- I: Primary solar radiance
- - - - II: Downwelled solar radiance
- ..... III: Upwelled solar radiance

Figure 2-6 Major paths of solar radiation reaching the satellite sensor. The target object is assumed to be on a horizontal plane.



$E_{Top}$  can be assumed constant (or spatially invariant) within the study area. While on the contrary, the sun angle  $\sigma$  and the obstruction factor  $F$  are dependent on the surface slope of the target, and the reflectance  $R_{rs}(\lambda)$  is dependent on surface cover of the earth. Their values may vary from pixel to pixel within a scene. If only pixels on horizontal surface and free of adjacent obstruction are considered ( $F = 1$ ), Equation (2-5) may be expressed as:

$$\begin{aligned}
 L_S(\theta, \phi_Z, \lambda) &= (E_{Top} \cdot \tau_1(\lambda) \cdot \cos \sigma + E_D(\lambda)) \cdot \frac{R_{rs}(\lambda)}{\pi} \cdot \lambda_2(\lambda) \\
 &+ L_u(\theta, \phi_Z, \lambda) \\
 &= k_1 \cdot R_{rs}(\lambda) + k_2
 \end{aligned} \tag{2-6}$$

where

$$\begin{aligned}
 k_1 &= (E_{Top} \cdot \tau_1(\lambda) \cdot \cos \sigma + E_D(\lambda)) \cdot \frac{\tau_2(\lambda)}{\pi} \\
 k_2 &= L_u(\theta, \phi_Z, \lambda)
 \end{aligned}$$

A common practice dealing with the upwelled radiance  $L_u(\theta, \phi_Z, \lambda)$  in satellite remote sensing is the dark object subtraction (DOS) method (Chavez, 1988; Cheng and Lei, 2001; Teng *et al.*, 2008). The basic concept of the DOS method is to identify very dark features within the scene. The minimum scene radiance is set to be the upwelled radiance based on the assumption that it represents the radiance from a pixel with near zero reflectance. If the minimum scene radiance is subtracted from the radiance of each individual pixel, the processed image is then assumed free of atmospheric scattering effect.

After removing the upwelled radiance  $L_u(\theta, \phi_Z, \lambda)$  using the DOS method, the DOS-adjusted radiance  $L'_S(\theta, \phi_Z, \lambda)$  is linearly related to the surface reflectance, i.e.:

$$L'_S(\theta, \phi_Z, \lambda) = L_S(\theta, \phi_Z, \lambda) - L_u(\theta, \phi_Z, \lambda) = k_1 \cdot R_{rs}(\lambda) \tag{2-7}$$

Based on the linear relationship between  $L'_S$  and  $R_{rs}(\lambda)$ , we derive a surface

reflectance estimation scheme through reflectance calibration in a radiometric control area (RCA).

In this study a radiometric control area of approximately 30 m × 60 m was chosen for spectral reflectance calibration. The RCA is a horizontal paved open area with homogeneous and stationary surface reflectance and no adjacent obstruction (see Figure 2-3). It is located in a restricted and free of public access harbor area. The wavelength-dependent surface reflectance of RCA is then calibrated using a variable spectral radiometer (VSR) which is equipped with two spectral-variable filters capable of detecting spectral radiances in various 7 nm-wide windows within the 0.40 – 0.72 μm and 0.65 – 1.1 μm ranges respectively (Figure 2-7). The VSR was moved around within the radiometric control area taking multispectral images. When taking images within the RCA, a standard reflectance disk which has been pre-calibrated to have  $R_{rs}^{Disk}(\lambda) \approx 1$  over the 0.25 – 1.1 μm wavelength range was also placed within the viewing area. Reflectance of the radiometric control area is then calculated as the ratio of average radiance from RCA to average radiance from the standard reflectance disk, i.e.:

$$R_{rs}^{RCA}(\lambda) = \frac{\bar{L}_S^{RCA}}{\bar{L}_S^{Disk}} \cdot R_{rs}^{Disk}(\lambda) \quad (2-8)$$

where  $R_{rs}^{RCA}(\lambda)$  is the reflectance of RCA, and  $\bar{L}_S^{RCA}$  and  $\bar{L}_S^{Disk}$  are respectively average radiances received at VSR sensor from the RCA surface and from the standard reflectance disk. For RCA reflectance calibration, the effect of upwelled radiance can be neglected since the VSR is placed near the ground surface. Table 2-5 lists measurements of surface reflectance in the radiometric control area and area average reflectance with respect to various spectral wavelengths are also shown in

Figure 2-8. The RCA-average reflectance corresponding to green, red and near infrared SPOT spectral bands (hereafter referred to as the RCA band reflectances) are calculated to be 0.097, 0.113, and 0.161%, respectively. The RCA band reflectances are considered constant since the land surface condition within the RCA is relatively homogeneous and stationary.

Assuming the sea surface is horizontal, the DOS-adjusted radiances of a pixel  $A$  in the RCA and a pixel  $B$  on the sea surface are respectively expressed by:

$$L_S^A(\theta, \phi_Z, \lambda) = k_1 \cdot R_{rs}^A(\lambda) \quad (2-9)$$

$$L_S^B(\theta, \phi_Z, \lambda) = k_1 \cdot R_{rs}^B(\lambda) \quad (2-10)$$

where  $R_{rs}^A$  and  $R_{rs}^B$  are the reflectance of RCA pixel  $A$  and sea surface pixel  $B$ , respectively. Combining Equation (2-9) and Equation (2-10) and rewriting the reflectance of sea surface pixel  $B$  as:

$$R_{rs}^B(\lambda) = \left[ \frac{R_{rs}^A(\lambda)}{L_S^A(\theta, \phi_Z, \lambda)} \right] \cdot L_S^B(\theta, \phi_Z, \lambda) \quad (2-11)$$

Practically,  $L_S^A(\theta, \phi_Z, \lambda)$  and  $R_{rs}^A(\lambda)$  are respectively replaced by the average radiance and reflectance of RCA, and

$$R_{rs}^B(\lambda) = \left[ \frac{R_{rs}^{RCA}(\lambda)}{\bar{L}_S^{RCA}(\theta, \phi_Z, \lambda)} \right] \cdot L_S^B(\theta, \phi_Z, \lambda) \quad (2-12)$$

where  $\bar{L}_S^{RCA}(\theta, \phi_Z, \lambda)$  represents the average value of DOS-adjusted radiances within RCA and  $R_{rs}^{RCA}(\lambda)$  is the RCA band reflectance. The reflectance calibration ratio

$\frac{R_{rs}^{RCA}(\lambda)}{\bar{L}_S^{RCA}(\theta, \phi_Z, \lambda)}$  in above equation may vary with SPOT scenes since  $\bar{L}_S^{RCA}(\theta, \phi_Z, \lambda)$

varies due to scene variations in orientation angles and atmospheric transmittance.

Table 2-6 summarizes reflectance calibration ratios of individual SPOT multispectral images.

## 2.4 Water quality estimation model assessment

In order to map the spatial distribution of water quality variables using remote sensing images, it is necessary to establish water quality estimation models based on reflectance of sea surface. A few simple or multiple regression models have been proposed in the literature (Bagheri and Dios, 1990; Cannizzaro and Carder, 2006; Catts *et al.*, 1985; Giardino *et al.*, 2001; Härmä *et al.*, 2001; Hellweger *et al.*, 2004; Huang, 2006; Khorram, 1981; Khorram and Cheshire, 1985; Khorram *et al.*, 1991; Kloiber *et al.*, 2002; Lavery *et al.*, 1993; Oyama *et al.*, 2007; Pattaratchi *et al.*, 1994; Polulus *et al.*, 1995; Prangma and Roozkrans, 1989; Rimmer *et al.*, 1987; Ritchie and Cooper, 1988; Tassan, 1987; Wang *et al.*, 2004; Wu, 2001) and most of these models fall into one of the following forms:

$$\log Y = c_0 + \sum_{i=1}^k c_i \log X_i \text{ (or equivalently, } Y = a_0 \prod_{i=1}^k X_i^{a_i} \text{)} \quad (2-13a)$$

$$\log Y = c_0 + \sum_{i=1}^k c_i X_i \quad (2-13b)$$

$$Y = c_0 + \sum_{i=1}^k c_i X_i \quad (2-13c)$$

where  $Y$  represents a water quality variable and  $X_i$  can be reflectance of a specific spectral band, ratio of reflectances of different spectral bands, or other arithmetic calculation of band reflectances.

In order to choose appropriate models for water quality mapping, we first examined scatter plots of water quality measurements versus band-dependent sea surface reflectances, as shown in Figures 2-9(a)-(d). Although the data points are widely dispersed, particularly in lower measurement ranges, measurements of turbidity and

Table 2-5 Measurements of surface reflectance in the radiometric control area.

Wavelength ( $\mu\text{m}$ )	Sampling points								
Green	1	2	3	4	5	6	7	8	9
0.50	0.091	0.073	0.088	0.088	0.074	0.076	0.069	0.101	0.094
0.51	0.094	0.076	0.091	0.090	0.076	0.079	0.071	0.104	0.096
0.52	0.097	0.079	0.094	0.093	0.079	0.081	0.073	0.107	0.100
0.53	0.100	0.081	0.097	0.096	0.081	0.084	0.075	0.110	0.103
0.54	0.103	0.083	0.099	0.098	0.083	0.086	0.076	0.113	0.106
0.55	0.106	0.086	0.103	0.101	0.086	0.089	0.079	0.117	0.110
0.56	0.109	0.088	0.106	0.104	0.088	0.091	0.080	0.120	0.113
0.57	0.112	0.090	0.108	0.107	0.090	0.093	0.082	0.123	0.116
0.58	0.114	0.092	0.110	0.109	0.092	0.095	0.083	0.125	0.118
0.59	0.117	0.094	0.113	0.111	0.094	0.097	0.084	0.127	0.120
0.60	0.119	0.095	0.114	0.113	0.095	0.099	0.086	0.129	0.122
Red									
0.61	0.121	0.097	0.116	0.114	0.096	0.100	0.087	0.131	0.124
0.62	0.122	0.097	0.117	0.115	0.097	0.101	0.087	0.132	0.125
0.63	0.123	0.098	0.118	0.116	0.098	0.101	0.088	0.133	0.126
0.64	0.124	0.099	0.119	0.118	0.100	0.103	0.089	0.134	0.127
0.65	0.125	0.100	0.119	0.118	0.100	0.103	0.089	0.135	0.128
0.66	0.126	0.101	0.120	0.119	0.101	0.104	0.090	0.136	0.129
0.67	0.127	0.102	0.121	0.120	0.102	0.105	0.091	0.137	0.130
0.68	0.129	0.103	0.122	0.121	0.103	0.106	0.092	0.138	0.131
Near IR									
0.79	0.263	0.205	0.241	0.247	0.205	0.205	0.180	0.290	0.284
0.80	0.245	0.189	0.225	0.229	0.190	0.189	0.167	0.270	0.258
0.81	0.223	0.171	0.204	0.208	0.173	0.171	0.151	0.245	0.231
0.82	0.162	0.127	0.151	0.151	0.131	0.128	0.115	0.180	0.174
0.83	0.157	0.126	0.148	0.148	0.130	0.126	0.114	0.174	0.169
0.84	0.155	0.126	0.148	0.147	0.131	0.126	0.115	0.173	0.169
0.85	0.146	0.124	0.143	0.141	0.129	0.124	0.113	0.161	0.162
0.86	0.142	0.124	0.144	0.141	0.129	0.124	0.114	0.156	0.161
0.87	0.141	0.125	0.144	0.140	0.130	0.124	0.114	0.155	0.163
0.88	0.140	0.126	0.146	0.141	0.132	0.126	0.116	0.155	0.165
0.89	0.138	0.126	0.145	0.141	0.131	0.125	0.116	0.154	0.164

Table 2-6 Scene reflectance calibration ratios of SPOT multispectral images used in this study.

Image acquisition date	Reflectance calibration ratio $\frac{R_{rs}^{RCA}(\lambda)}{\bar{L}_S^{RCA}(\theta, \phi_z, \lambda)}$		
	Green	Red	Near infrared
7/04/2007	0.00282	0.00313	0.00420
7/19/2007	0.00232	0.00249	0.00410
8/23/2007	0.00331	0.00336	0.00532
9/03/2007	0.00345	0.00342	0.00500

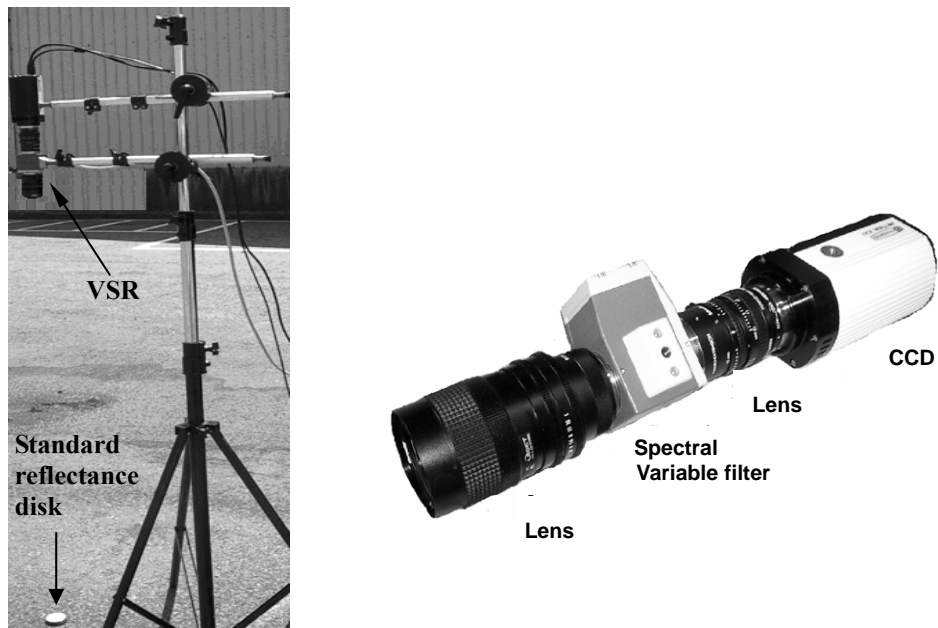


Figure 2-7 Variable spectral radiometer (VSR) used for reflectance calibration.

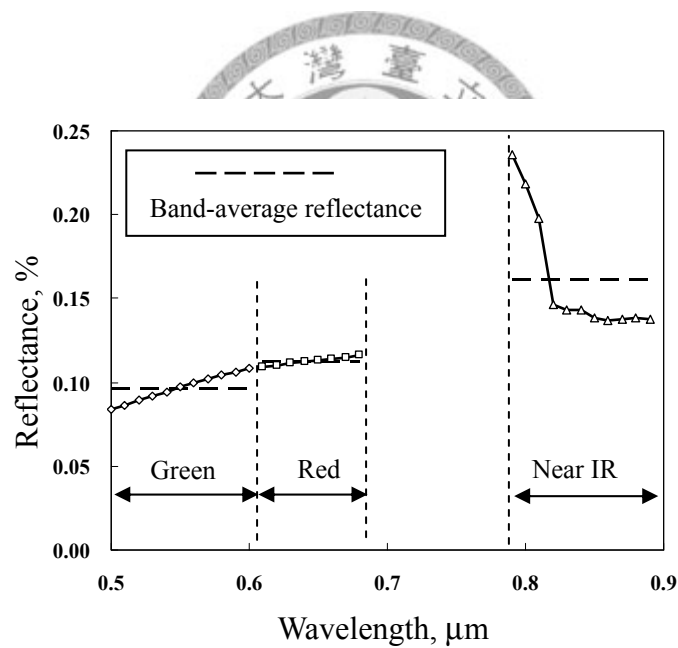


Figure 2-8 Calibrated wavelength-dependent RCA-average reflectances and band-average reflectances.

total suspended solids tend to increase with sea surface reflectance whereas secchi disk depth tends to decrease with increase of sea surface reflectance. Chlorophyll-a concentration has no significant correlation with sea surface reflectance. It approves that the optical properties of Case II water is not depends on Chlorophyll-a concentration.

To better illustrate the variation trend of these water quality variables, water quality measurements were grouped into several incremental intervals. Each water quality variable is classified into five or six classes, and interval-average water quality and corresponding average sea surface reflectance were calculated and were demonstrated in Figure 2-10(a)-(d). Using Equation 4-12, the specific water quality estimation models are as follow:

$$SDD = 6.25R_r^{-1.11} \quad (R^2 = 0.92, p=0.03) \quad (2-14a)$$

$$Turb = 0.97R_r^{3.65} \quad (R^2 = 0.93, p=0.01) \quad (2-14b)$$

$$TSS = -4.47 + 7.11R_r \quad (R^2 = 0.45, p=0.12) \quad (2-14c)$$

$$Chla = -0.8 + 1.7R_r \quad (R^2 = 0.22, p=0.29) \quad (2-14d)$$

where  $R_r$  represents the reflectance of red band. The signs of regression coefficients of  $R_r$  are consistent with the physical phenomena normally observed in the natural environment, except for chlorophyll-a concentration (refer to Figure 2-1).

Although the above water quality estimation models were established using the interval-average measurements, these models were adopted for water quality estimation using the pixel-based sea surface reflectance. The applicability of these models was checked by comparing the model estimates against the original



measurements. Figure 2-11(a) demonstrates that the water quality estimates are roughly consistent with the corresponding measurements. Each of the above models utilizes the single band reflectance  $R_r$  for estimation of a single water quality variable, and is referred to as the *univariate model* in this study.

The water body is a mixture of seawater, suspended solids, dissolved organic matters, zooplankton, etc. The sea surface reflectance of a specific wavelength is affected by the combined effect of these constituents. On the other hand, the effects of individual constituents on the sea surface reflectance vary among different spectral wavelengths. Such wavelength-dependent combined effect must be reflected in the water quality estimation model. Thus, we propose the following *multivariate model*, by multivariate regression (Johnson and Wichern, 2002), for water quality estimation using the multispectral reflectances:

$$Y_{n \times m} = Z_{n \times (r+1)} \cdot \beta_{(r+1) \times m} + \varepsilon_{n \times m} \quad (2-15)$$

where  $Y_{n \times m}$  is the dependent variable matrix ( $Y_{n \times m} = [SDD, Turb, TSS, Chla]$ ),  $m$  and  $n$  are the numbers of water quality ( $m=4$ ) and the number of data ( $n=25$ ), respectively.  $Z_{n \times (r+1)}$  is the independent variable matrix ( $Z_{n \times (r+1)} = [1, R_g, R_r, R_{ir}]$ ). Where the subscripts of reflectance refer to green, red and near infrared band. The number of band reflectances  $R$  is three.  $\beta_{(r+1) \times m}$  and  $\varepsilon_{n \times m}$  are the coefficient matrix and residual matrix, respectively. The coefficient matrix is estimated by least squared estimator and expressed as:

$$\hat{\beta} = (Z'Z)^{-1} Z'Y \quad (2-16)$$

After the coefficient matrix is estimated, the multivariate model can be expressed as

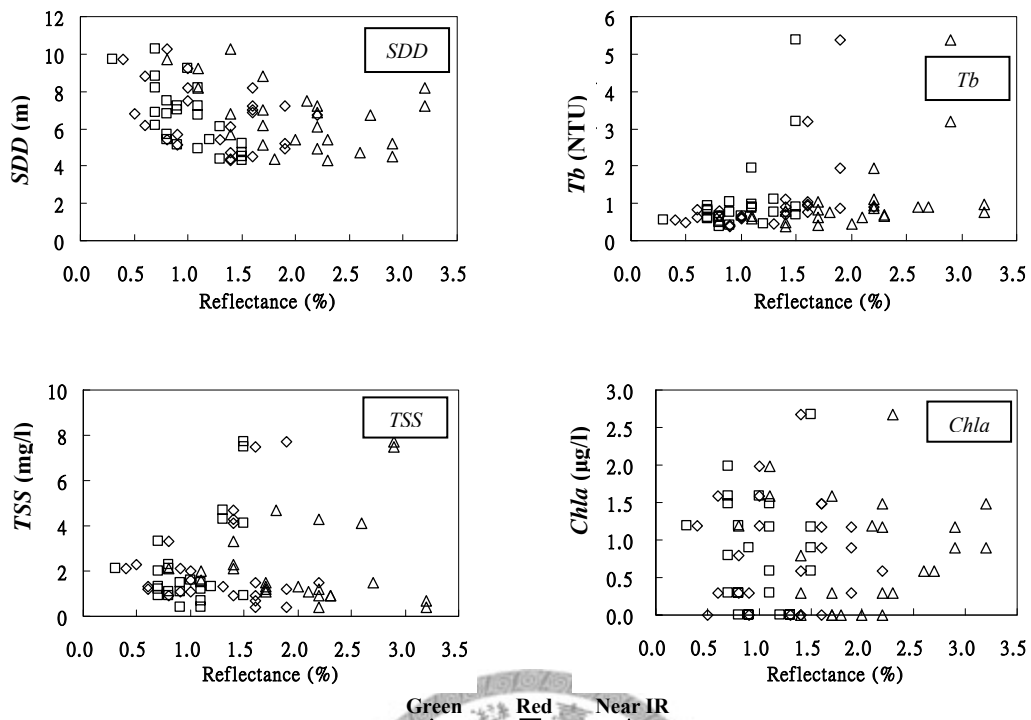


Figure 2-9 Scatter plots of water quality measurements versus band-dependent sea surface reflectances.

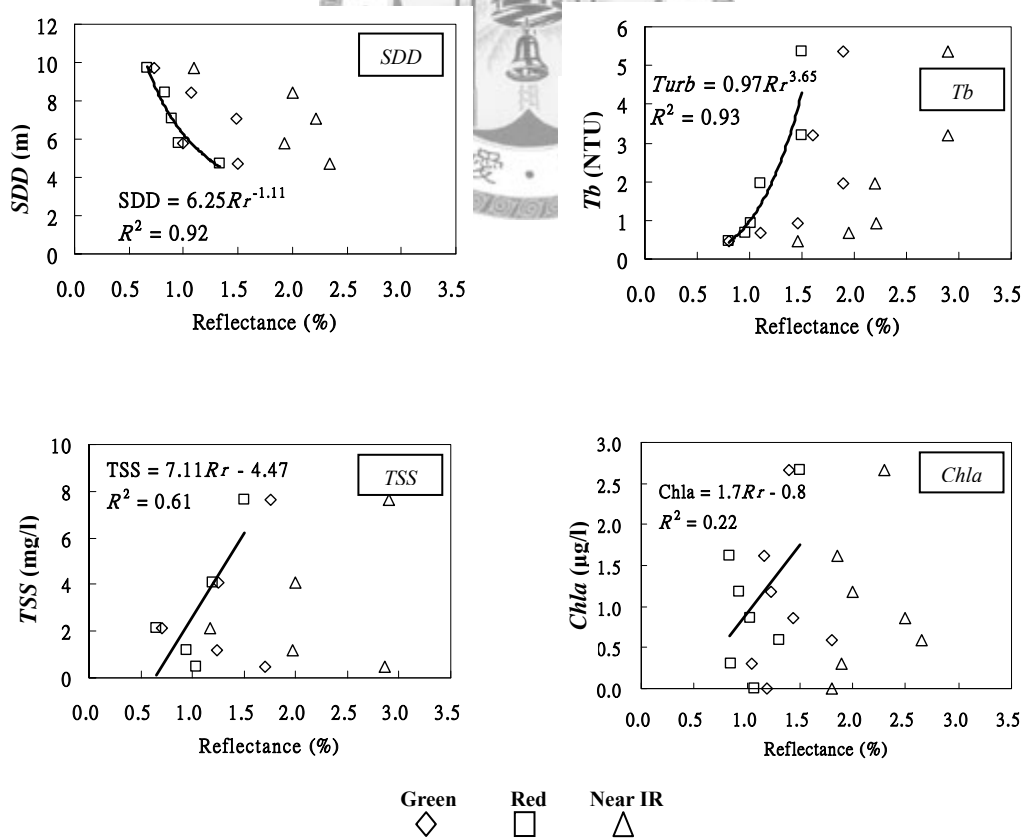


Figure 2-10 Scatter plots of interval-average water quality measurements versus sea surface reflectances.

$$[SDD, Tb, TSS, Chla] = [1, R_g, R_r, R_{ir}] \cdot \begin{bmatrix} 10.42 & -0.93 & -0.58 & 0.76 \\ 0.54 & 0.32 & -0.97 & 0.034 \\ -3.99 & 1.05 & 4.79 & -0.15 \\ -0.25 & 0.26 & -0.36 & 0.083 \end{bmatrix} \quad (2-17)$$

Figure 2-11(b) demonstrates the results of water quality estimation using the multivariate model. Comparing to the estimation results of the univariate model, water quality estimates of the multivariate model show significantly less degree of dispersion around the line of equivalence. Notably, there is an out-of-bound estimate of *SDD* using the univariate model (see Figure 2-11(a)), whereas the corresponding estimate by the multivariate model is quite accurate. The superior of the multivariate model may be attributed to its capability of modeling the wavelength-dependent combined effect of the seawater constituents. It is also noteworthy that the sign of regression coefficients of the red band reflectance ( $R_r$ ) in both models are consistent, and the red band reflectance remains the dominant factor in the multivariate model. Performance of water quality estimation by the univariate and multivariate models was evaluated with respect to the correlation coefficient ( $r$ ), root mean square error (RMSE) and normalized RMSE (see Table 2-7). Performance of the multivariate model is superior to the univariate model regardless of the overall or univariate performance.

Quantitative coastal water quality mapping was accomplished by substituting the pixel-specific spectral reflectance calculated by Eq. (2-12) into the multivariate model of Equation (2-17). The resultant water quality distribution maps are shown in Figure 2-12, Figure 2-13 and Figure 2-14. In general, *SDD* increases outward from the near shore area, whereas decreasing *Tb* and *TSS* can be observed. Such spatial variation trends are particularly evident on August 23 and September 3, 2007. Spatial variations of water quality variables on July 4 and 19 appear to be more complicated and the

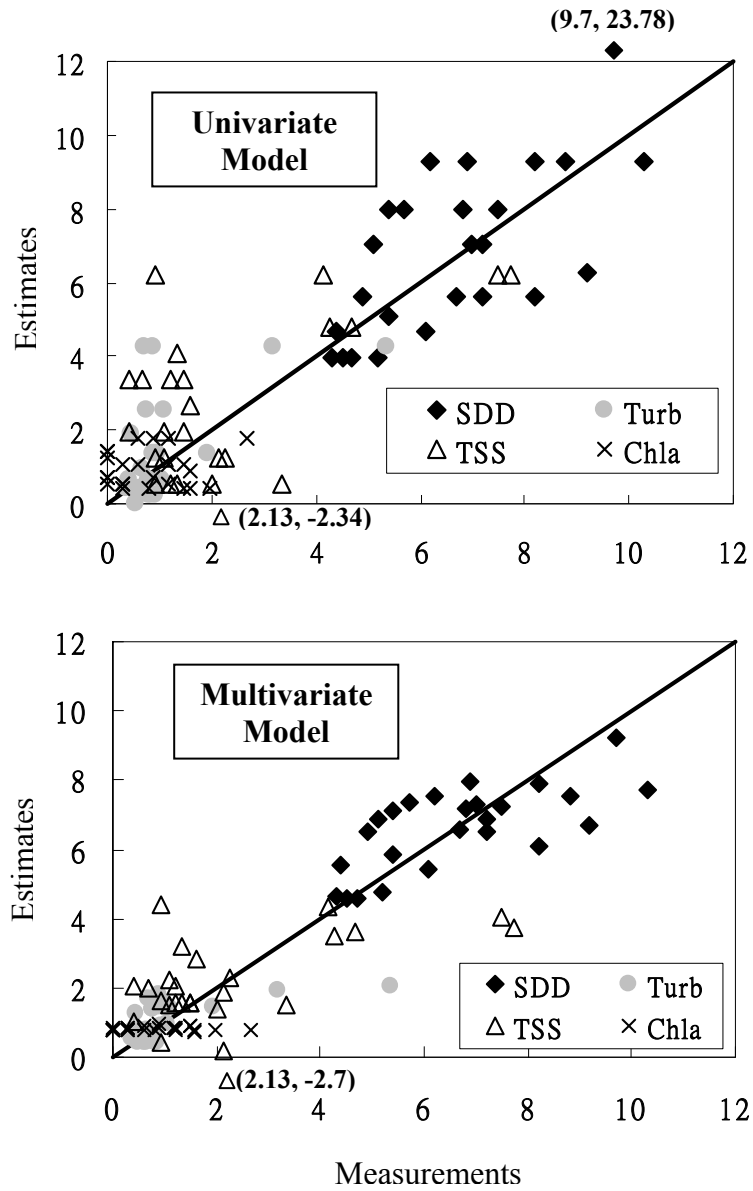


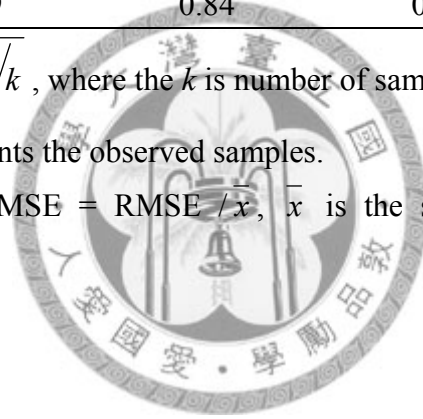
Figure 2-11 Water quality measurements versus estimates.

Table 2-7 Comparison of water quality estimation models.

Univariate model				
Variable	<i>SDD</i>	<i>Turb</i>	<i>TSS</i>	<i>Chla</i>
<i>r</i>	0.60	0.59	0.53	-0.003
RMSE <sup>a</sup>	3.21	1.21	2.06	0.89
NRMSE <sup>b</sup>	0.48	1.14	0.92	1.08
Multivariate model				
Variable	<i>SDD</i>	<i>Turb</i>	<i>TSS</i>	<i>Chla</i>
<i>r</i>	0.70	0.55	0.58	0.069
RMSE <sup>a</sup>	1.24	0.89	1.62	0.72
NRMSE <sup>b</sup>	0.19	0.84	0.72	0.88

<sup>a</sup>RMSE:  $\sqrt{\sum_{i=1}^k ((x_i - \hat{x}_i)^2) / k}$ , where the *k* is number of samples, the  $\hat{x}_i$  represents the estimates, the  $x_i$  represents the observed samples.

<sup>b</sup>NRMSE: normalized RMSE = RMSE /  $\bar{x}$ ,  $\bar{x}$  is the sample mean of observed samples.



influence of the water quality condition in the Yin-Yang Sea area is more significant. As can be seen in Figure 2-15(a), on July 2, 2007 there were higher waves on the sea and the brownish water color (the lower right corner in the figure) suggests higher concentrations of *TSS* and *Tb* in seawater. In contrast, the sea condition was calm on August 23 and no brownish water color can be observed in Figure 2-15(b). Turbidity distribution mapping also reveals areas with negative *Tb* values. Although small in magnitude, these negative estimates suggest exercising extra caution for estimates of low *Tb* concentration. Within the study area, the Yin-Yang Sea area has exceptionally higher *TSS* and *Tb* concentrations and lower *SDD* values due to non-dissolved solids routinely received from its upstream area. As for the area offshore from the YST tunnel outlet, no significant effect of the diverted flood flow on coastal water quality has been observed. This may be attributed to very few cases and short duration of flow diversion since the tunnel completion in 2003. However, a monitoring routine using satellite images is recommended for assessing the long term effect of the diverted flood flow on the coastal water quality.

## 2.5 Conclusions

In this study we demonstrate the feasibility of coastal water quality mapping using remote sensing images. A few concluding remarks are drawn as follows:

- (1) A surface reflectance estimation scheme which involves choosing a radiometric control area was proposed in this study. The scheme is applicable for local-scale environmental monitoring applications.
- (2) The three water quality variables (*SDD*, *Tb*, and *TSS*) are found to be most related to the red band surface reflectance. High values of the sea surface reflectance generally correspond to high *TSS* and *Tb* concentrations and low *SDD*

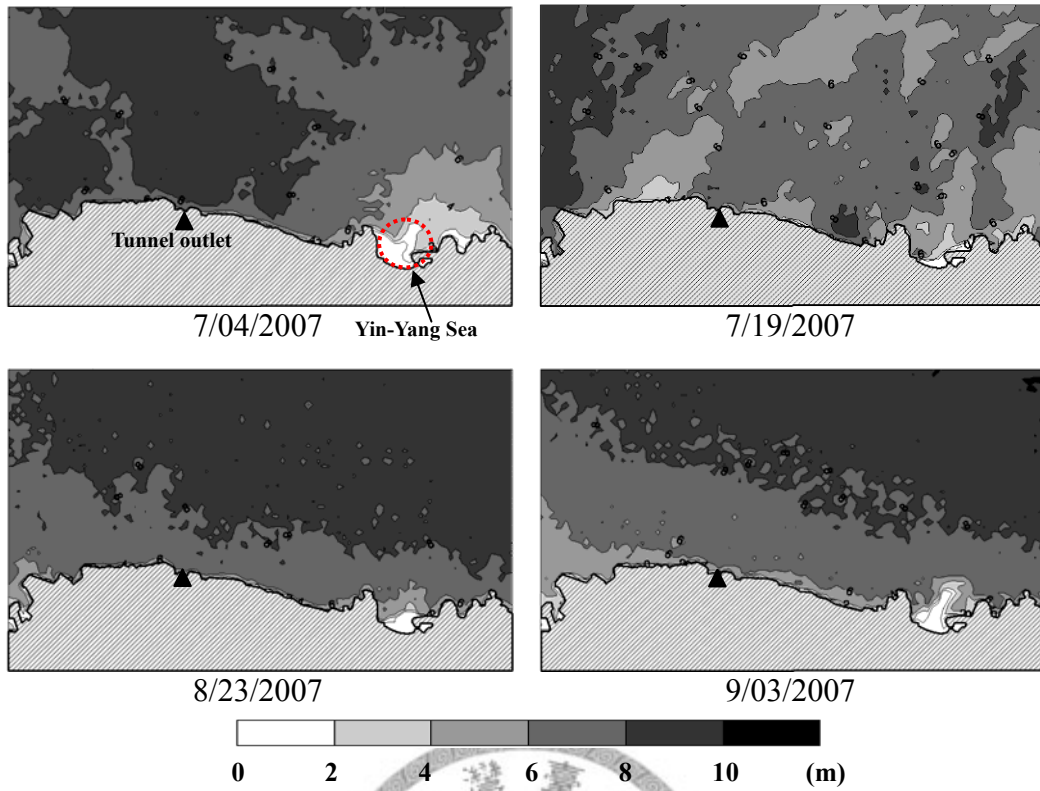


Figure 2-12 Spatial distribution of secchi disk depth.

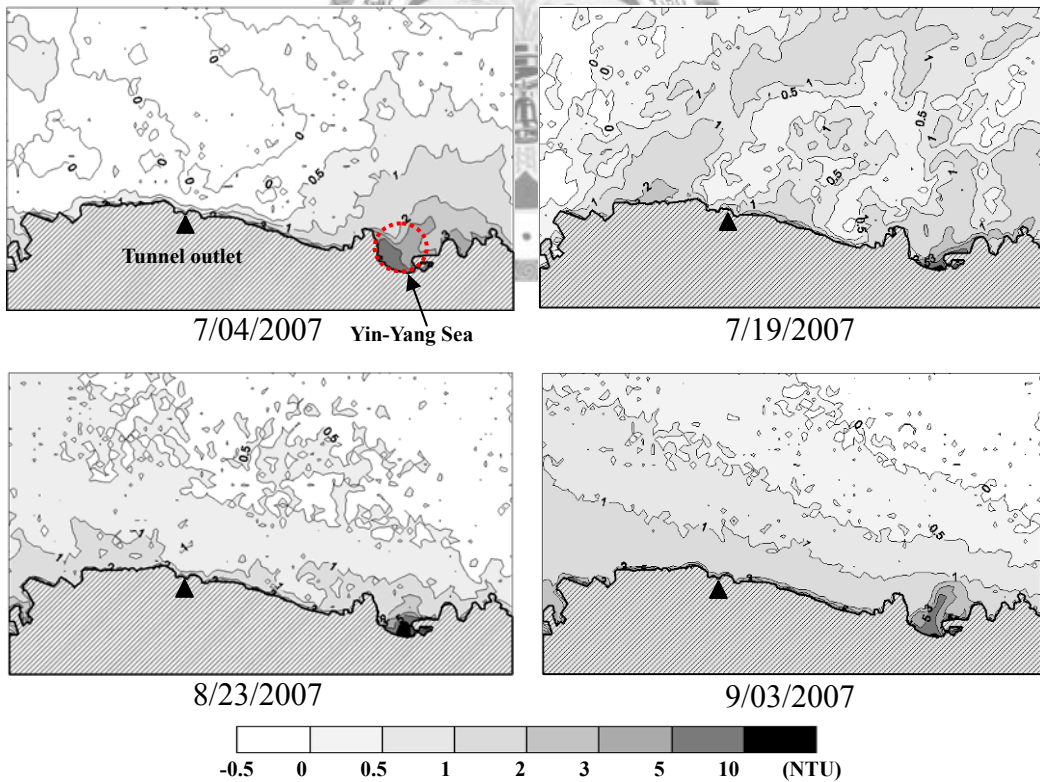


Figure 2-13 Spatial distribution of turbidity.

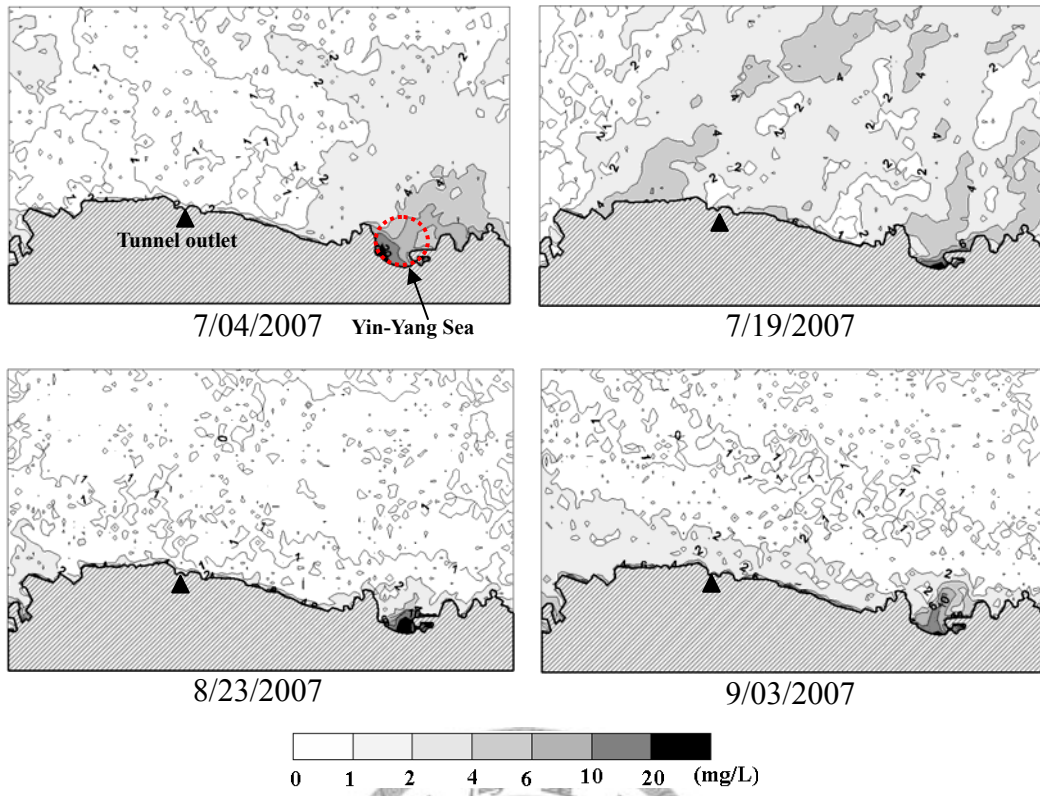


Figure 2-14 Spatial distribution of total suspended solids.

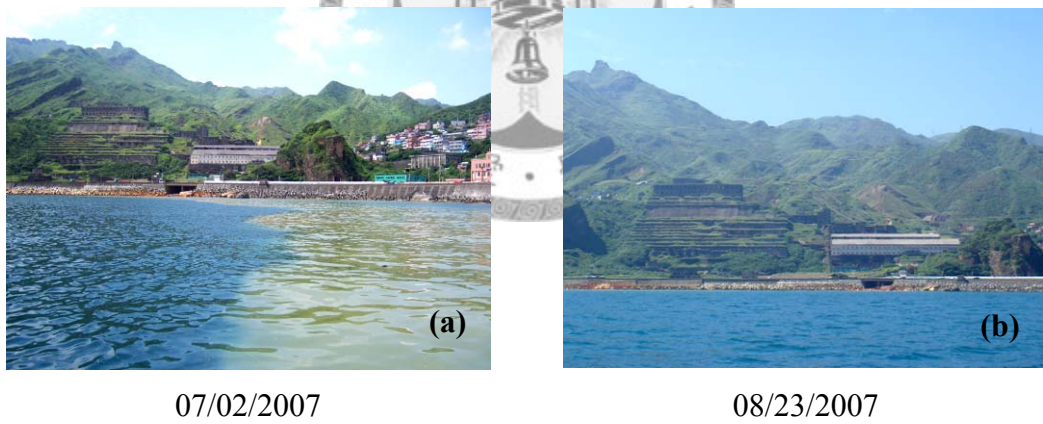


Figure 2-15 Photos of the Yin-Yang Sea area taken during water sampling campaigns.



values. However, *Chla* is not well-correlated to band surface reflectance.

- (3) The water body is a mixture of the seawater and other constituents including the suspended solids, the dissolved organic matters, the zooplankton, etc. The proposed multivariate water quality estimation model takes into consideration the wavelength-dependent combined effect of individual constituents on the sea surface reflectance and yields more accurate water quality estimation results.
- (4) The signs of all bands reflectances for chlorophyll-a concentration in multivariate model is coincident with the spectral feature of chlorophyll-a, whereas the spectral feature is not reflected in univariate model. The multivariate model takes the co-variance of water quality variables into account and yields better ability to explain the nature of water quality.
- (5) Water quality mapping using remote sensing images shows a general pattern of increasing *SDD* and decreasing *Tb* and *TSS* outward from the coast. Under higher wave condition, water quality in the Yin-Yang Sea area may have more significant influence on the spatial distribution of water quality in the nearby area.
- (6) Until present, no significant effect of the diverted flow on coastal water quality has been observed due to few cases of flow diversion. However, a routine operation of coastal water quality mapping utilizing satellite images is recommended for assessment of the long term effect of the diverted flow.

## References

- Bagheri, S. and Dios, R.A. (1990). Chlorophyll-a estimation in New Jersey's coastal waters using Thematic Mapper data. *International Journal of Remote Sensing*, 11(2), 289-299.
- Cannizzaro, J.P. and Carder, K.L. (2006). Estimating chlorophyll a concentrations from remote-sensing reflectance in optically shallow waters. *Remote Sensing of*

*Environment*, 101, 13-24.

Catts, G.P., Khorram, S., Cloern, J.E., Knight, A.W., Degloria, S.D. (1985). Remote sensing of tidal chlorophyll-a variations in estuaries. *International Journal of Remote Sensing*, 6(11), 1685-1706.

Chavez, P.S. Jr. (1988). An improved dark-object subtraction technique for atmospheric scattering correction of multispectral data. *Remote Sensing of Environment*, 24, 459-479.

Cheng, K.S. and Lei, T.C. (2001). Reservoir trophic state evaluation using Landsat TM Images. *Journal of the American Water Resources Association*, 37(5), 1321-1334.

Dekker, A.G., Vos, J.R. and Peters, S.W.M. (2002). Analytical algorithms for lake water TSM estimation for retrospective analysis of TM and SPOT sensor data. *International Journal of Remote Sensing*, 23(1), 15-35.

Doxaran, D., Froidefond, J.M., Lavender, S., Castaing, P. (2002). Spectral signature of highly turbid waters: Application with SPOT data to quality suspended particulate matter concentrations. *Remote Sensing of Environment*, 81, 149-161.

Gao, P., Pasternack, G.B., Bali, K.M., Wallender, W.W. (2008). Estimating suspended sediment concentration using turbidity in an irrigation-dominated southeastern California watershed. *Journal of Irrigation and Drainage Engineering*, 134(2), 250-259.

Giardino, C., Pepe, M., Brivio, P.A., Ghezzi, P., Zilioli, E. (2001). Detecting chlorophyll, secchi disk depth and surface temperature in a sub-apline lake using Landsat imagery. *The Science of the Total Environment*, 268, 19-29.

Grayson, R.B., Finlayson, B.L., Gippel, C.J. and Hart, B.T. (1996). The potential of field turbidity measurements for the computation of total phosphorus and suspended solids loads. *Journal of Environmental Management*, 47, 257-267.

Härmä, P., Vepsäläinen, J., Hannonen, T., Pyhalahti, T., Kämäri, J., Kallio, K., Eloheimo, K., Koponen, S. (2001). Detection of water quality using simulated satellite data and semi-empirical algorithms in Finland. *The Science of the Total Environment*, 268, 107-121.

Hellweger, F.L., Schlosser, P., Lall, U., Weissel, J.K. (2004). Use of satellite imagery for water quality studies in New York Harbor. *Estuarine, coastal and shelf science*, 61, 437-448.

- Hoegh-Guldberg, O., Muscatine, L., Goiran, C., Siggaard, D., Marion, G. (2004). Nutrient-induced perturbations to  $\delta^{13}\text{C}$  and  $\delta^{15}\text{N}$  in symbiotic dinoflagellates and their coral hosts. *Mar. Ecol. Prog. Ser.*, 280, 105-114.
- Huang, C.S. (2006). *Development and application of the model of water quality and optical properties in reservoir*. Master thesis of Department of Environmental Engineering, National Cheng Kung University (In Chinese).
- Johnson, R.A. and Wichern, D.W. (2002). *Applied multivariate statistical analysis* (5th ed.). New Jersey: Prentice Hall, 383p.
- Khorram, S. (1981). Water quality mapping from Landsat digital data. *International Journal of Remote Sensing*, 2(2), 145-153.
- Khorram, S. and Cheshire, H. M. (1985). Remote sensing of water quality in the Neuse River Estuary, North Carolina. *Photogrammetric Engineering and Remote Sensing*, 51(3), 329-341.
- Khorram, S., Cheshire, H., Geraci, A. G., Rosa, G. (1991). Water quality mapping of Augusta Bay, Italy from Landsat-TM data. *International Journal of Remote Sensing*, 12(4), 803-808.
- Kloiber, S.M., Brezonik, P.L., Olmanson, L.G., Bauer, M.E. (2002). A procedure for regional lake water clarity assessment using Landsat multispectral data. *Remote Sensing of Environment*, 82, 38-47.
- Koponen, S., Pulliainen J., Kallio K., Hallikainen, M. (2002). Lake water quality classification with airborne hyperspectral spectrometer and simulated MERIS data. *Remote Sensing of Environment*, 79, 51-59.
- Lavery, P., Pattiaratchi, C., Wyllie, A., Hick, P. (1993). Water quality monitoring in estuarine waters using the Landsat Thematic Mapper. *Remote Sensing of Environment*, 46, 268-280.
- Lewis, J. (1996). Turbidity-controlled suspended sediment sampling for runoff-event load estimation. *Water Resources Research*, 32(7), 2299-2310.
- Lodhi, M.A., Rundquist, D.C., Han, L., Kuzila, M.S. (1997). The potential for remote sensing of loess soils suspended in surface waters. *Journal of the American Water Resources Association*, 33(1), 111-117.
- Lin, C.C. (2005). *The water quality monitoring using FORMOSAT-2 imagery in Sunmoon-Lake*. Master thesis of Environment and Information Science and Technology (In Chinese).

- Mobley (1994). *Light and water: radiative transfer in natural waters*. New York: Academic Press, 60p.
- Morel, A. and Prieur, L. (1977). Analysis of variations in ocean color. *Limnology and Oceanography*, 22(4), 709-722.
- Östlund, C., Flink, P., Strombeck, N., Pierson, D., Lindell, T. (2001). Mapping of the water quality in Lake Erken, Sweden, from Imagery Spectrometry and Landsat Thematic Mapper. *The Science of the Total Environment*, 268, 139-154.
- Oyama, Y., Matsushita, B., Fukushima, T., Nagai, T, Imai, A. (2007). A new algorithm for estimating chlorophyll-a concentration from multi-spectral satellite data in case II waters: a simulation based on a controlled laboratory experiment. *International Journal of Remote Sensing*, 28(7), 1437-1453.
- Pattiaratchi, C., Lavery, P., Wyllie, A., Hick, P. (1994). Estimates of water quality in coastal water using multi-date Landsat Thematic Mapper data. *International Journal of Remote Sensing*, 15(8), 1571-1584.
- Pavanelli, D. and Bigi, A. (2005). Indirect methods to estimate suspended sediment concentration: Reliability and relationship of turbidity and settleable solids. *Biosystems Engineering*, 90(1), 75-81.
- Populus, J., Hastuti, W., Martin, J.L.M., Guelorget, O., Sumartono, B., Wibowo, A. (1995). Remote sensing as a tool for diagnosis of water quality in Indonesian seas. *Ocean and Coastal Management*, 27(3), 197-215.
- Prangma, G. J. and Roozkrans, J. N. (1989). Using NOAA AVHRR imagery in assessing water quality parameters. *International Journal of Remote Sensing*, 10(4), 811-818.
- Rimmer, J. C, Collins, M. B. and Pattiaratchi, C. B. (1987). Mapping of water quality in coastal waters using Airborne Thematic Mapper data. *International Journal of Remote Sensing*, 8(1), 85-102.
- Ritchie, J. C. and Cooper, C. M. (1988) Comparison of measured suspended sediment concentrations with suspended sediment concentrations estimated from Landsat MSS data. *International Journal of Remote Sensing*, 9(3), 379-387.
- Rundquist, D.C., Han, L., Schalles, J.F., Peake, J.S. (1996). Remote measurement of algal chlorophyll in surface waters: The case for the first derivative of reflectance near 690nm. *Photogrammetric Engineering & Remote Sensing*, 62(2), 195-200.
- Schott, J.R. (1997). *Remote Sensing – The Image Chain Approach*. New York: Oxford

University Press, 394p.

Su, Y.F., Liou, J.J., Hou, J.C., Hung, W.C., Hsu, S.M., Lien, Y.T., Su, M.D., Cheng, K.S., Wang, Y.F. (2008). A multivariate model for coastal water quality mapping using satellite remote sensing images. *Sensors*, 8, 6321-6339.

Tan, C.K. (2006). *Application of bio-optical models and FORMOSAT-2 remote sensing imagery to study the temporal and spatial distribution of water quality in Tseng-Wen Reservoir*. Ph.D. dissertation of Department of Environmental Engineering, National Cheng Kung University (In Chinese).

Tassan, S. (1987). Evaluation of the potential of the Thematic Mapper for marine application. *International Journal of Remote Sensing*, 8(10), 1455-1478.

Teng, S.P., Chen, Y.K., Cheng, K.S., Lo, H.C. (2008). Hypothesis-test-based landcover change detection using multitemporal satellite images. *Advances in Space Research*, 41, 1744-1754.

Tomascik, T., Sander, F. (1985). Effects of eutrophication on reef-building corals. I. Growth rate of the building coral *Montastrea annularis*. *Mar. Biol.*, 87, 143–155.

Verdin, J. P. (1985). Monitoring water quality conditions in a large western reservoir with Landsat imagery. *Photogrammetric Engineering and Remote Sensing*, 51(3), 343-353.

Wang, Y., Xia, H., Fu, J., Shen, G. (2004). Water quality change in reservoirs of Shenzhen, China: detection using Landsat/TM data. *Science of the Total Environment*, 328, 195-206.

Wu, C.Y., (2001). *A study on water quality monitoring of Yung-He-Shan reservoir using satellite images*. Master thesis of Department of Civil Engineering, Chung Hua University (In Chinese).

## Chapter 3 Assessing the effect of landcover changes on air temperature using remote sensing images

### 3.1 Introduction

Rice cultivation through paddy irrigation has had a long history in eastern and southeastern Asia. The vast extent of paddy fields necessitates a well-organized and sophisticated irrigation network including reservoirs, ponds, intake/outlet structures, pumps, channels, and flumes to convey enough water to all points in an irrigation district. Despite of its long history and relevant cultural aspect, such practices have been criticized for inefficiency of water utilization. In addition, demand and request for larger share of water utilization from industrial sectors are ever increasing due to low market prices of agricultural produce as compared to industrial products. After entering WTO, agricultural sectors in Taiwan also face harsh competition of imported produce from labor-cheap countries. As a result, paddy fields in some regions are let fallow and converting paddy fields to other landuse types have been discussed. However, in addition to rice production, there are also concerns about multifunctionality of paddy cultivation. Such concerns have been the focus of countries and professional societies in eastern and southeastern Asia over the last several years. An important and apparent function of paddy field is its capability of flood retention during the typhoon and monsoon seasons (Nakanishi, 2004; Unami and Kawachi, 2005). Other functions of paddy culture include recharge of groundwater (Greppi, 2004), air temperature cooling (Saptomo *et al.*, 2004; Yokohari *et al.*, 1997, 2001), removal of pollutants in irrigation water (Ishikawa *et al.*, 2003; Nakasone, 2003), providing habitat for inhabitants (Fukuda *et al.*, 2006), aesthetic landscape, and facilitating religious/cultural activities. Many of these functions have been experienced or practiced for many generations. However, quantitative

evaluations of individual functions are difficult and rare due to lack of data and, in some cases, difficulty in determining what to measure.

Many major cities in eastern Asia still paddy fields within their close vicinities. Existence of such paddy fields provides many functions in urban areas (Yokohari *et al.*, 1994). Extensive landuse changes of paddy fields may have significant environmental, ecological, cultural, and social impacts and yield potentially severe and adverse consequences. Therefore, the positive and adverse effects of paddy culture should be thoroughly investigated and considered in the landuse planning and decision-making process.

Yokohari *et al.* (1994, 1997, 2001) conducted a series of studies on the temperature cooling effect of paddy fields in urban fringe areas of Tokyo using field measured land surface and air temperatures. They found that measured surface temperatures varied by approximately 20°C, while measured air temperatures differed by more than 2°C. For large study areas, it would be labor and time consuming to conduct field measurements. With the availability of many images from weather and land observation satellites, it seems beneficial and feasible to use remote sensing images to aid in similar studies. In addition, what kinds of landuse conversions should be pursued in order to avoid adverse effect and to sustain the environment quality in the region must also be investigated for a sound decision making. Therefore, the objectives of this study are to quantitatively evaluate the effect of landcover types on ambient air temperature using remote sensing images and to understand the inter-relationships of different landcover types in a region through a pilot study conducted in northern Taiwan. The flowchart of this study is shown in Figure 3-1.

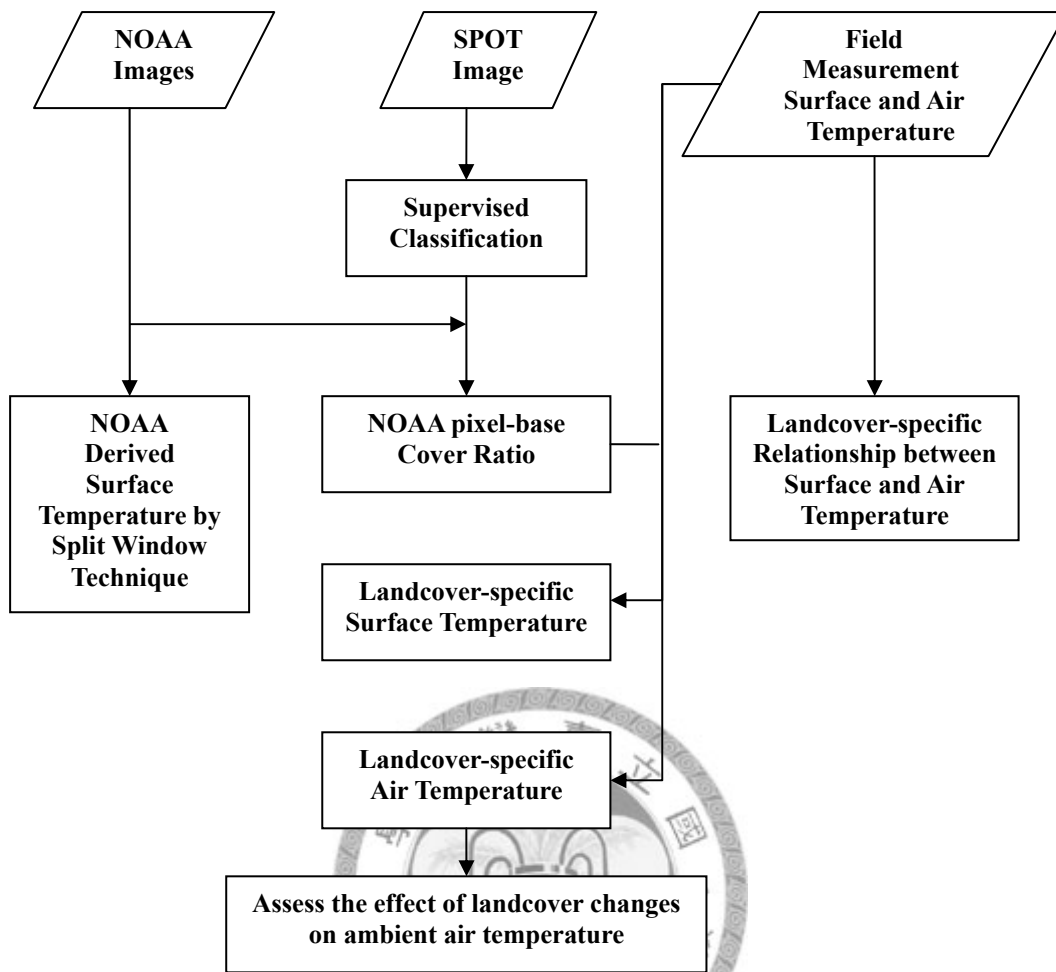


Figure 3-1 Flowchart for assessing the effect of landcover changes on ambient air temperature.



### 3.2 Energy exchange between the land surface and the atmosphere

Surface of paddy fields (partly to fully covered by crop canopy, depending on the growth condition) generally has a lower temperature than landcover types like bare soil and paved surfaces due to its higher moisture content in solids. However, instead of the land surface temperature, the ambient air temperature is of interest in assessment of the cooling effect of paddy field. The relationship of land surface temperature and ambient air temperature depends on landcover types and can be derived by considering energy exchange between the atmosphere and the land surface.

Energy exchange between the atmosphere and the land surface (or the crop canopy) can be expressed by the following energy balance equation:

$$R_n - LE - H - G = 0 \quad (3-1)$$

where  $R_n$ ,  $LE$ ,  $H$  and  $G$  respectively, represent the net radiation at the land surface, the latent heat flux, the sensible heat flux, and the soil heat flux.

The net radiation is the sum of incoming and outgoing short and longwave radiations on the land surfaces, and is expressed by

$$R_n = (1 - r_{ss})S_0 - \varepsilon_s \sigma T_s^4 + (1 - r_{sl})\varepsilon_a \sigma T_{sky}^4 \tau \quad (3-2)$$

where

$S_0$  = incident solar radiation

$r_{ss}$  = the shortwave reflectance of the land surface

$r_{sl}$  = the longwave reflectance of the land surface

$\varepsilon_s$  = the thermal emissivity of the land surface

$\varepsilon_a$  = the thermal emissivity of the atmosphere

$T_s$  = the absolute temperature of the canopy or land surface

$T_{sky}$  = the absolute temperature of the atmosphere

$\tau$  = the average transmittance of the atmosphere

$\sigma$  = the Stefan- Boltzmann constant.

The first term in the right-hand-side of the above equation is the net incoming shortwave radiation. The second term is the thermal radiation emitted from the land surface. The last term is the thermal radiation emitted by the atmosphere and absorbed by the land surface. For thermal radiation, transmittance through the land surface can be assumed to be zero and, under the thermal equilibrium, the emissivity equals the absorptance ( $\alpha_a$ ). Therefore,

$$\alpha_s + r_{sl} = \varepsilon_s + r_{sl} = 1 \quad (3-3)$$

the net radiation of the land surface  $R_n$  can thus be expressed as

$$R_n = (1 - r_{ss})S_0 - \varepsilon_s \sigma T_s^4 + \varepsilon_s \varepsilon_a \sigma T_{sky}^4 \tau \quad (3-4)$$

The sensible heat flux can be expressed in terms of temperature difference as (Monteith and Unsworth, 1990):

$$H = \rho C_p \frac{T_s - T_a}{r_a} \quad (3-5)$$

where  $\rho$  is the air density,  $C_p$  the specific heat of air at constant pressure,  $r_a$  the aerodynamic resistance, and  $T_a$  is the air temperature at a reference height above the land surface.

The latent heat is the energy used for transport of water vapor from the land surface, through crop evapotranspiration or evaporation from the soil, to the atmosphere and may be expressed as (Monteith and Unsworth, 1990):

$$LE = \frac{\rho C_p [e_0(T_s) - e_a]}{r_a \gamma} \quad (3-6)$$

where  $e_0(T_s)$  is the saturation vapor pressure at temperature  $T_s$ ,  $e_a$  is the actual vapor pressure, and  $\gamma$  is the psychrometric constant. The vapor pressure deficit (VPD) of the

atmosphere is defined as

$$VPD = e_0(T_s) - e_a \quad (3-7)$$

The  $e_0(T_s) - e_a$  term in Eq. (3-6) can be expressed by

$$e_0(T_s) - e_a = [e_0(T_a) - e_a] + \Delta(T_s - T_a) \quad (3-8)$$

where  $\Delta$  is the slope of the saturation vapor pressure as a function of temperature.

Substituting Eq. (3-8) into Eq. (3-6), it yields:

$$LE = \frac{\rho C_p [VPD + \Delta(T_s - T_a)]}{r_a \gamma} \quad (3-9)$$

Idso *et al.*, (1997) suggested that the soil heat flux ( $G$ ) can be considered as a fraction ( $\xi$ ) of  $R_n$ , i.e.,

$$G = \xi R_n \quad (3-10)$$

Rearrangement of the energy balance equation, i.e. Eq. (3-1), yields:

$$(1 - \xi)R_n = LE + H \quad (3-11)$$

Substituting Eqs. (3-5) and (3-9) into Eq. (3-11), we have

$$(1 - \xi)R_n = \rho C_p \frac{T_s - T_a}{r_a} + \frac{\rho C_p [VPD + \Delta(T_s - T_a)]}{r_a \gamma} \quad (3-12)$$

Rearranging the above equation yields:

$$\left[1 + \frac{\Delta}{\gamma}\right](T_s - T_a) = \frac{r_a(1 - \xi)R_n}{\rho C_p} - \frac{VPD}{\gamma} \quad (3-13)$$

$$T_a = T_s - \left[ \frac{r_a \gamma (1 - \xi)R_n}{(\Delta + \gamma)\rho C_p} - \frac{VPD}{\Delta + \gamma} \right] \quad (3-14)$$

The above equation expresses the relation of the air and surface temperatures. Both

the land surface temperature  $T_s$  and the net radiation  $R_n$  vary with landcover types, and therefore, the  $T_s \sim T_a$  relationships are landcover-dependent. The best way of collecting the landcover information in a large study area is by using remote sensing images, and thus Eq. (3-14) provides the rationale of combining remotely sensed land surface temperature  $T_s$  and locally calibrated  $T_s \sim T_a$  relationship for estimation of the air temperature with respect to different landcover types.

### **3.3 Study area and remote sensing data set**

An area of approximately 275 km<sup>2</sup> in Tao-Yuan County of northern Taiwan was chosen for this study (Figure 3-2). It encompasses different landcover types including paddy field, water ponds, residential and factory buildings, and other vegetations. The western half is mostly agricultural area while the eastern half has mixed land uses including manufactural and industrial parks. Multispectral remote sensing images of the study area from NOAA-16 AVHRR sensors and SPOT-4 HRVIR sensors were collected. Overpasses of the NOAA satellites were almost concurrent with the time of field data collection on 16 March and 4 April 2005. NOAA thermal images (channels 4 and 5, with a spatial resolution of 1.1km×1.1km) were used for retrieval of land surface temperature. High-resolution multispectral SPOT images (green, red, infrared channels, with a spatial resolution of 20m×20m) were used for landcover classification. A set of 45 orthorectified aerial photos (Figure 3-3) at 1:5000 scale were also collected to assist in landcover classification.

### **3.4 Land surface temperature estimation using NOAA images**

The first step of our approach for assessing the effect of landcover types on ambient air temperature is to estimate the land surface temperature using NOAA thermal images. The AVHRR sensors aboard NOAA satellite receive and record thermal

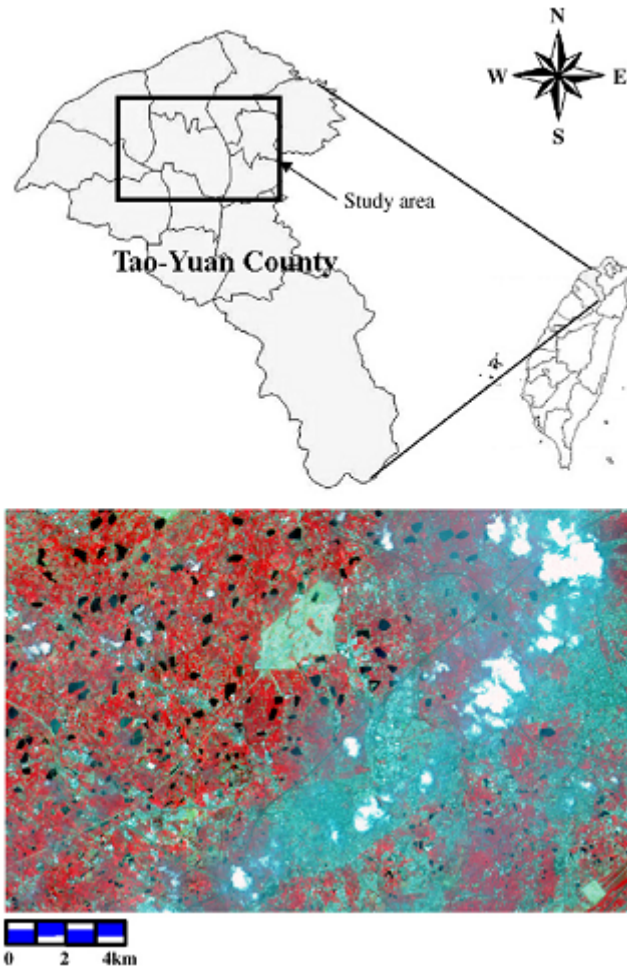


Figure 3-2 Location map and pseudo-color SPOT image of the study area.

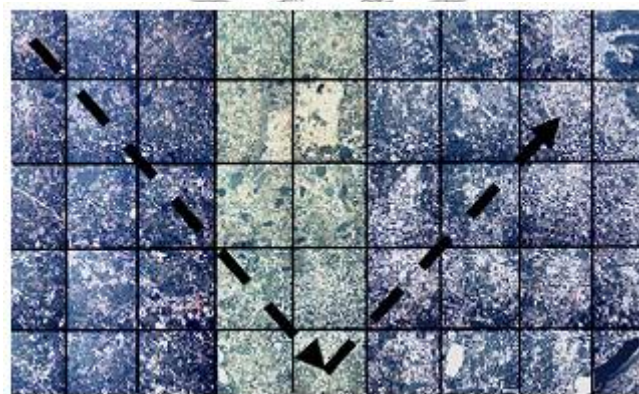


Figure 3-3 Orthorectified aerial photos of the study area and the field sampling route.

emissions from objects on the land surface. These sensors receive radiances within specific windows and techniques have been developed for retrieval of land surface temperatures from remote sensing thermal images (Prabhakara *et al.*, 1974; McMillan, 1975; Chedin *et al.*, 1982; Price, 1984; Kerr *et al.*, 1992; Li and Becker, 1993; Vasquez *et al.*, 1997). Among these methods, the split window technique (SWT) briefly described below is most widely applied and adopted in this study. Readers are referred to Schott (1997) for theoretical details of the following derivations.

Let the radiance received by a sensor with spectral window centered at wavelength  $\lambda$  and the radiance emitted by a target object on the earth surface be respectively represented by  $L_\lambda(h)$  and  $L(0)$ . The radiance from the air column between the target and the sensor due to its mean effective temperature is represented by  $L_{TA}$ . We then have

$$L_\lambda(h) = L(0)\tau_\lambda(h) + L_{TA}[1 - \tau_\lambda(h)] \quad (3-15)$$

where  $h$  is the height of the satellite orbit and  $\tau_\lambda(h)$  is the effective transmittance of the air column with respect to the sensor's spectral window.

For atmospheres dominated by absorption effects, the transmittance expressed as

$$\tau_\lambda(h) = e^{-\beta_\alpha(\lambda)h} \quad (3-16)$$

where  $\beta_\alpha(\lambda)$  is the absorption coefficient with respect to the spectral window centered at  $\lambda$  and  $\beta_\alpha(\lambda)h$  is the optical depth. For clear atmospheres,  $\tau_\lambda(h)$  can be expanded using a Taylor series and truncated to yield as a good approximation:

$$\tau_\lambda(h) = 1 - \beta_\alpha(\lambda)h \quad (3-17)$$

Therefore,

$$L_{\lambda}(h) = L(0) - [L(0) - L_{TA}] \beta_{\alpha}(\lambda) h \quad (3-18)$$

Assuming a linear relationship between the radiance and the apparent temperature, it yields:

$$T_{\lambda}(h) = T(0) - [T(0) - T_A] \beta_{\alpha}(\lambda) h \quad (3-19)$$

where  $T_{\lambda}(h)$  is the apparent temperature at the sensor,  $T(0)$  the apparent temperature at the surface, and  $T_A$  is the apparent temperature corresponding to  $L_{TA}$ . The apparent temperature (also known as the brightness temperature) of an object is the kinetic temperature which a perfect radiator would be required to maintain in order to generate the radiance measured from the object.

Suppose that images of two spectral channels (each of nominal wavelength  $\lambda_1$  and  $\lambda_2$ ) which an atmospheric window are available. Then,

$$T_{\lambda_1}(h) = T(0) - [T(0) - T_A] \beta_{\alpha}(\lambda_1) h \quad (3-20)$$

$$T_{\lambda_2}(h) = T(0) - [T(0) - T_A] \beta_{\alpha}(\lambda_2) h \quad (3-21)$$

where  $T_{\lambda_1}(h)$  and  $T_{\lambda_2}(h)$  are the apparent temperatures at the sensor with respect to channels 1 and 2, respectively. Rearranging Eq. (3-20) and (3-21), we have

$$T(0) = T_{\lambda_1}(h) + [T(0) - T_A] \beta_{\alpha}(\lambda_1) h \quad (3-22)$$

$$T(0) - T_A = \frac{T(0) - T_{\lambda_2}(h)}{\beta_{\alpha}(\lambda_1) h} \quad (3-23)$$

$$T(0) = T_{\lambda_1}(h) + \frac{T(0) - T_{\lambda_2}(h)}{\beta_{\alpha}(\lambda_2) h} \beta_{\alpha}(\lambda_1) h \quad (3-24)$$

$$T(0) = T_{\lambda_1}(h) + (T(0) - T_{\lambda_2}(h)) \frac{\beta_{\alpha}(\lambda_1)}{\beta_{\alpha}(\lambda_2)} \quad (3-25)$$

Let

$$R = \frac{\beta_{\alpha}(\lambda_1)}{\beta_{\alpha}(\lambda_2)} \quad (3-26)$$

it yields:

$$(1-R)T(0) = T_{\lambda_1}(h) + T_{\lambda_2}(h)R \quad (3-27)$$

$$T(0) = \frac{T_{\lambda_1}(h) + T_{\lambda_2}(h)R}{1-R} \quad (3-28)$$

$$\begin{aligned} T(0) &= c_1 T_{\lambda_1}(h) + (1-c_1) T_{\lambda_2}(h) \\ &= c_1 T_{\lambda_1}(h) + c_2 T_{\lambda_2}(h), \quad [c_1 + c_2 = 1] \end{aligned} \quad (3-29)$$

Or,

$$T(0) = T_{\lambda_1}(h) + \frac{(1-R)}{R} [T_{\lambda_1}(h) - T_{\lambda_2}(h)] \quad (3-30)$$

Eq. (3-30) shows that the land surface temperature can be calculated using the at-sensor apparent temperatures (which can be calculated using the measured radiances and the Planck's equation) of two spectral channels.

Gallo *et al.* (1993) and Florio *et al.* (2004) proposed the following equation for estimation of the land surface temperature using NOAA images of channels 4 and 5.

$$T(0) = T_4 + 3.3(T_4 - T_5) \quad (3-31)$$

where  $T_4$  and  $T_5$  are respectively the apparent temperatures of the target object derived from NOAA images of channels 4 and 5. Hereafter, apparent surface temperatures estimated using Eq. (3-31) will be referred to as the SWT surface temperatures.

Figure 3-4 shows the spatial variation of SWT surface temperatures over the study area during 2 days of field data collection (described later). It can be seen clearly that apparent surface temperatures are higher in area with residential and factory building (the circled area) and lower in the northwestern region where paddy fields and other vegetations are the dominant landcover types. However, NOAA AVHRR images have



a spatial resolution of 1.1 km and each pixel corresponds to an area of 1.21 km<sup>2</sup> on the earth surface. There may be different landcover types within the spatial coverage of a NOAA pixel, and the SWT surface temperatures are average temperatures of all landcover types within the pixel coverage.

### 3.5 Estimating the landcover-specific surface temperatures

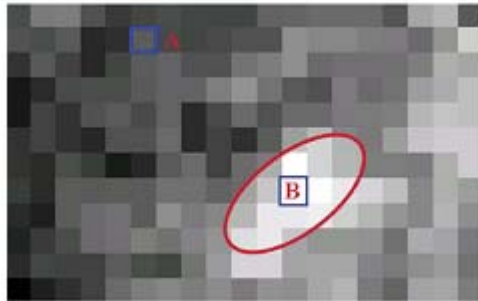
SWT surface temperatures derived from NOAA images represent average temperature within a pixel which may be composed of several landcover types. Four major landcover types are present in the study area: (1) paddy fields, (2) water ponds, (3) built-up areas (including paved roads, residential area, and factory buildings) and bare soils, and (4) other vegetations. In order to assess the effect of landcover types on ambient air temperatures, it is necessary to further estimate the apparent temperatures of individual landcover types from the SWT surface temperatures. This can be done by determining the coverage ratios of different landcover types within individual NOAA pixels using the multispectral SPOT images. Detailed procedures are described below.

Assume that  $k$  different landcover types are present in the study area. Within the spatial coverage of a pixel, each landcover type accounts for  $w_i$  ( $i=1, 2, \dots, k$ ). The pixel-average land surface temperatures can thus be calculated as

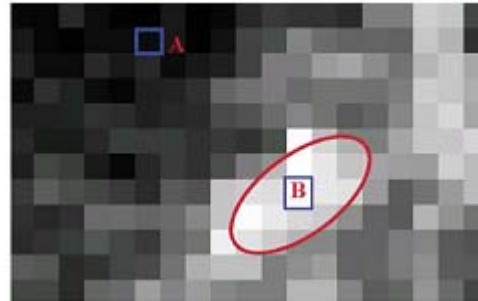
$$\bar{T}(j) = \sum_{i=1}^k w_i(j) T_i(j), \quad j = 1, 2, \dots, N \quad (3-32)$$

where  $j$  is the index specifying individual pixels in the NOAA AVHRR images and  $N$  is the total number of pixels in the study area. The coverage ratio  $w_i$ 's not only vary with landcover but also pixels.

We also assume that within the study area the apparent temperatures of specific



(a) March 16, 2005



(b) April 4, 2005



(c) Detailed landcover in area A



(d) Detailed landcover in area B

Figure 3-4 (a) and (b): spatial variation of apparent surface temperatures derived from NOAA AVHRR images. Brighter pixels have higher apparent temperatures. (c) Area A with paddy and other vegetation. (d) Area B with residential and factory buildings.

landcover types do not vary with spatial locations, i.e.,

$$T_i(j) = T_i, \quad j = 1, 2, \dots, N \quad (3-33)$$

where  $T_i$ 's represent the landcover-specific apparent temperatures. Such assumption is reasonable since, for a specific landcover type, spatial variation of the apparent temperature within the study area (approximately 21km×13km) is small, and more importantly the effect of landcover types on ambient air temperatures should be assessed on a region scale, not base on individual pixels. Thus, spatial variation of the pixel-average land surface temperatures depends on coverage ratios of different landcover types present in individual NOAA pixels, i.e.,

$$\bar{T}(j) = \sum_{i=1}^k w_i(j) T_i, \quad j = 1, 2, \dots, N \quad (3-34)$$

Or equivalently in matrix form,

$$\begin{bmatrix} \bar{T}(1) \\ \bar{T}(2) \\ \vdots \\ \bar{T}(N) \end{bmatrix} = \begin{bmatrix} w_1(1) & w_2(1) & \cdots & w_k(1) \\ w_1(2) & w_2(2) & \cdots & w_k(2) \\ \vdots & \vdots & \ddots & \vdots \\ w_1(N) & w_2(N) & \cdots & w_k(N) \end{bmatrix} \begin{bmatrix} T_1 \\ T_2 \\ \vdots \\ T_k \end{bmatrix} \quad (3-35)$$

$$\bar{T} = WT \quad (3-36)$$

In the above equation the pixel-average land surface temperatures ( $\bar{T}$ ) can be substituted by the SWT surface temperatures, and thus if the coverage ratios  $w_i (i=1, 2, \dots, k)$  are known, the landcover-specific surface temperatures  $T_i (i=1, 2, \dots, k)$  can be determined by solving the inversion problem with the following least squares estimator:

$$T = (W'W)^{-1} W' \bar{T} \quad (3-37)$$

The pixel-specific coverage ratio ( $W$ ) were obtained by conducting a supervised

landcover classification using high-resolution multispectral SPOT images and orthorectified aerial photos. Implementation of the supervised landcover classification using remote sensing images involves the following steps:

- (1) Determining the landcover types to be specified in the subsequent analysis. Both the landcover conditions present in the study area and the required level of landcover details should be taken into consideration. Four major landcover types—paddy fields (P), water ponds (W), built-up area and bare soils (B), and other vegetations (V) are present in the study area. However, there were also areas covered by clouds (C), and therefore, a total of five landcover types were specified.
- (2) Determining the classification features to be used in classification. The selected features jointly should be able to differentiate different landcover types. SPOT multispectral (green, red, and near infrared) images were chosen as classification features in our study.
- (3) Collecting training pixels of individual landcover types. This is done by making several field investigations and referencing to the aerial photos to identify areas on satellite images which are representative of different landcover types. Digital numbers of training pixels are then extracted to establish the spectral signatures of different landcover types. Such signatures characterize the distribution and variation of digital numbers of individual landcover types in the feature space and form the basis of supervised landcover classification.
- (4) Pixels of unknown landcover types are classified by referencing their digital numbers to spectral signatures of different landcover types. Many classification methods have been developed and the maximum likelihood classification method was used in our study. Details of the supervised classification and the maximum

likelihood classification method can be found in Schowengerdt (1997) and Schott (1997).

Results of landcover classification are assessed by the confusion matrix shown in Table 3-1. It achieves a very high overall accuracy (92.10%) and the user's and producer's accuracies of all landcover types except vegetation (V) are all higher than 86%. Table 3-1 shows some pixels belonging to paddy fields and vegetations are mutually misclassified since their spectral signatures are more similar. Particularly, vegetation pixels are more likely to be classified into paddy fields. Figure 3-4 demonstrates the landcover image resulted from landcover classification using multispectral SPOT images.

The landcover image derived from multispectral SPOT images has a spatial resolution of 20m which is much smaller than the spatial resolution (1.1km) of the NOAA AVHRR images. By overlying NOAA AVHRR images on the landcover image (Figure 3-5), the coverage ratios ( $W_i$ ) of individual landcover types within each NOAA pixel can be determined and landcover-specific surface temperatures  $T_i$  ( $i=1, 2, \dots, k$ ) can be obtained using Eq. (3-37). It should also be noted that NOAA pixels containing classified cloud pixels were excluded in subsequent analysis since coverage ratios of real landcover types in cloud-covered areas cannot be determined. As a result, among a total of 228 NOAA pixels, only 183 pixels ( $N=183$  in Eq. (3-35)) were used for estimation of landcover-specific surface temperatures.

Landcover-specific surface temperatures of the 2 days of field investigation (described in the Section 3.6) are shown in Table 3-2. Using the landcover-specific surface temperatures and within-pixel coverage ratios ( $W_i$ ), pixel-average temperatures can be estimated by Eq. (3-35) and compared against the SWT surface

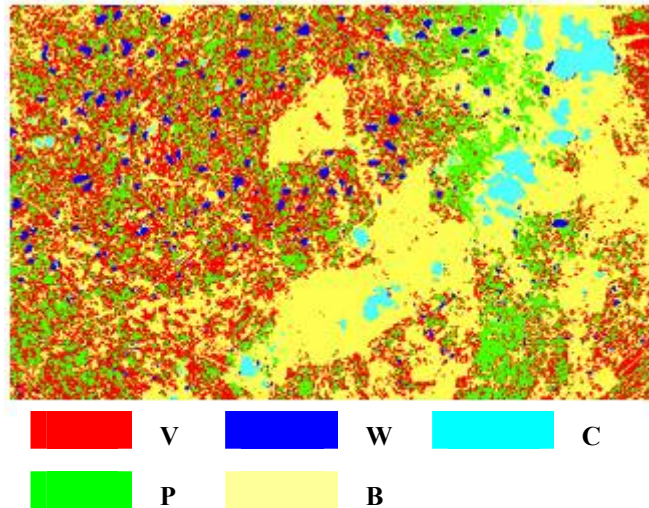


Figure 3-5 Results of landcover classification using multispectral SPOT images (W: water ponds, P: paddy fields, B: built-up, V: other vegetations, and C: clouds).

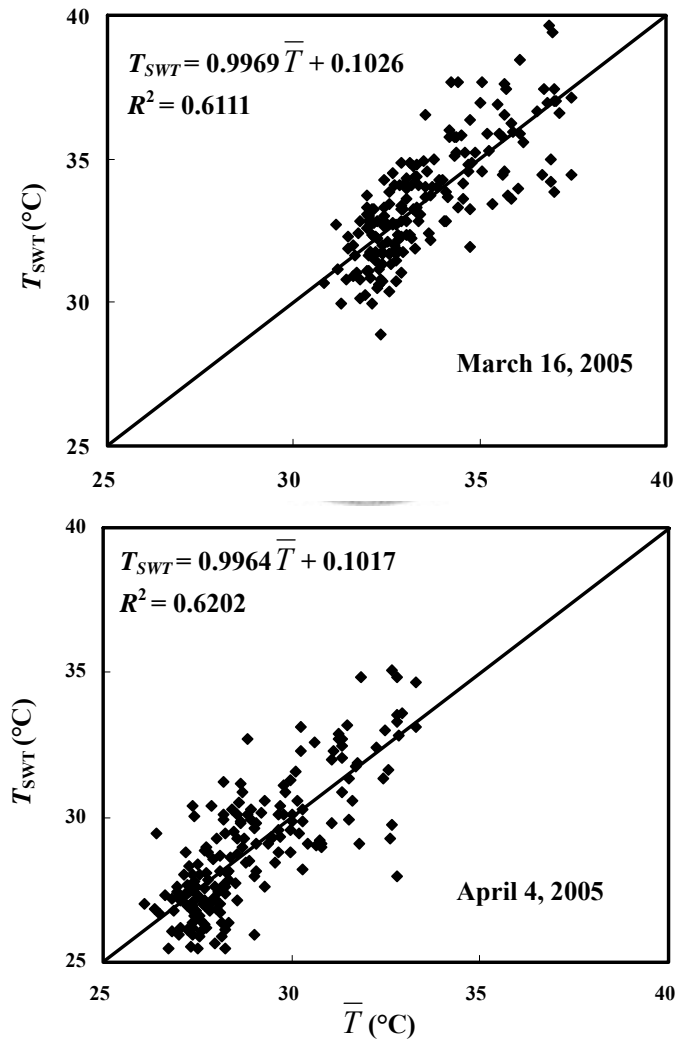


Figure 3-6 Comparison of pixel-average surface temperatures derived by the split window technique ( $T_{SWT}$ ) and estimated using landcover-specific surface temperatures ( $\bar{T}$ ).

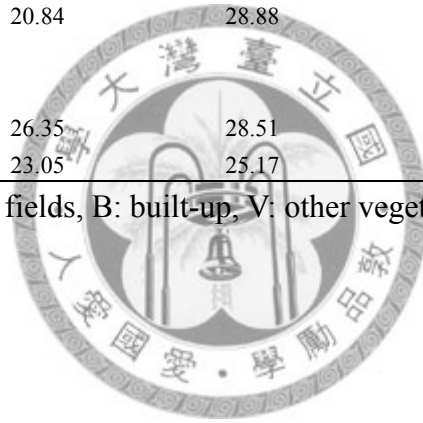
Table 3-1 Confusion matrix of landcover classification using training data.

Classified landcover types	Reference landcover types					Sum	User's accuracy (%)
	W	P	B	V	C		
W	3236	0	11	0	0	3247	99.66
P	0	3963	2	613	0	4578	86.57
B	98	1	5344	13	316	5772	92.58
V	4	487	26	1126	0	1643	68.53
C	0	0	88	0	5669	5757	98.47
Sum	3338	4451	5471	1752	5985	20997	Overall accuracy
Producer's accuracy (%)	96.94	89.04	97.68	64.27	94.72		92.10%

Table 3-2 Estimated landcover-specific surface and air temperatures (°C).

Date	Landcover type			
	W	P	B	V
Surface temperature				
03/16/2005	25.18	33.17	37.49	29.90
04/04/2005	20.84	28.88	33.31	24.65
Air temperature				
03/16/2005	26.35	28.51	29.34	27.77
04/04/2005	23.05	25.17	27.23	23.70

W: water ponds, P: paddy fields, B: built-up, V: other vegetations



temperatures. Figure 3-6 demonstrates the pixel-average surface temperature ( $\bar{T}$ ) estimated by landcover-specific surface temperatures and the SWT surface temperatures ( $T_{\text{SWT}}$ ) are well correlated and the regression lines are almost identical to the line of equivalence (slope and interception of the regression lines are respectively very close to 1.0 and 0), suggesting the applicability of the landcover-specific surface temperatures and coverage ratios within individual NOAA pixels.

### 3.6 Pixel-average air temperature estimation

Field investigations were conducted on 16 March and 4 April 2005 in order to develop landcover-specific relationships for surface and air temperatures. In 16 March the weather is quiet clear, however there is some cloudy in 4 April 2005. During each trip of field investigation surface temperatures of different landcover types and corresponding air temperature at 0.2, 0.4, 0.8, 1.2, 1.6 and 2m above the ground surface were measured by an infrared thermometer. The field investigations were conducted roughly between 11:00 am and 2:30 pm in order to be nearly concurrent with the daytime overpass of NOAA AVHRR sensors. A V-shape sampling route as shown in Figure 3-2 was adopted to take into consideration the spatial variation of temperatures and to cover both north-south and east-west extent of the study area. Land surface and air temperatures of different landcover types were measured at locations near centers of individual aerial photos (see Figure 3-2) along the sampling route. At each location and height, 20 temperatures readings were recorded and the average value was taken as the representative temperature. In order to take the diurnal temperature changes into consideration, a temperature adjustment practice suggested by Yokohari *et al.* (1997) was adopted. Upon completion of temperature sampling along the sampling route, land surface and air temperatures at the starting point were



measured again and all other temperature measurements were adjusted to be consistent with the last measurement by assuming a linear temporal variation of temperatures. Figure 3-7 illustrates vertical air temperature profiles of different landcover types.

Air temperatures above the surface of water ponds have reversed vertical profiles, i.e., the surface temperatures are lower than the air temperatures at different heights. For other landcover types, surface temperatures are higher than air temperatures. In particular, built-up areas have a sharp temperature decrease (about 6-12<sup>0</sup>C) from the ground surface to 20cm above the ground. Paddy fields and other vegetations have much smaller temperatures decrease (about 0.5-3<sup>0</sup>C) at the same height. More specifically, paddy fields seem to have a little larger temperature decrease than vegetations.

Using the above temperature measurements, the following empirical relationships (also shown in Figure 3-8) of land surface temperatures ( $T_s$ ) and air temperatures at 2 m height ( $T_a$ ) with respect to different landcover types were developed:

$$T_a = 0.7748T_s + 2.8106 \quad (\text{paddy fields}) \quad (3-38a)$$

$$T_a = 0.505T_s + 10.407 \quad (\text{built-up}) \quad (3-38b)$$

$$T_a = 0.76T_s + 7.2131 \quad (\text{water ponds}) \quad (3-38c)$$

$$T_a = 0.7747T_s + 4.6043 \quad (\text{other vegetations}) \quad (3-38d)$$

These relationships are needed for calculation of NOAA-pixel-average air temperatures using a procedure illustrated in Figure 3-9 and described below.

Spatial variation of surface temperatures within a NOAA pixel is characterized by the landcover-specific surface temperatures and spatial distribution of different landcover types within the NOAA pixel. The landcover-specific surface temperatures are then converted to landcover-specific air temperatures using the empirical

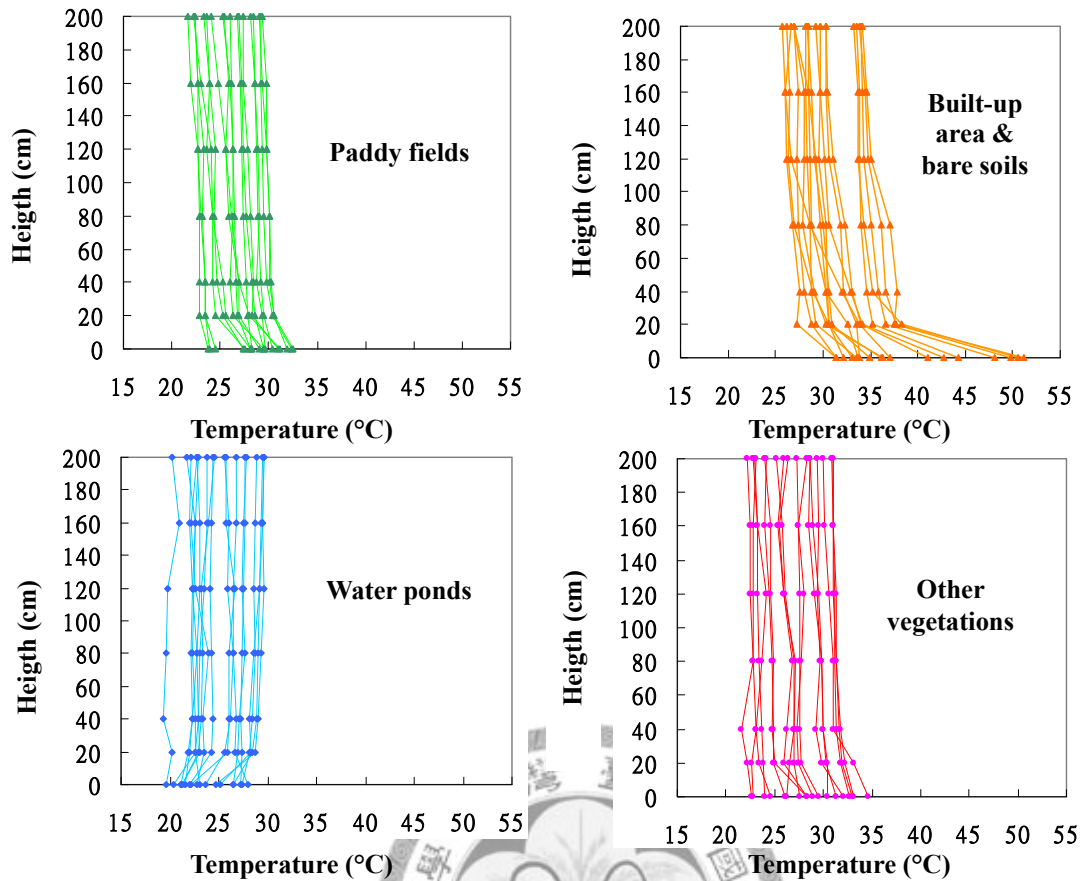


Figure 3-7 Vertical temperature profiles of different landcover types.

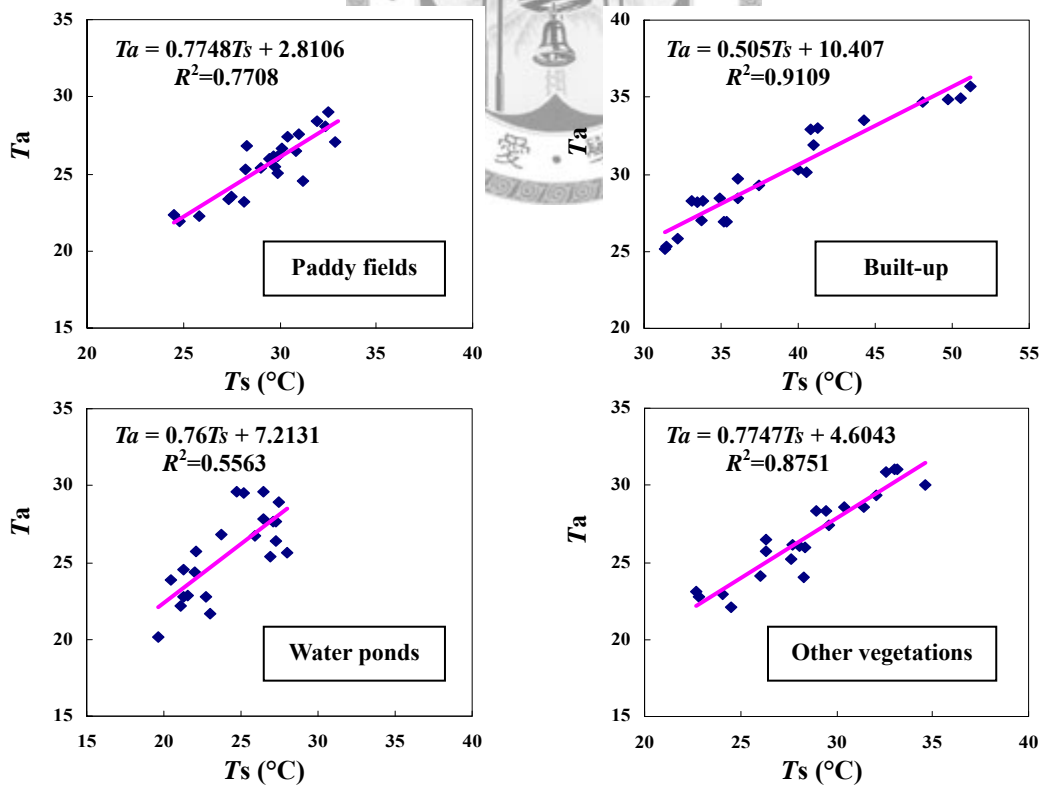
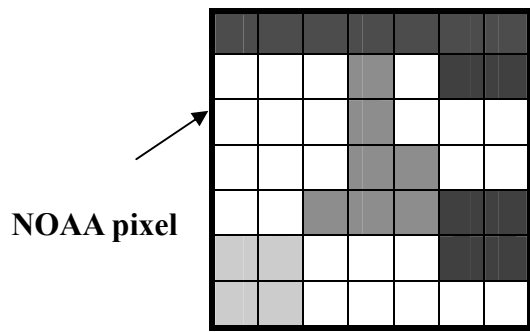
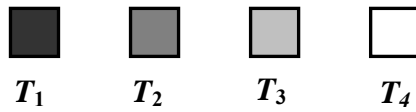


Figure 3-8 Landcover-specific empirical relationship between the air temperature at 2m height ( $T_a$ ) and surface temperature ( $T_s$ ).



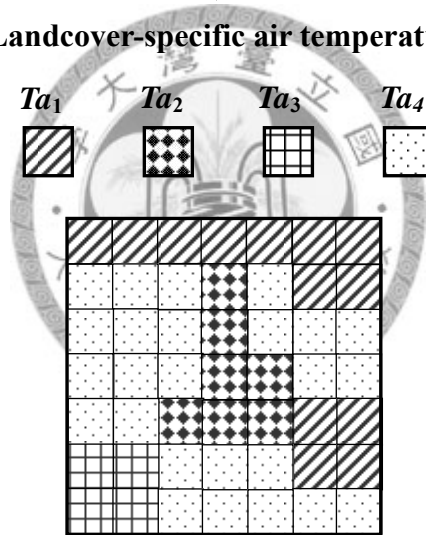
Spatial variation of surface temperatures within a NOAA pixel



Landcover-specific surface temperature

↓ Eq. (3-38)

Landcover-specific air temperature



↓ Eq. (3-39)

Pixel-average air temperature  $\overline{Ta}$

Figure 3-9 Schematic illustration of procedures of calculation of pixel-average air temperature over a NOAA pixel.

relationships of Eqs. (3-38a)-(3-38d). Although empirical relationships between the surface temperatures and air temperatures were derived based on point temperatures measurements, they were also used for converting the landcover-specific surface temperatures (which represent area-average temperatures) to corresponding air temperatures. Finally, the average air temperatures over individual NOAA pixels were calculated as the area-weighted average of landcover-specific air temperatures, i.e.,

$$\bar{T}_a(j) = \sum_{i=1}^k w_i(j) T_{a_i}, \quad j = 1, 2, \dots, N \quad (3-39)$$

where  $\bar{T}_a(j)$  is the average air temperatures of the  $j$ th NOAA pixel,  $T_{a_i}$  the air temperature of the  $i$ th landcover types presents in the  $j$ th NOAA pixel.

Table 3-2 shows the landcover-specific air temperatures at the time of field investigation estimated using the above method. Readers are reminded that the average surface and air temperatures discussed in this paper refer to respective average temperatures over individual NOAA pixels. We consider the size of a NOAA pixel (1.1km×1.1km) is appropriate for assessing the landcover changes and its effect on ambient air temperatures.

### 3.7 Effect of landcover types on ambient air temperatures

Table 3-2 indicates that surface temperatures vary with landcover types. Built-up areas with paved roads and residential and factory buildings have significant higher surface temperatures than other landcover types, while water ponds have the lowest surface temperatures. Surface temperatures of paddy fields are 3-4° higher than that of other vegetations. This may be due to the fact that rice crops in the paddy fields have not formed full canopy coverage at the time of this study. However, with regard to the living environment, it is the ambient air temperature that is of major concern.

Although the built-up landcover has a significantly higher surface temperature than other landcover types, the corresponding air temperature differences are smaller. This is because the built-up landcover has the largest vertical temperature gradient. On 16 March 2005 the maximum air temperature difference (between the built-up areas and the water ponds) was about 3°C, while on 4 April 2005 the maximum difference was about 4.2°C. It is worthy to mention that the differences between landcover-specific surface and air temperatures are also dependent on local climatological condition.

The data in Table 3-2 imply that if an area of NOAA pixel size (1.1km×1.1km) with a complete water ponds coverage is converted to a complete built-up coverage, the ambient air temperature will be raised by about 3°C (29.34-26.35) to 4°C (27.23-23.05). Other kinds of landcover conversions will result in smaller changes on ambient air temperatures. Similarly, if the same area is converted from a full paddy coverage to a complete built-up area, the ambient air temperature rise will be about 0.8°C (29.34-28.51) to 2°C (27.23-25.17). Such arbitrarily hypothesized landcover conversions between two landcover types are referred to as the blind landcover conversions since it may not reflect the actual landcover conditions of the study area. For example, in our study there is no pixel with complete paddy or water coverage.

We argue that landcover conversions will not arbitrarily occur and the likely conversions are often restricted by the local or regional conditions of resources availability, transportation, etc. Within an area of NOAA pixel size, landcover conversions are amore likely to take place among several landcover types, instead of mutual conversion between two landcover types. Prevalent landcover conversions area related to climatological, geographical, economical, sociological, and other factors, and should be considered in assessing the effect of landcover types on ambient air temperatures. Such prevalent conversions often are too complicated to be

characterized by a generally applicable model and should be considered as a local or regional phenomenon. Thus, a locally based assessment of the effect of landcover types on ambient air temperatures is presented below.

Apart from comparing the landcover-specific air temperatures based on blind landcover conversions, another way of assessing the effect of landcover types on ambient air temperatures is by evaluating average air temperatures with respect to coverage ratios of certain landcover types within individual NOAA pixels. Such assessment is similar to Yokohari *et al.* (1997), although in their study temperature differences between 50m×50m cells and a reference urban area with respect to paddy coverage ratios were evaluated.

Figure 3-10 illustrates relationships between pixel-average air temperatures ( $\bar{T}_a$ ) and within-pixel coverage ratios (CR) of different landcover types. All regression lines, particularly the one associated with the built-up landcover type, are very significant, suggesting well-established landcover patterns in the study area. It should be emphasized that, for any given value of average air temperature (e.g., 28.8°C), the sum of corresponding coverage ratios of different landcover types (determined by the regression lines) is always very close to 100%. It indicates the regression lines shown in Figure 3-10 are inter-related and collectively they characterize the existing landcover pattern within the study area. For example, a pixel with 60% built-up coverage is likely to have about 27 and 13% coverage of vegetations and paddy fields, respectively. The maximum coverage ratio of paddy fields within a NOAA pixel is about 26% whereas the maximum coverage ratio of built-up areas reaches near 100% due to the dense population and fully developed industrial and manufacturing parks. It can also be observed that water ponds only exist in areas which are agriculture (paddy fields and other vegetations combined) dominant since they are used as irrigation

water supply. Another important observation of Figure 3-9 is that reduction in paddy and vegetation coverages tend to occur contemporaneously due to decline in agricultural activities, and such reductions are converted to increase of built-up areas. For regions with no well-established landcover pattern, co-existence of the landcover-specific regression lines in Figure 3-9 will not appear.

The increasing (or decreasing) trend of ambient air temperatures with respect to increasing within-pixel coverage ratio of built-up areas (or other landcover types) is apparent. Under the existing landcover pattern (i.e., the pattern of inter-related regression lines in Figure 3-9), the ambient air temperature will rise by 1.7°C (from 27.8 to 29.5 on 16 March) to 3.1°C (from 24.3 to 27.4 on 4 April) if the coverage ratio of paddy fields decreases from its maximum of 26% to none. It may seem unreasonable that this amount of ambient air temperature rise is higher than the 0.8-2°C rise under the blind landcover conversion. This can be explained by considering the existing landcover pattern in the region.

Under the existing landcover pattern of the study area, a pixel with 26% paddy coverage is likely to have 19% water ponds, 51% vegetations, and only 5% of built-up area, resulting in a pixel-average air temperature of 27.8°C (16 March 2005) which is lower than the landcover-specific air temperature of paddy fields (28.51°C). Similarly, when the paddy coverage is reduced to zero, the vegetation coverage will also decrease due to decline of agricultural activities in the area. Reduced coverages of paddy fields and vegetations are converted to built-up areas, causing the pixel-average air temperatures to reach around 29.5°C (very close to the landcover-specific air temperature for built-up areas, 29.34°C). The well-established existing landcover pattern reflects the complex local conditions that sustain the totality of living environment in the region. Blind landcover conversion ignores such existing

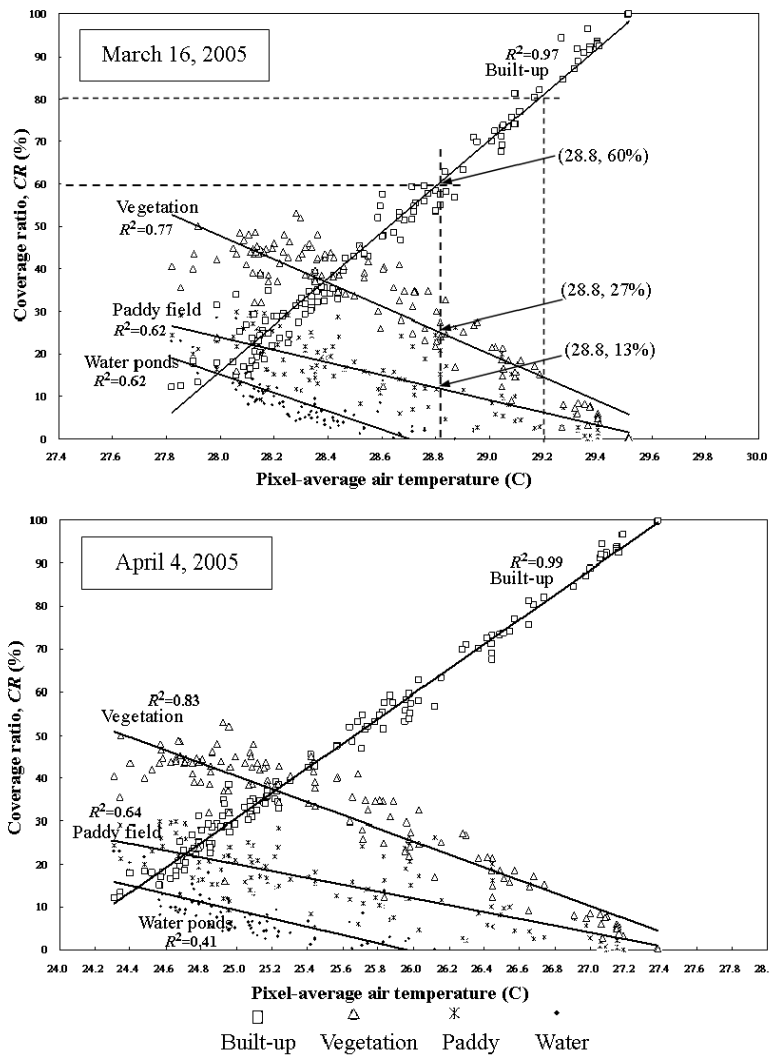


Figure 3-10 Empirical relationships between within-pixel coverage ratios of different landcover types and pixel-average air temperature. The inter-related regression lines collectively characterize the prevalent landcover conversion pattern of the study area.



landcover pattern and will only yield imaginary assessment results. For example, assessing the effect of turning huge areas (several pixels) of all-paddy fields into water ponds is unrealistic since such all-paddy pixels do not exist in the study area. Scenarios contradicting the existing landcover pattern should not be presented for assessment.

We may further consider the situation of changing from an existing landcover condition to a forced landcover condition. Suppose a pixel with existing landcover condition of 26% paddy fields is forced to become 50% of built-up areas and 50% of paddy fields. Under such forced landcover conversion, the average air temperature will be raised from 27.8 to 28.93°C (using landcover-specific air temperatures on 16 March 2005), an increase of 1.13°C. In contrast, if a prevalent landcover conversion (conversion following the existing landcover pattern) is taken, a pixel with 50% built-up coverage (corresponding to 16% and 32% coverages of paddy fields and other vegetation, respectively) has an average air temperature of 28.63°C. The forced conversion results in a higher temperature increase than would be under prevalent conversion.

The concept of different landcover conversions can be better illustrated in a coverage-ratio space as shown in Figure 3-11. Scattering of actual landcover ratios of individual NOAA pixels (points marked by ▲ except C and D) exhibits a pattern which characterizes the existing landcover conditions. Landcover condition of point C is unrealistic and thus landcover conversion from point C to B is a blind conversion. Point A represents an existing landcover condition and conversions from point A to B and D are respectively the prevalent and forced landcover conversions. A forced landcover conversion contradicts the existing landcover pattern and may cause complicated consequences. For instance, conversion from point A to D will force

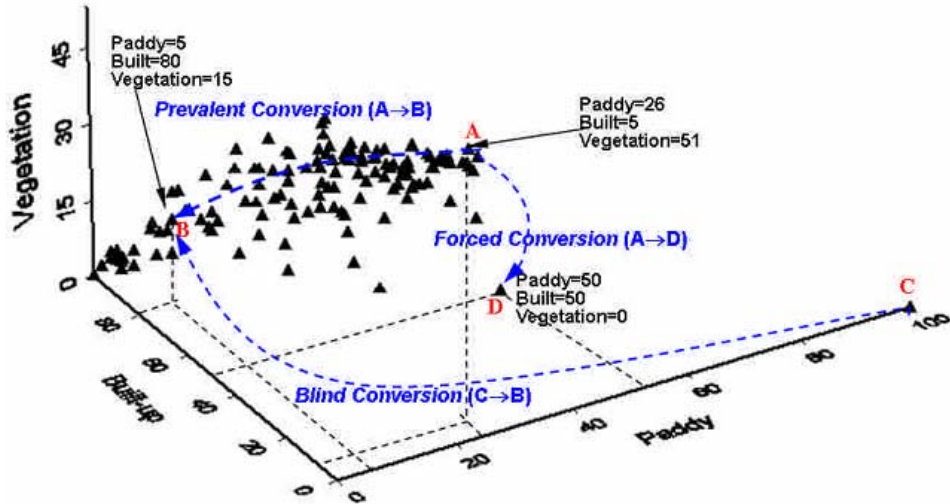
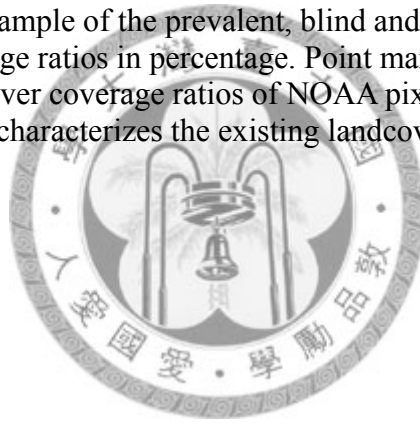


Figure 3-11 Illustrative example of the prevalent, blind and forced conversion. Numbers represent coverage ratios in percentage. Point marked by ▲ (except C and D) represent actual landcover coverage ratios of NOAA pixels in the study area. Scattering of these points characterizes the existing landcover pattern.



landcover types of vegetation and water ponds to disappear and increase the coverage of paddy fields and built-up areas. It may encounter problems such as not having enough water for irrigation and low intention of local farmers to transform from vegetation growing to paddy culture. Additional resources allocation and incentives may need to be introduced in order to ensure a successful forced conversion.

Several final remarks should also be mentioned:

- (1) We recognize that environmental changes are dynamic processes and the existing landcover pattern may gradually change over time. Therefore, long-term monitoring of landcover changes should be pursued.
- (2) Analyses and results of this pilot study were based on data collected in only 2 days of field investigation. It may not reflect the complete range of temperature changes during the full growing period of paddy rice. Therefore, continuation of this pilot study is necessary for a more complete assessment of landcover effect on ambient air temperature in the study area.
- (3) Spatial scattering of different landcover types within a NOAA pixel may also affect the pixel-average air temperatures. Yokihari *et al.* (1997) studied the effect of segmentation of paddy fields on air temperature and found that, for intermediate coverage ratios (30-70%) of paddy fields, segmentation level of paddy fields has strong influence on air temperatures is more complicated and should be pursued in future study.

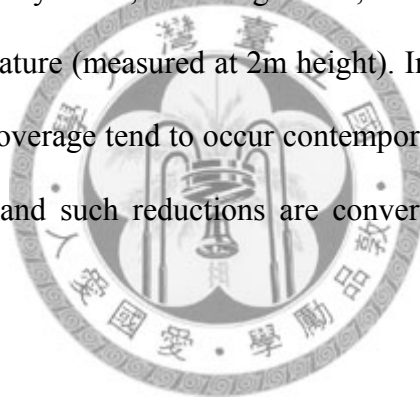
### **3.8 Conclusions**

In this study we present a new method for assessment of landcover effect on ambient air temperature using remote sensing images. The proposed method takes into account the existing landcover pattern. A few concluding remarks are drawn as

follows.

Landcover-specific empirical relationships exist between within-pixel coverage ratios and pixel-average air temperatures. These empirical relationships are inter-related and they collectively characterize the existing landcover pattern of the region. Landcover conversions tend to follow a local prevalent pattern which sustains the totality of the living environment in the region.

In our study, under the prevalent landcover conversion pattern, reduce the coverage ratio of paddy fields from its maximum of 26% to none will result in an ambient air temperature rise of 1.7-3.1°C. Increasing the coverage ratio of built-up areas (or decreasing coverage of paddy fields, other vegetation, and water ponds) will result in rise of ambient air temperature (measured at 2m height). In the study area, reductions in paddy and vegetation coverage tend to occur contemporaneously due to the decline in agricultural activities, and such reductions are converted to increase of built-up areas.

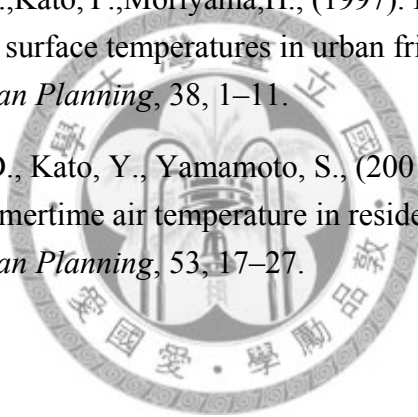


## References

- Chedin, H., Scott, N.A., Berroir, A., (1982). A single channel double-viewing angle method for sea surface temperature determination from coincident METEOSAT and TIROS-N radiometric measurements. *J. Climate Appl. Meteorol.*, 21, 613–618.
- Florio, E.N., Lele, S.R., Chang, Y.C., Sterner, R., Glass, G.E., (2004). Integrating AVHRR satellite data and NOAA ground observations to predict surface air temperature: a statistical approach. *International Journal of Remote Sensing*, 25, 2979–2994.
- Fukuda, S., Hiramatsu, K., Mori, M., (2006). Fuzzy neural network model for habitat prediction and HEP for habitat quality estimation focusing on Japanese medaka (*Oryzias latipes*) in agricultural canals. *Paddy Water Environ.*, 4, 119–124.
- Gallo, K.P., McNab, A.L., Karl, T.R., Brown, J.F., Hood, J.J., Tarpley, J.D., (1993).

- The use NOAA AVHRR data for assessment of the urban heat island effect. *J. Appl. Meteorol.*, 32, 899–908.
- Greppi, M., (2004). Infiltration process and groundwater table rising in a paddy field area. *Paddy Water Environ.*, 2, 171–179.
- Idso, S.B., Jackson, R.D., Reginato, R.J., (1977). Remote sensing of crop yields. *Science*, 196, 19–25.
- Ishikawa, M., Tabuchi, T., Yamaji, E., (2003). Clarification of adsorption and movement by predicting ammonia nitrogen concentrations in paddy percolation water. *Paddy Water Environ.*, 1, 27–33.
- Kerr, Y.H., Lagouarde, J.P., Imbernon, J., (1992). Accurate land surface temperature retrieval from AVHRR data with use of an improved split window algorithm. *Remote Sensing of Environment*, 41, 197–209.
- Li, Z.L., Becker, F., (1993). Feasibility of land surface temperature and emissivity determination from AVHRR data. *Remote Sensing of Environment*, 43, 67–85.
- McMillan, L.M., (1975). Estimation of sea surface temperatures from two infrared window measurements with different absorptions. *J. Geophys. Res.*, 80, 5113–5117.
- Monteith, J.L., Unsworth, M.H., (1990). *Principles of environmental physics*. Edward Arnold.
- Nakanishi, N., (2004). Potential rainwater storage capacity of irrigation ponds. *Paddy Water Environ.*, 2, 91–97.
- Nakasone, H., (2003). Runoff water quality characteristics in a small agriculture watershed. *Paddy Water Environ.*, 1, 183–188.
- Prabhakara, C., Dalu, G., Kunde, V.G., (1974). Estimation of the sea surface temperature from remote sensing in the 11 to 13 $\mu$ m window region. *J. Geophys. Res.*, 79, 5039–5044.
- Price, J.C., (1984). Land surface temperature measurements from the split window channels of the NOAA 7 advanced very high-resolution radiometer. *J. Geophys. Res.*, 89, 7231–7237.
- Saptomo, S.K., Nakano, Y., Yuge, K., Haraguchi, T., (2004). Observation and simulation of thermal environment in a paddy field. *Paddy Water Environ.*, 2, 73–82.

- Schott, J.R., (1997). *Remote Sensing—the Image Chain Approach*. Oxford University Press.
- Schowengerdt, R.A., (1997). *Remote Sensing—Models and Methods for Image Processing*(2<sup>nd</sup> ed.). San Diego: Academic Press.
- Unami, K., Kawachi, T., (2005). Systematic assessment of flood mitigation in a tank irrigated paddy fields area. *Paddy Water Environ.*, 3, 191–199.
- Vasquez, D.P., Reyes, F.J.O., Arboledas, L.A., (1997). A comparative study of algorithms for estimating land surface temperature from AVHRR data. *Remote Sensing of Environment*, 62, 215–222.
- Yokohari, M., Brown, R.D., Takeuchi, K., (1994). A framework for the conservation of rural ecological landscapes in the urban fringe area in Japan. *Landscape and Urban Planning*, 29, 103–116.
- Yokohari, M., Brown, R.D., Kato, Y., Moriyama, H., (1997). Effect of paddy fields on summertime air and surface temperatures in urban fringe areas of Tokyo, Japan. *Landscape and Urban Planning*, 38, 1–11.
- Yokohari, M., Brown, R.D., Kato, Y., Yamamoto, S., (2001). The cooling effect of paddy fields on summertime air temperature in residential Tokyo, Japan. *Landscape and Urban Planning*, 53, 17–27.





## Chapter 4 Forest Drought Monitoring

### 4.1 Introduction

Drought is a complex natural disaster that affects the entire ecosystem. Generally, a drought refers to a period during which the rainfall is lower than the average. Rainfall deficit has different impacts depending on factors such as meteorological conditions, ecosystem type, and social and economic circumstances (McVicar and Jupp, 1998). According to McVicar and Jupp (1998), there are four major types of drought. They are as follows:

1. Meteorological drought. This is generally regarded as a period during which lower than average precipitation is received. The time period is related to meteorological condition and ecosystem type; in some cases air temperature and precipitation anomalies may be combined.
2. Agricultural drought. It occurs when the total quantity of available water, i.e. the precipitated water and the water stored in the soil, falls below that required by a plant community during the critical growth stage. This leads to below average yields in both pastoral and grain-producing regions.
3. Hydrologic drought. This is generally defined by one or a combination of factors such as stream flow, reservoir storage and groundwater.
4. Socioeconomic drought. This is defined in terms of loss from an average or expected return. This can be measured by both social and economic indicators.

In Taiwan, drought has been studied from the meteorological (Lin, 2007), agricultural (Chung *et al.*, 2005), and hydrological (Liu, 1994) perspectives. From the meteorological point of view, the application of an index provides a comparable and



easily understood categorization of rainfall anomaly. Among the numerous meteorological precipitation indices, the standard precipitation index (SPI) proposed by McKee (1993) is one of the most commonly used indices to describe the anomalies in rainfall. Advantages of the SPI include simplicity and time scale variability, which make it suitable for quantifying most types of drought events. Therefore, the SPI is used to assess the precipitation anomalies in this study.

Details of apply remotely sensed data to monitor drought events have been suggested and validated in numerous literature (Kogan, 1995a, 1995b, 1997, 1998; Unganai and Kogan, 1998a, 1998b; Singh *et al.*, 2003). Study of drought (water stress) effect on vegetation can be traced back to Idso *et al.* (1977). They proposed an index which is a summation of the difference between the canopy temperature and the ambient air temperature during the growing season of wheat. They then proposed the crop water stress index (CWSI) for assessing crop health and establishing irrigation scheduling at the field scale. The CWSI is defined as one minus the ratio of daily actual to daily potential evapotranspiration. Since the CWSI was proposed, numerous studies have used it for many different types of crop (Idso, 1982; Su, 2004). Su (2004) applied the CWSI in rice paddy fields and concluded that during water stress, the rice canopy temperature increases and the chlorophyll concentration of the leaves decreases after several days. The characteristics of drought (or water stress on vegetation) agree with the experimental results of several authors (Moran *et al.*, 1994; McVicar and Jupp, 1998).

The key indicators of the effect of drought on vegetation are the spectral vegetation indices and the temperature indices. The most commonly used vegetation index is the normalized difference vegetation index (NDVI), which is well correlated to the pigment amounts in vegetation (Gitelson and Merzlyak, 1997). Kogan (1995a)

proposed vegetation condition index (VCI), which is a percentage of NDVI values at a specific time with respect to the pixel-based maximum NDVI amplitude. Some authors show that there is a lag time from insufficient water supply (or rainfall) to the reduction in chlorophyll content (McVicar and Jupp, 1998). During the lag time, the NDVI has a limited ability to assess drought conditions. However, surface temperature may play an alternative role.

Kogan (1995a) also proposed the temperature condition index (TCI), which uses surface temperature information to assess drought conditions. McVicar *et al.* (1992) and Jupp *et al.* (1998) developed the normalized difference temperature index (NDTI), which depends on modeling two surface temperatures if there is an infinite and zero surface resistance. These surface temperatures can be considered as the upper and lower limits.

In the literature, there are two major combinations of thermal and reflective data for drought assessment. The first is an integration of the VCI and TCI by a linear combination and it yields a vegetation health index (Kogan, 1995a, 1995b, 1997, 1998a, 1998b, 2000). Kogan mentions that the coefficients of the VCI and TCI are a function of the type of vegetation and others environmental factors. The second method is to construct a triangle shape in vegetation index and temperature space (VI-Ts). The details of VI-Ts space will be discuss in section 4.3.

In this study, we identify the drought and non-drought years using SPI. Six SPOT (Satellite Pour l'Observation de la Terre) satellite images with a spatial resolution of 20 m were taken in each May from 1999 to 2004 and were used to classify drought severity. In addition, series of AVHRR (Advanced Very High Resolution Radiometer) images taken in year 2002 and 2004 were used. The AVHRR images can be used to

calculate surface temperature and vegetation index. Therefore, AVHRR images are utilized to construct a VI-Ts diagram, and an upgraded version of the VI-Ts diagram is proposed in this study.

## 4.2 Study Area and Materials

The forest area in the upstream basin of the Shihmen reservoir is selected as the study area (Figure 4-1). One meteorological station, GaoYi station (21C080), is selected to represent the forest area upstream from the Shihmen reservoir. The precipitation records of the station, which have been kept for more than 30 years, are collected.

The acquisition dates of the SPOT images and relative information are given in Table 4-1 and the six SPOT false-color images are given in Figure 4-2. For SPOT images, there are four spectral bands: green (0.51–0.59  $\mu\text{m}$ ), red (0.61–0.68  $\mu\text{m}$ ), near infrared (0.79–0.89  $\mu\text{m}$ ), and short wave infrared (1.58–1.75  $\mu\text{m}$ ), and a 20 meter spatial resolution. Every SPOT image is geometrically rectified, and the error of rectification is less than 10 meters. Other satellite images, with coarser spatial resolution (1.1 km at nadir) are also collected. Several AVHRR images taken in 2002 and 2004 are obtained from the Center for Space and Remote Sensing Research, National Central University. Thirty-nine images with less cloud covered are selected in year 2002, and 30 images for the year 2004; the dates of the selected images are listed in Table 4-2. AVHRR data include five spectral bands—red (0.58–0.68  $\mu\text{m}$ ), near infrared (0.725–1.1  $\mu\text{m}$ ), mid-wave infrared (3.55–3.93  $\mu\text{m}$ ), and two thermal channels (10.3–11.3  $\mu\text{m}$  and 11.5–12.5  $\mu\text{m}$ )—and provide information about vegetation and surface temperature.

The AVHRR data are preprocessed using WinChips software, which coordinates

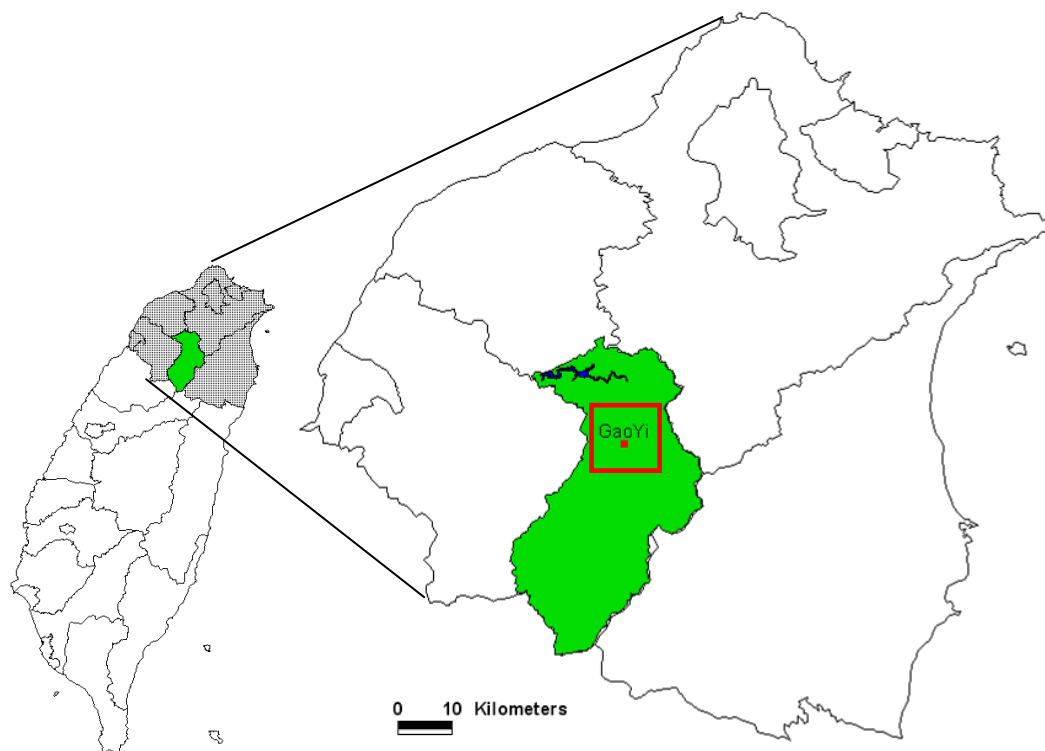


Figure 4-1 Northern Taiwan and the upstream basin of the Shihmen reservoir.

Table 4-1 SPOT images used in this study.

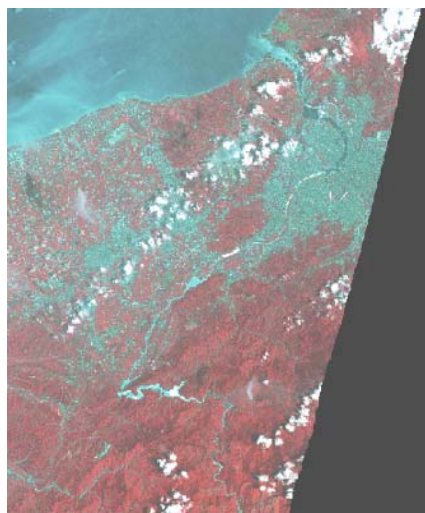
Sensor	Date	Physical gain value			Minimum radiance ( $W / m^2 \times \mu m \times sr$ )		
		Band 1	Band 2	Band 3	Band 1	Band 2	Band 3
SPOT-4	1999/05/11	1.935	2.28786	2.42568	26.17	11.80	10.31
SPOT-4	2000/05/09	1.467	1.83253	0.876*	31.36	18.01	22.83
SPOT-4	2001/05/25	1.4085	1.78991	1.93605	43.31	24.02	9.30
SPOT-4	2002/05/29	1.3545	1.76272	1.2735	31.91	18.15	7.85
SPOT-4	2003/05/07	1.3545	1.76272	1.2735	36.18	15.32	6.28
SPOT-2	2004/05/11	1.43772	1.2662	1.15374	70.94	18.95	17.33

\*: Extremely low physical gain value due to different mode setting when the image was acquired.

Table 4-2 Selected AVHRR images with less cloud cover.

Dates of AVHRR image			
2002		2004	
2002-01-04-0511*	2002-07-22-0416	2004-01-03-0555	2004-07-06-0425
2002-01-06-0450	2002-07-24-0533	2004-01-04-0544	2004-07-24-0558
2002-01-10-0547	2002-08-19-0410	2004-01-10-0437	2004-07-25-0546
2002-02-17-0540	2002-08-27-0422	2004-02-10-0526	2004-08-01-0429
2002-02-22-0446	2002-08-28-0411	2004-02-14-0442	2004-08-03-0544
2002-02-26-0405	2002-08-29-0401	2004-02-22-0451	2004-11-20-0506
2002-03-07-0546	2002-09-17-0530	2004-03-11-0448	2004-11-29-0503
2002-03-08-0357	2002-09-18-0519	2004-03-22-0603	2004-12-02-0608
2002-04-06-0521	2002-10-14-0533	2004-04-11-0536	2004-12-09-0450
2002-04-08-0459	2002-10-15-0522	2004-04-21-0523	2004-12-11-0605
2002-04-14-0534	2002-10-16-0511	2004-05-03-0448	2004-12-12-0554
2002-04-15-0523	2002-11-05-0450	2004-05-11-0638	2004-12-13-0543
2002-04-22-0409	2002-11-08-0418	2004-05-16-0540	2004-12-16-0509
2002-04-23-0537	2002-11-09-0408	2004-06-02-0548	2004-12-29-0600
2002-05-02-0401	2002-12-04-0430	2004-06-10-0557	
2002-05-10-0552	2002-12-05-0420	2004-06-28-0553	
2002-06-19-0515	2002-12-13-0431		
2002-06-21-0453	2002-12-14-0559		
2002-06-24-0601	2002-12-15-0548		
	2002-12-17-0526		

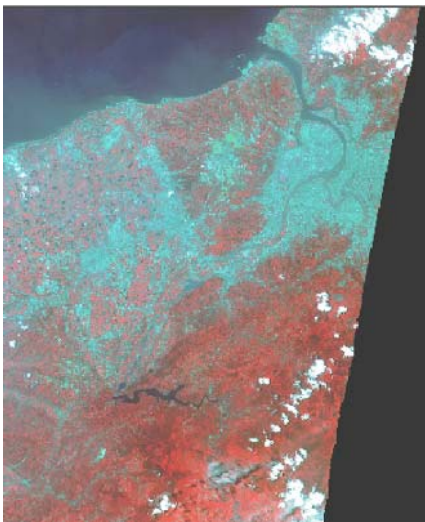
\*: The last four digits represent the Greenwich Mean Time (GMT) of image acquired.



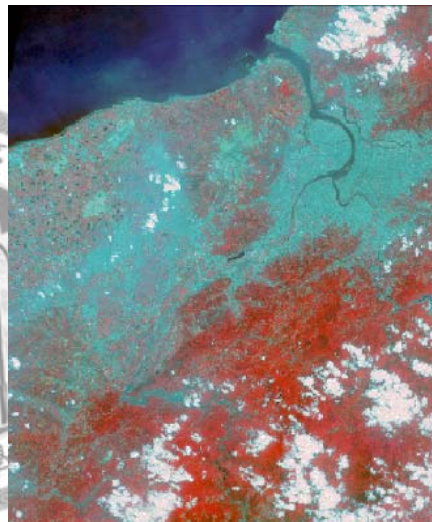
1999



2000



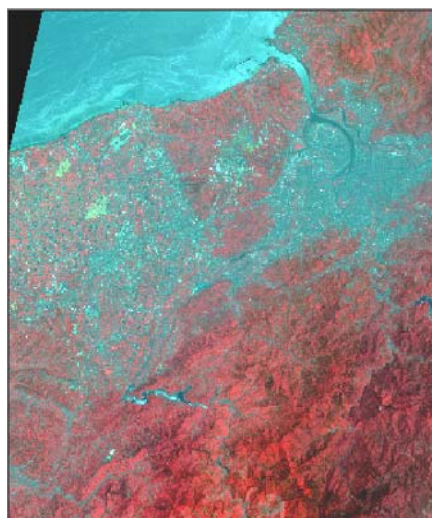
2001



2002



2003



2004

Figure 4-2 False-color representations of SPOT images from 1999 to 2004.

the images into a longitude and latitude system. The WinChips output data are albedos for two visible channels and brightness temperatures for three infrared channels. However, the largest geometric registration error of the output images may be as large as 10 km. Therefore, manually geometric registration of each AVHRR image is conducted by selecting several ground control points (GCPs) around the boundary of Taiwan and controlling the registration error to within 1.1 km.

Besides the registration problem, the other difficulty for land resource monitoring is the presence of cloud cover in the study area. Cloud screening plays an important role in series satellite images applications. Therefore, a standard and efficient cloud screening procedure is necessary. Saunders and Kriebel (1988) applied a radiance band ratio, channel 2 divided by channel 1, and determined a threshold to identify cloud pixels in an AVHRR image. Welch (1998) mentioned that the spatial variability of the spectral signal increases when cloud cover present in an image. He utilized the GLCM (Gley Level Co-occurrence Matrix) method to assess the spatial texture of cloud. The variables of the GLCM, including angular second moment (*ASM*), contrast (*CON*), and entropy (*ENT*), are commonly used in texture analysis. The other method for cloud screening is based on the physical characteristics of clouds. However, prior knowledge is needed for the physical-based method.

The cloud screening procedure (see Figure 4-3) proposed in this study combines the reflective spectral features of cloud and the spatial texture characteristics. We assume that when cloud presents in a pixel, the sensor-received reflective radiance and the spatial contrast will increase. We exclude the feature of low cloud top temperature because the cloud top temperature may vary with seasons and types of cloud. The thresholds of channel 1 and channel 2, albedos equal to 15%, are first applied. If there is a pixel for which the albedos of channel 1 ( $a_1$ ) and channel 2 ( $a_2$ ) are both larger

than 15%, the pixel is probability covered by clouds; otherwise, the pixel will be assigned to a land surface. The next step is to calculate the band ratio (also called Q value) by the radiances received by channel 1 and channel 2, which can be expressed as (Saunders and Kriebel, 1988)

$$Q = \frac{I_2}{I_1} \quad (4-1)$$

where  $I_1, I_2$  are the received radiances of channel 1 and channel 2. The relationship between radiance and albedo is expressed as

$$a_i(\%) = \frac{100\pi I_i}{F_i} \quad (4-2)$$

where the subscript represents the number of the channel ( $i=1,2$ ).  $a_i$  is the albedo of channel 1 or channel 2 in percentage, and  $F_i$  is the extra-terrestrial solar irradiance in channel 1 or channel 2. The values of  $F_1$  and  $F_2$  are 133.2 and 243.1 (W/m<sup>2</sup>), respectively. The thresholds of Q value given by Saunders and Kriebel, 0.75~1.6, are modified to 1.0~2.5 which is more suitable for application in Taiwan. If a pixel's Q value is within the suggested threshold, the pixel will be assigned to cloud covered; otherwise, the pixel will be considered to represent land surface. After the above two steps, the pixels covered by thick cloud are identified. Thus, the pixels covered by thin cloud and near the boundary of the cloud mass are not filtered. To resolve this problem the contrast texture (CON) is applied which is sensitive to the boundary of cloud mass and some kinds of thin cloud. Therefore, the third step is to calculate the contrast texture, which is defined as

$$CON(\theta, d) = \sum_{g=0}^M g^2 \left[ \frac{h(\theta, d, g)}{N} \right] \quad (4-3)$$

where  $N$  is the total number of pixels, and  $d$  and  $\theta$  are the distance and angle,



respectively, which are determined from a  $3 \times 3$  window (Figure 4-4). The  $g$  is the gray level and  $M$  is the maximum gray level presented in an image. The  $CON$  texture is calculated by the albedo of channel 2 (near infrared band) in this study. The maximum  $CON$  value may be larger than 30000 and varies with the images. We normalized the  $CON$  value by the maximum  $CON$  value ( $CON_{max}$ ), which is expressed as

$$CON_N = \frac{CON}{CON_{max}} \quad (4-4)$$

where the  $CON_N$  represents the normalized  $CON$  value. The selected threshold value of the  $CON_N$  equals 0.23. This value is given somewhat arbitrarily, but is capable of screening thin clouds and the boundary area of cloud mass (Figure 4-5).

### 4.3 Drought indices

McKee *et al.* (1993) developed the SPI to quantify precipitation deficits on multiple time scales. A drought event is defined as a period in which the SPI is continuously negative and the SPI reaches a value of -1.0 or less. The SPI is uniquely related to probability and corresponds to drought categories with specific SPI ranges (Table 4-3). The major advantages of the SPI are simplicity and time scale variability, which make the SPI suitable for quantifying most types of drought event. Gamma distribution is applied to describe precipitation data by McKee *et al.* (1993). However, Lana *et al.* (2001) suggested that other distributions, such as Poisson-gamma distribution or log-normal distribution, may be better models. Exponential distribution belongs to gamma distribution family, which is also skewed to the right and non-negative. Exponential distribution is selected to describe precipitation in this study. Kolmogorov-Smirnov (K-S) test is utilized to assess the goodness of exponential

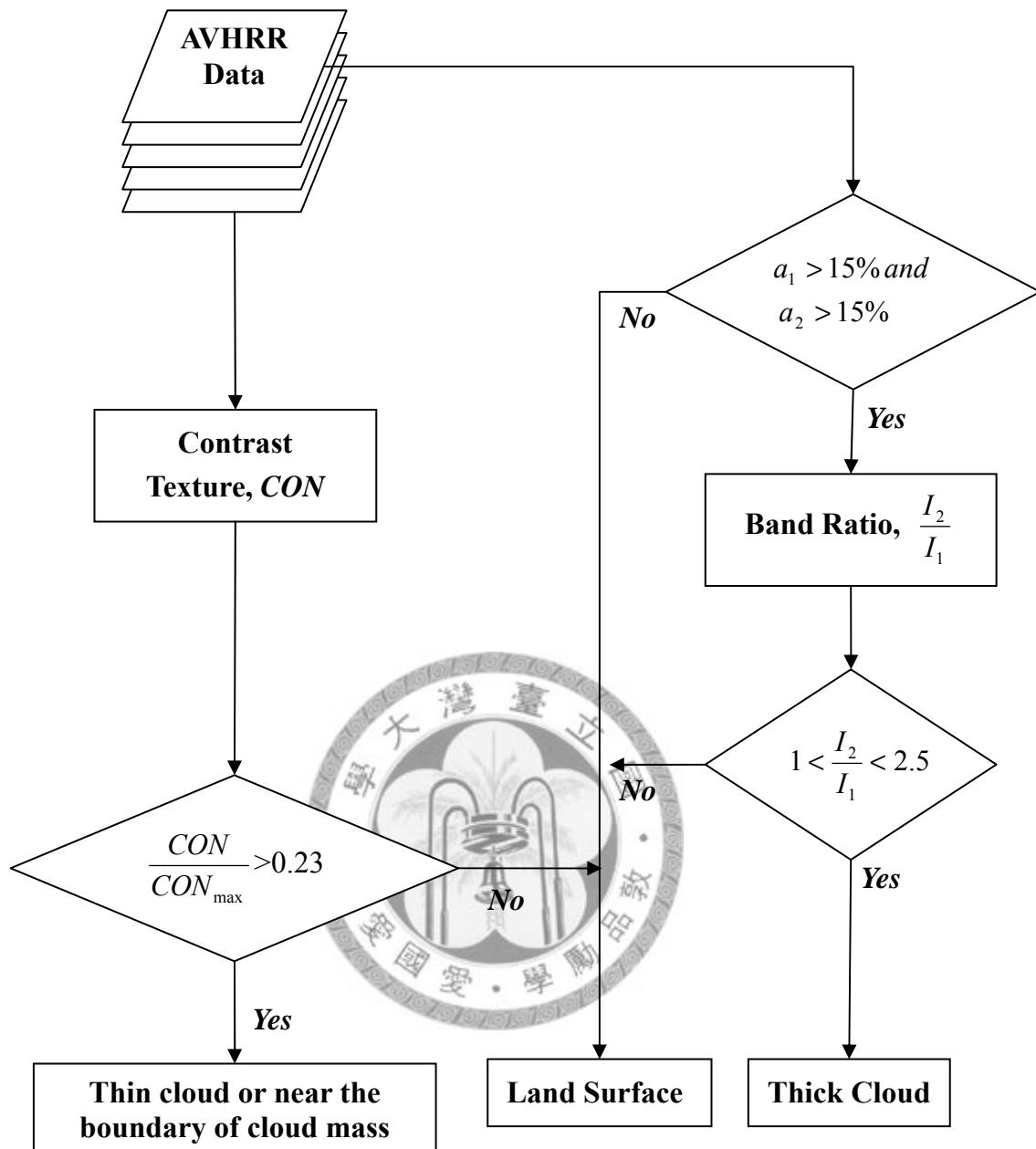


Figure 4-3 The proposed cloud screening procedure.

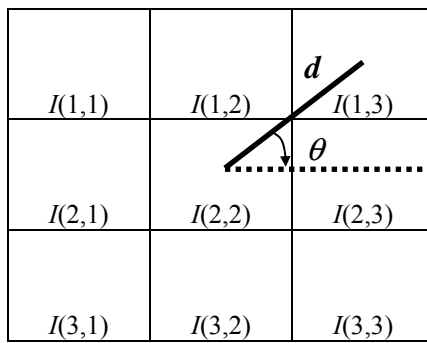


Figure 4-4 A schematic three-by-three window for texture calculation.

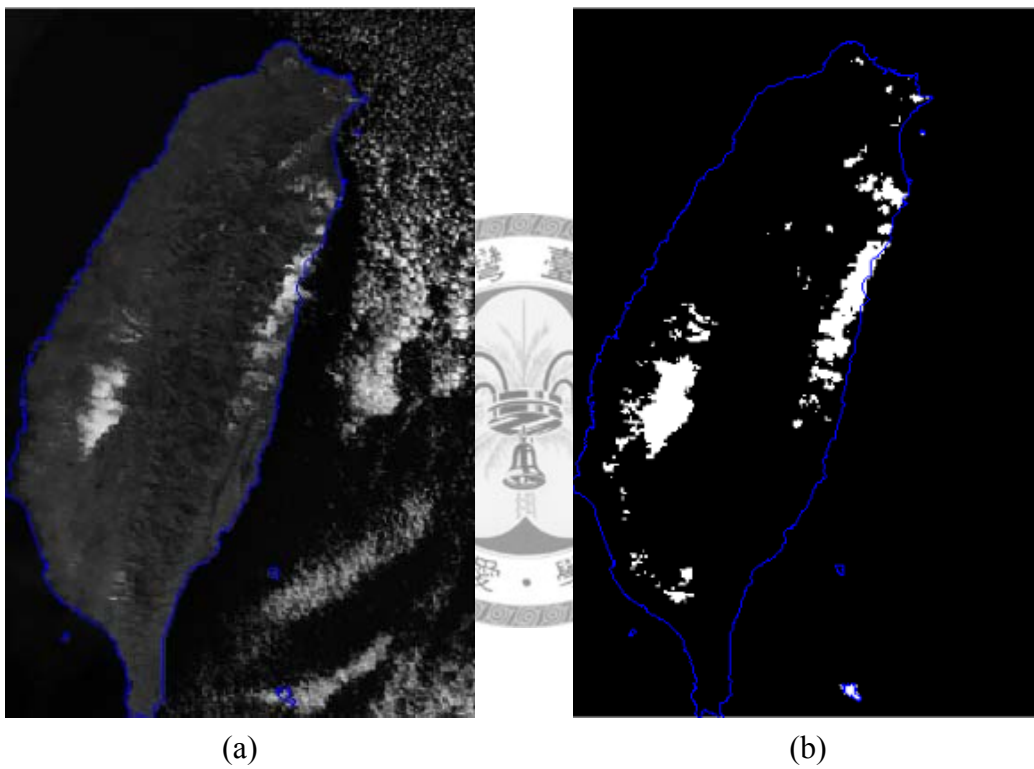


Figure 4-5 Example of cloud screening using the image acquired on 2004/02/10 (a) Channel 2, and (b) the cloud mask image (White pixels represent cloud).

distribution fit the precipitation (Eq. 4-5).

$$f(x) = \begin{cases} \lambda e^{-\lambda x} & , x > 0 \\ 0 & , x \leq 0 \end{cases} \quad (4-5)$$

$$F(x) = 1 - e^{-\lambda x} \quad (4-6)$$

Eq. 4-6 is the cumulative distribution function (CDF) of Exponential distribution which is further converted to a normalized value

$$SPI = Z = G^{-1}(F(x)) \quad (4-7)$$

where  $G^{-1}(\cdot)$  is the inverse standard normal cumulative distribution function.

In order to quantify the severity of drought, McKee et al. (1993) defined a measurement of the accumulated magnitude of drought, drought magnitude (DM) as

$$DM = - \left[ \sum_{j=1}^x SPI_j \right] \quad (4-8)$$

where  $x$  is the duration of drought.

Most satellite remote sensing in vegetation study has applied the vegetation index to assess vegetation health and growing conditions. One of the most commonly used vegetation indices is NDVI, which can be expressed as

$$NDVI = \frac{IR - R}{IR + R} \quad (4-9)$$

where IR and R represent the data in the near infrared band and visible red band, respectively. The data type of red and near infrared channel used for calculating NDVI can be reflectance, radiance, or gray level.

The other commonly used index to assess the water status of vegetation is the surface temperature. For the theoretical details on estimating the surface temperature

using AVHRR data, please refer to section 3-4. The estimation of surface temperature ( $T_s$ ) applied in this study is suggested by Gallo *et al.* (1993), and can be expressed as

$$T_s = T_4 + 3.3(T_4 - T_5) \quad (4-10)$$

where  $T_4, T_5$  are the brightness temperature of the thermal channels of AVHRR data.

Eq. (4-10) is exactly the same with Eq. (3-31).

The combination of vegetation index and surface temperature to assess vegetation growing condition is based on the relationship between the slope of the  $T_s$ /NDVI and canopy resistance (Nemani *et al.*, 1993). The schematic plot of VI- $T_s$  space and its conceptual relationships with evaporation, transpiration and fraction vegetation cover are shown in Figure 4-6.

#### 4.4 Results and discussion

The SPI series of the GaoYi station with a 10-day period time scale from 1999 to 2004 is shown in Figure 4-7. The corresponding acquisition dates of SPOT images in May are also shown in Figure 4-7. A negative value of SPI represents that the precipitation is lower than the normal level. In 2002, before the SPOT image was acquired, sequential negative SPI values were observed from February to May, which period is within the dry season of Taiwan. The sequential negative SPI values indicate to mild to moderate drought and last for almost four months. A similar phenomenon is found in 2003. However, there is an intensive rainfall one month before the SPOT image is acquired. Therefore, from a meteorological perspective, the drought condition from February to May 2003 is not as severe as in 2002. Other than 2002, all of the years are considered as non-drought years (or wet years) in a meteorological sense.

#### 4.4.1 Drought classification using SPOT image

The vegetation indices derived from SPOT images are used to classify drought conditions. Six years of SPOT images have been as geometrically rectified. The gray level of each pixel in the SPOT image is converted to the sensor-received radiance by the specific gain value shown in Table 4-1. The minimum histogram method is used to correct the atmospheric effect. After atmospheric correction, six vegetation indices are compared using the same foundation. In order to extract the pixels that represent vegetation, we classified the SPOT images, using the maximum likelihood classifier, into four classes: vegetation (V), built-up or bare soil (B), water (W), and cloud (C) (Figure 4-8). Pixels classified as vegetation over the six years were extracted, and the histograms are compared in Figure 4-9. In Figure 4-9, the histogram for the year 2000 is significantly lower than all the other distributions. It is probability due to its extremely low physical gain value compared to those of others images (Table 4-1). The reason for the extremely low physical gain is to compress the range of receiving radiance. However, an inappropriate gain setting may result in an over-compressed gray level. Therefore, the data for the year 2000 are excluded in the following analysis.

Base on SPI results in Figure 4-7, we accumulated the SPI one to three months before the date when SPOT images were taken. Assuming that each 10-day period SPI value is independent, the cumulative SPI follows the normal distribution. The original SPI is standard normally distributed with the mean of zero and the variance of one, the cumulative SPI can be expressed as

$$SPI(n) = \sum_{i=1}^n SPI_i, \quad SPI(n) \sim N(0, n) \quad (4-11)$$

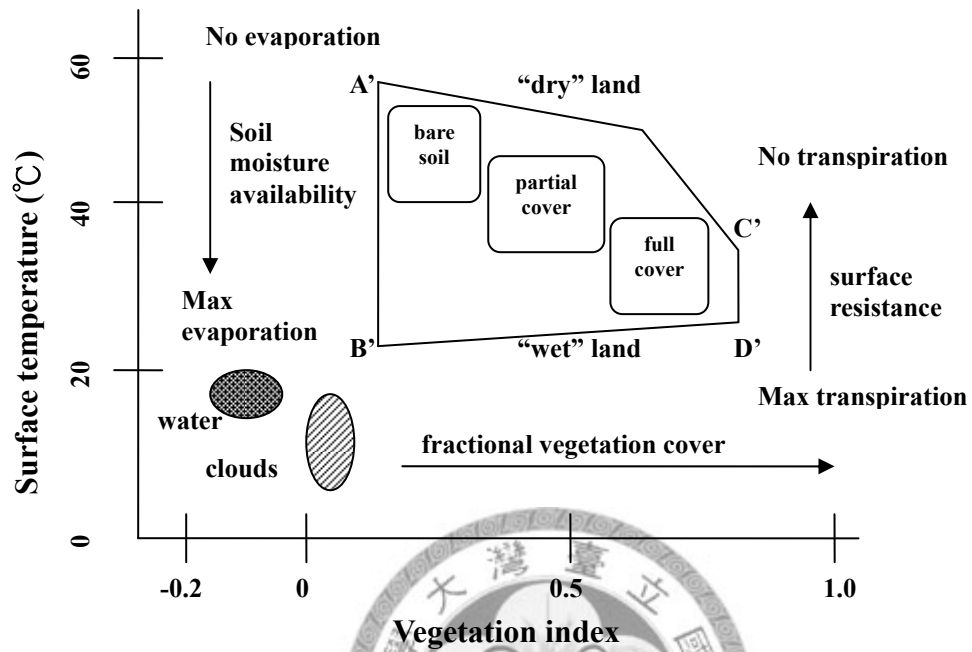


Figure 4-6 Schematic plot of VI-Ts space. (Reproduced from McVicar and Jupp, 1998).

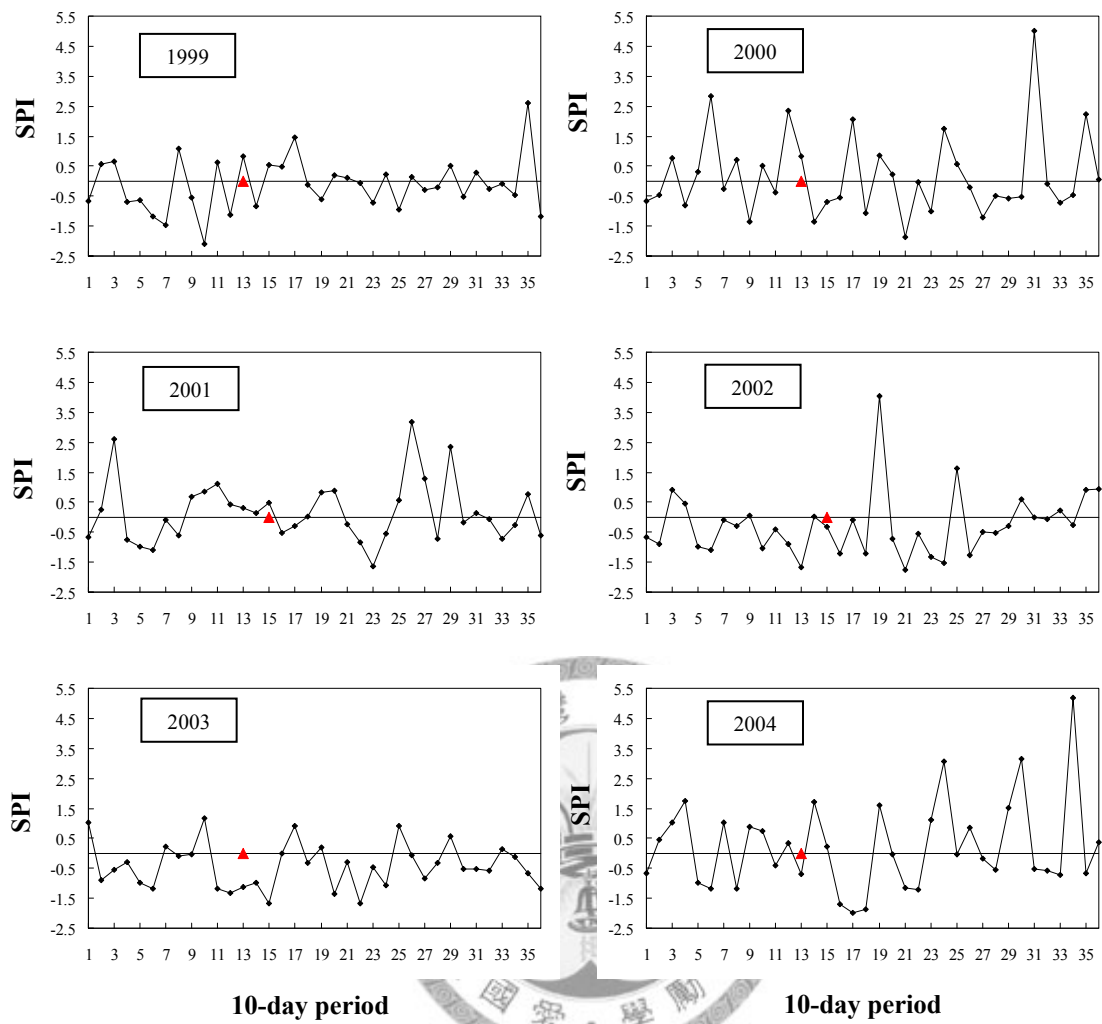


Figure 4-7 The SPI series for GaoYi station with a 10-day period time scale from 1999 to 2004 (The triangles show the corresponding SPOT image acquisition dates).



where  $SPI(n)$  represents the cumulative SPI for  $n$  steps (10-day periods) before the date when SPOT images were taken. Where  $SPI(n)$  is normally distributed with the mean of zero and the variance of  $n$ . The cumulative SPI is further standardized as

$$SPI^n = \frac{SPI(n)}{\sqrt{n}}, \quad SPI^n \sim N(0,1) \quad (4-12)$$

where  $SPI^n$  represents the standardized cumulative SPI, which is standard normally distributed with zero mean and variance equals one. The upper subscript represents the  $n$  steps, 10-day periods, that SPI cumulated. Therefore, the  $SPI^n$  can refer to the drought categories that McKee proposed in 1993.

Figure 4-10 shows the trends of the average NDVI and the standardized cumulative SPI. Except year 2000, the variation of average NDVI agrees with the SPI series that accumulated more than one month. Involving drought duration and magnitude, drought severity quantified by the standardized cumulative SPI which can be applied to McKee proposed drought categories.

In order to classify drought severity by forest NDVI value, the relationships between the average NDVI and the standardized cumulative SPI with various cumulative periods were showed in Figure 4-11 and can be expressed as

$$\begin{aligned} SPI^1 &= 6.08NDVI - 5.28 & R^2 &= 0.11, \quad p=0.593 \\ SPI^3 &= 17.62NDVI - 15.41 & R^2 &= 0.53, \quad p=0.163 \\ SPI^6 &= 23.28NDVI - 20 & R^2 &= 0.77, \quad p=0.052 \\ SPI^9 &= 24.46NDVI - 21.46 & R^2 &= 0.78, \quad p=0.046 \end{aligned} \quad (4-13)$$

The r-square value of regression line is getting higher while the cumulative periods longer. With a significant level of 0.05, only  $SPI^9$  is significant. After relating the NDVI to SPI, the drought categories of NDVI, correspond to of original SPI, is proposed in Table 4-4.

#### 4.4.2 Comparison between NDVI values derived from SPOT and AVHRR

A finer spatial resolution satellite image, such as a SPOT image (20 m spatial resolution), reveals the details of land cover types. However, the entire coverage of a single scan is only capable of local-scale study. The AVHRR images, with 1.1km spatial resolution, cover about a 2400 km scan band width and are applied for the large-scale monitoring purposes. A comparison between NDVI values derived from SPOT and from AVHRR is given in this study. One single SPOT image is chosen to compare with a simultaneously taken AVHRR image on 11 May 2004. The SPOT image is presented in false color (Figure 4-12(a)). The area for comparison is covered by three major land cover types, built-up, vegetation and a few water bodies, which are classified by the maximum likelihood classifier (Figure 4-12(b)). The NDVI map derived from AVHRR is then produced by the albedo values of channel 1 and channel 2 (Figure 4-12(c)); in contrast, the NDVI map derived from SPOT images is produced by the sensor-received radiance (Figure 4-12(d)). For comparison purposes, an average filter of size 55 by 55 goes through the NDVI image derived from SPOT, and yields a 1.1km resolution averaged NDVI map (Figure 4-12(e)). The NDVI map derived from AVHRR image (Figure 4-12(c)) and filtered SPOT image (Figure 4-12(e)) show a consistent pattern. The NDVI value is lower in built-up areas and higher in vegetation covered areas. In an NDVI map with finer spatial resolution (Figure 4-12(d)), the NDVI value in the water body, Shihmen reservoir, even reveals a negative value. The relation between NDVI values derived from AVHRR images and filtered SPOT images is presented in Figure 4-13. A linear relationship between the two NDVI values is modeled using the regression method

$$NDVI_N = 0.075 + 0.343 \times \overline{NDVI}_S \quad (R^2 = 0.74, N=735) \quad (4-14)$$

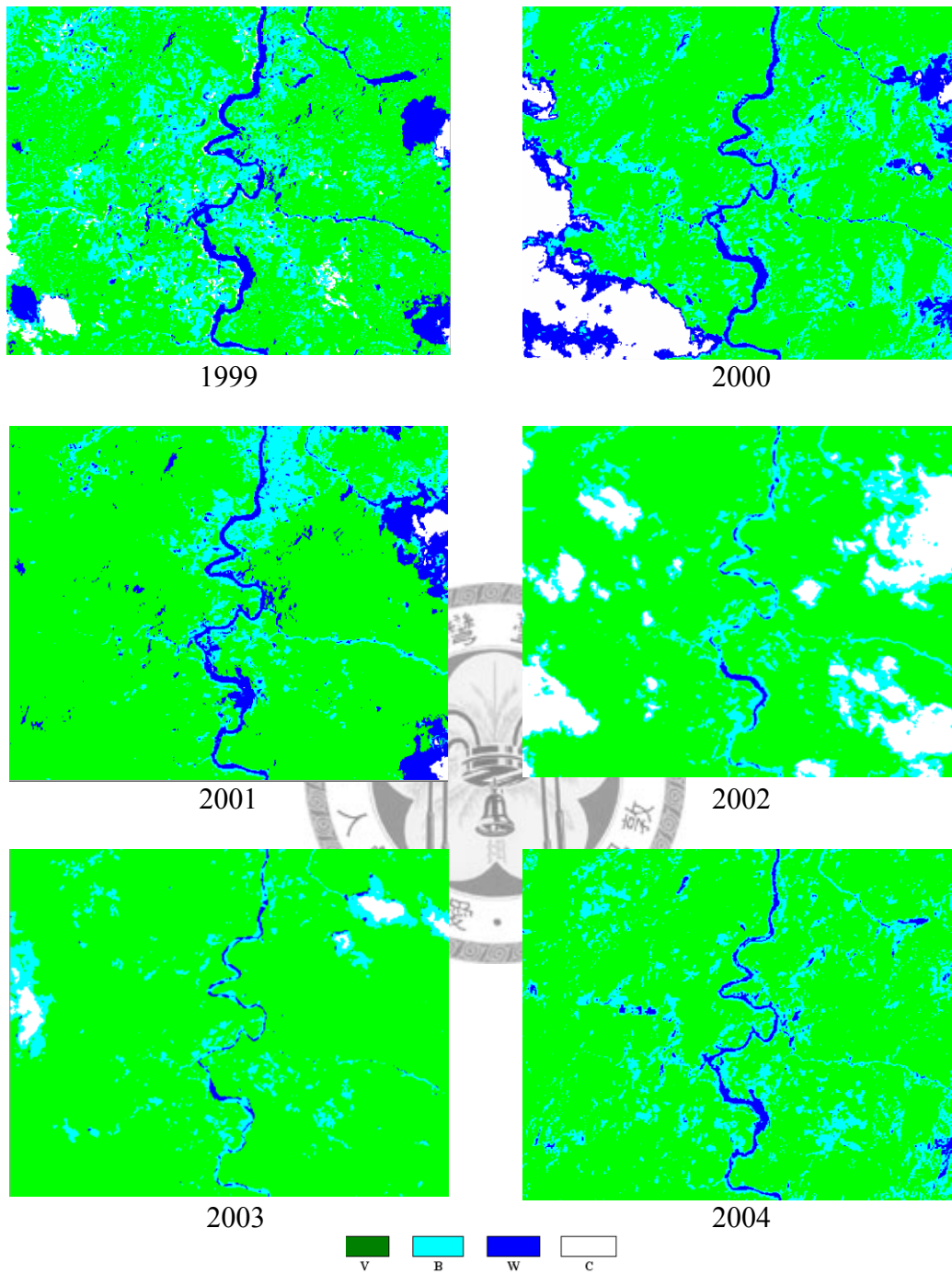


Figure 4-8 Classified SPOT image of the study area from 1999 to 2004 (V: vegetation, B: built-up and bare soil; W: water bodies; C: cloud).

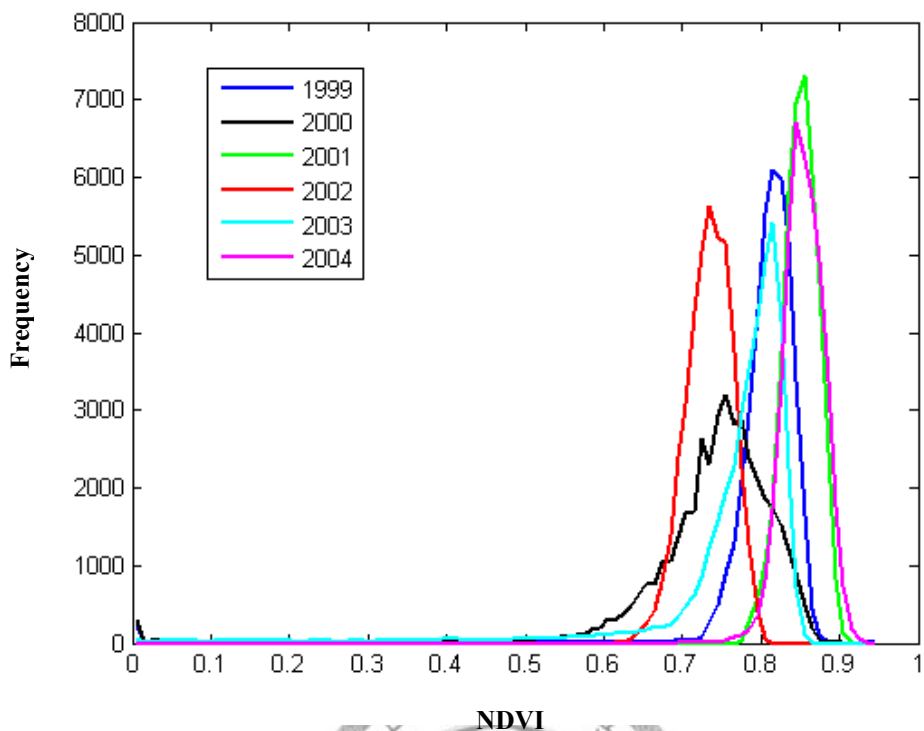


Figure 4-9 NDVI histograms of the six years.

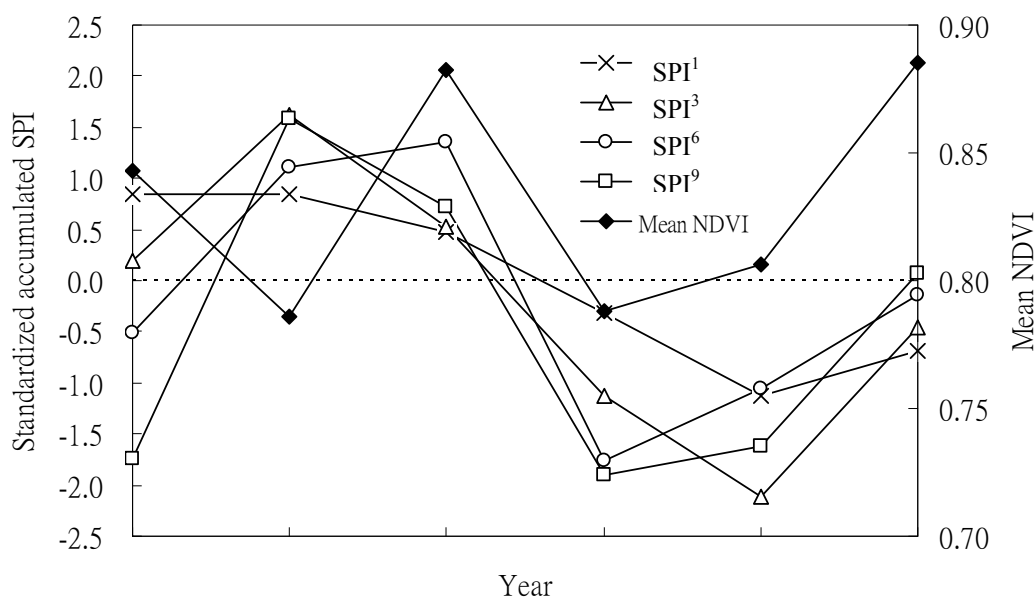


Figure 4-10 Trends of mean NDVI and cumulative SPI values. (SPI<sup>n</sup> represent the accumulated n's 10-day period before the date when SPOT images are taken. E.g. SPI<sup>1</sup> represent the SPI of the 10-day period that when SPOT images are taken)

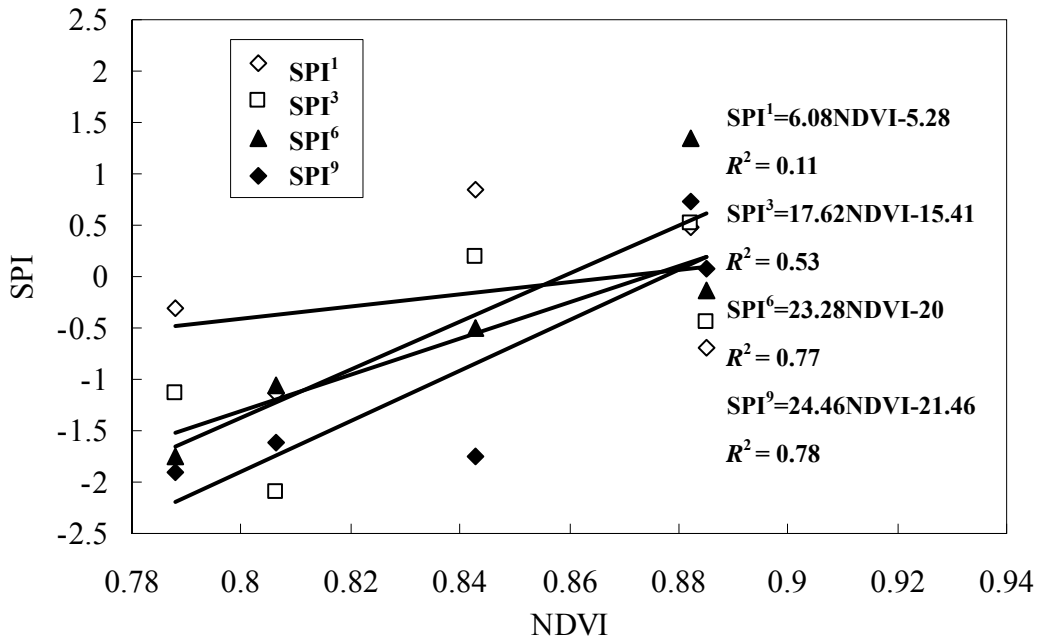


Figure 4-11 Mean NDVI and cumulative SPI values (Exclude year 2000).



Table 4-3 Drought classification by SPI and NDVI (The last column represents the corresponding probabilities and the summation is 50%).

SPI value	NDVI value	Category	Probability %
0 to -0.99	0.877 to 0.837	Mild drought	34.1
-1.0 to -1.49	0.836 to 0.816	Moderate drought	9.2
-1.5 to -1.99	0.816 to 0.796	Severe drought	4.4
-2 or less	0.796 or less	Extreme drought	2.3



where  $NDVI_N$  represents the NDVI value derived from the NOAA-AVHRR image,  $\overline{NDVI}_S$  is the NDVI value derived from the filtered SPOT image, and  $N$  is sample size.

The filtered NDVI value derived from a SPOT image is composed of pixels that may be classified as built-up or vegetation within the filter window. In the selected SPOT image (Figure 4-12(a)), 98% of the pixels are covered by vegetation and built-up areas, thus only 2% represent water. We show that the coverage ratios of vegetated and built-up areas within the corresponding AVHRR pixels are highly-correlated to the filtered NDVI value derived from the SPOT image (Figure 4-14). The relationships between the filtered NDVI value and the coverage ratios of vegetation and built-up areas are modeled as follows:

$$\overline{NDVI}_S = 0.075 + 0.73CR_V \quad (R^2 = 0.94) \quad (4-15)$$

$$\overline{NDVI}_S = 0.798 - 0.745CR_B \quad (R^2 = 0.91) \quad (4-16)$$

where  $CR_V$  and  $CR_B$  are the coverage ratios of vegetation and built-up area, respectively.

#### 4.4.3 Using AVHRR images for drought assessment

The drought event we discuss in this part is the drought of 2002, which is compared with the non-drought (or wet) year 2004. The AVHRR images applied in this part are preprocessed using the cloud screening procedure proposed in this study. Basically, at least one image is selected for each month. However, the cloud cover rate is extremely high during typhoon season, July to October in Taiwan. Therefore, there is no cloudless image from September to October in 2004 to be selected in this study.

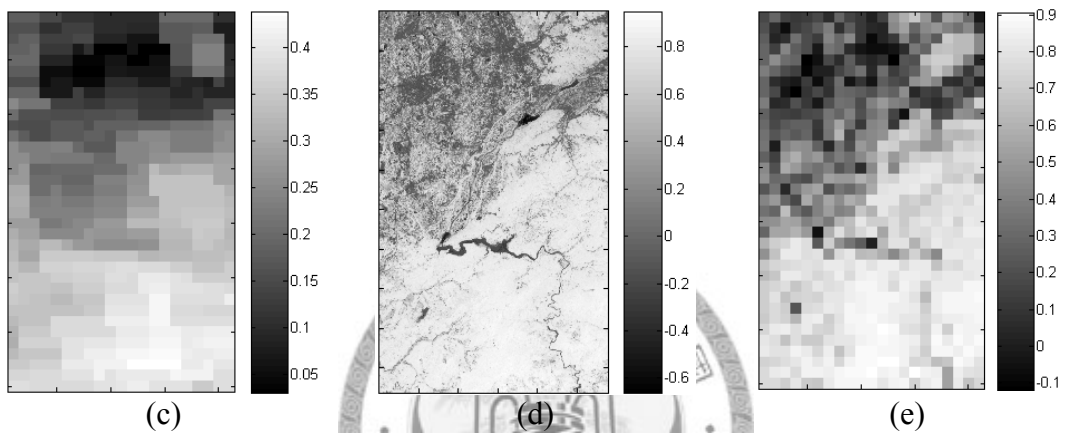
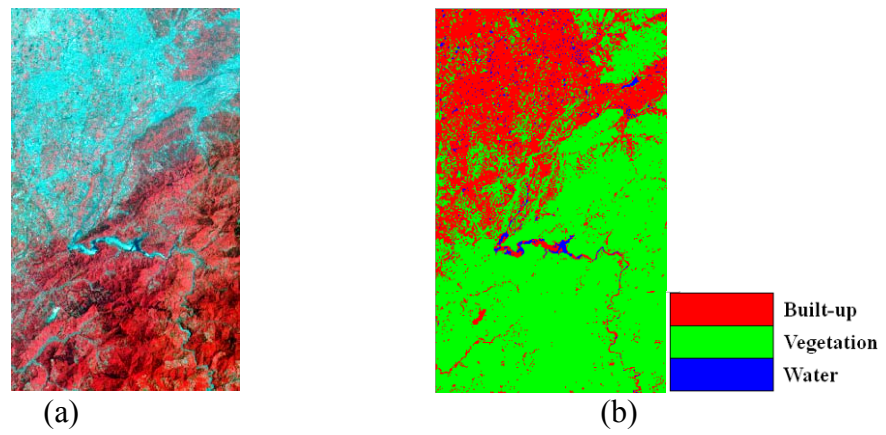


Figure 4-12 Comparison of SPOT and AVHRR images (a) SPOT false-color image, (b) classified SPOT image, (c) NDVI map derived from AVHRR, (d) NDVI map derived from SPOT, (e) filtered NDVI map derived from SPOT.



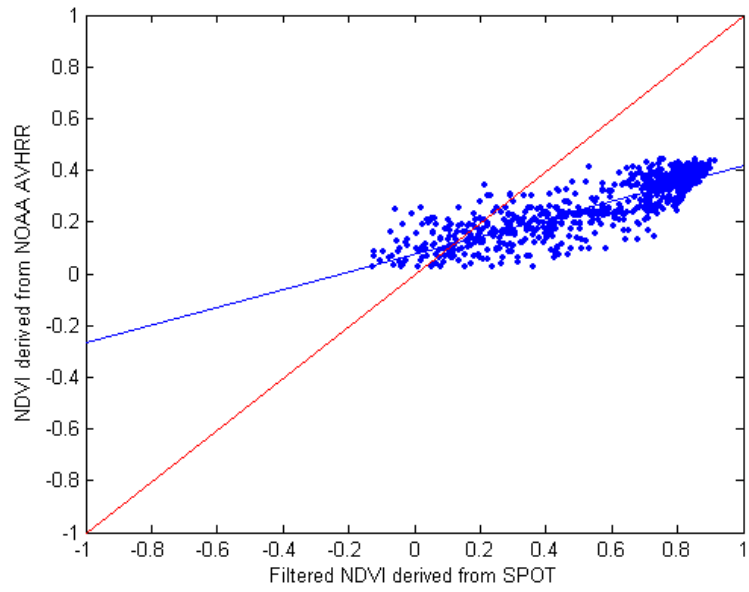


Figure 4-13 The regression result of NDVI values derived from AVHRR images and filtered SPOT images.

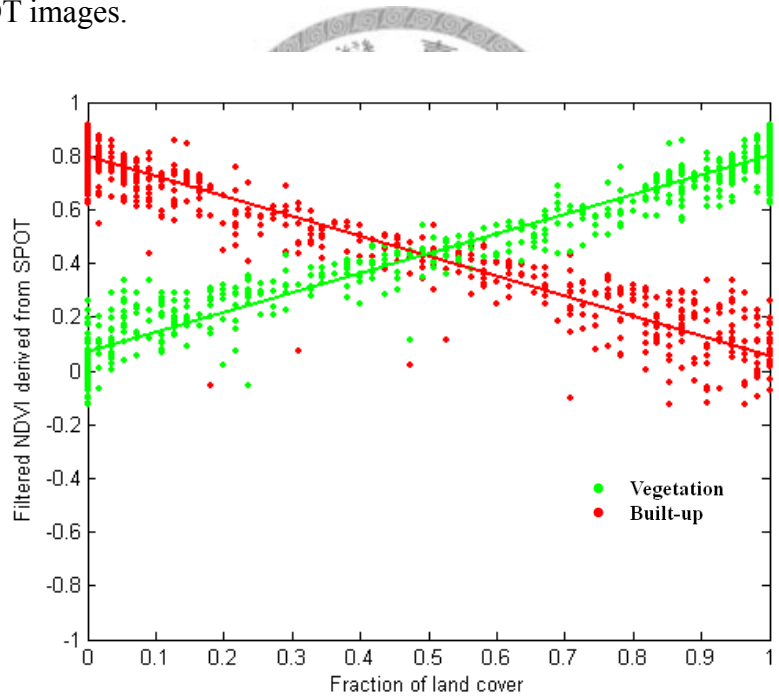


Figure 4-14 Relationships between the NDVI value and the coverage ratios of vegetation and built-up areas.

The cloud-filtered AVHRR images of the study area, the upstream area of the Shihmen reservoirs, are extracted and plotted in VI-Ts space. In order to compare the difference between the drought year (year 2002) and a non-drought year (year 2004), the plots for each month, except September and October 2004, are shown in Figure 4-15. Readers are reminded that year 2002 is considered a drought year according to the SPI result, while 2004 is considered a non-drought year. In VI-Ts diagrams, the vegetation under water stress usually reveals a high surface temperature and low vegetation index value. However, in Figure 4-15, the variation of the drought year in the VI-Ts diagram, during the dry season from January to May, does not show the expected pattern. From February to April in 2002, the SPI result indicates that the drought is getting more severe. As a result, the surface temperatures from February to April of 2002 are generally higher than in 2004. However, the NDVI does not decrease simultaneously. In May, data availability is limited due to cloud cover; there is no significant information shown in the VI-Ts space. The NDVI value in June of 2004 reaches the maximum for the year. For July, the VI-Ts distributions in 2002 and 2004 completely overlap one another. The reason for this may be that July is usually the start of the wet season in Taiwan. As a result, the drought effects on vegetation disappear. From August to October 2002, cloud free images are unavailable due to the high cloud cover rate.

In short, the dynamics of vegetation in VI-Ts space are not easily identified by comparison between drought and non-drought years for any single month. However, the dynamics of vegetation in VI-Ts space in single year may reveal some information for assessing the vegetation growing conditions. Mean values of NDVI and Ts are used to represent the average vegetation growing conditions in a single month. Figure 4-16 and Figure 4-17, respectively, show that the mean values in VI-Ts space vary

over the twelve months of year 2002 and 2004. In Figure 4-16 and Figure 4-17, the NDVI values from January to February form a group at the lower right corner (point A) of VI-Ts space. From March or April to May, while the weather is getting warmer the average temperature rises. In addition, this period is within the dry season in Taiwan. Therefore, once rainfall amount that is lower than the normal level may be reflected as a decrease of the NDVI. As shown in Figure 4-16 and Figure 4-17, the mean values of vegetation dynamics from April and May move to the upper left corner (point B). From June to October, the weather remains warm and wet. During this period, the mean surface temperature remains high and increases the mean NDVI value. As a result, vegetation dynamics move to the upper right corner (point C). After October, surface temperatures decrease due to the cold weather. Meanwhile, the vegetation growing condition usually does not decrease significantly. As a result, the mean point of NDVI and Ts returns back to point A. However, residual cloud present in the study will reduce the NDVI dramatically. Thus, some points, such as February, May, and October 2002 and May and August 2004 have lower NDVI values than expected. In contrast, the average surface temperatures show a very stable pattern and properly reflect their seasonal effect on the growing conditions of the vegetation.

Based on the result, an assumption is proposed in this study, which is that the dynamics of the vegetation growing conditions in VI-Ts space reveal a triangle shape (formed by points A, B, and C). The shape and location of the triangle in VI-Ts space may vary with drought conditions. The effects of drought on vegetation, resulting in higher temperature and lower NDVI values, are well known; these are reflected in the triangle. Therefore, the diagram proposed by (Lambin and Ehrlich, 1995) can be upgraded, as shown in Figure 4-18. In a wet and cold season, the main distributions of vegetation growing condition tend to be located at point A. When a dry and warm

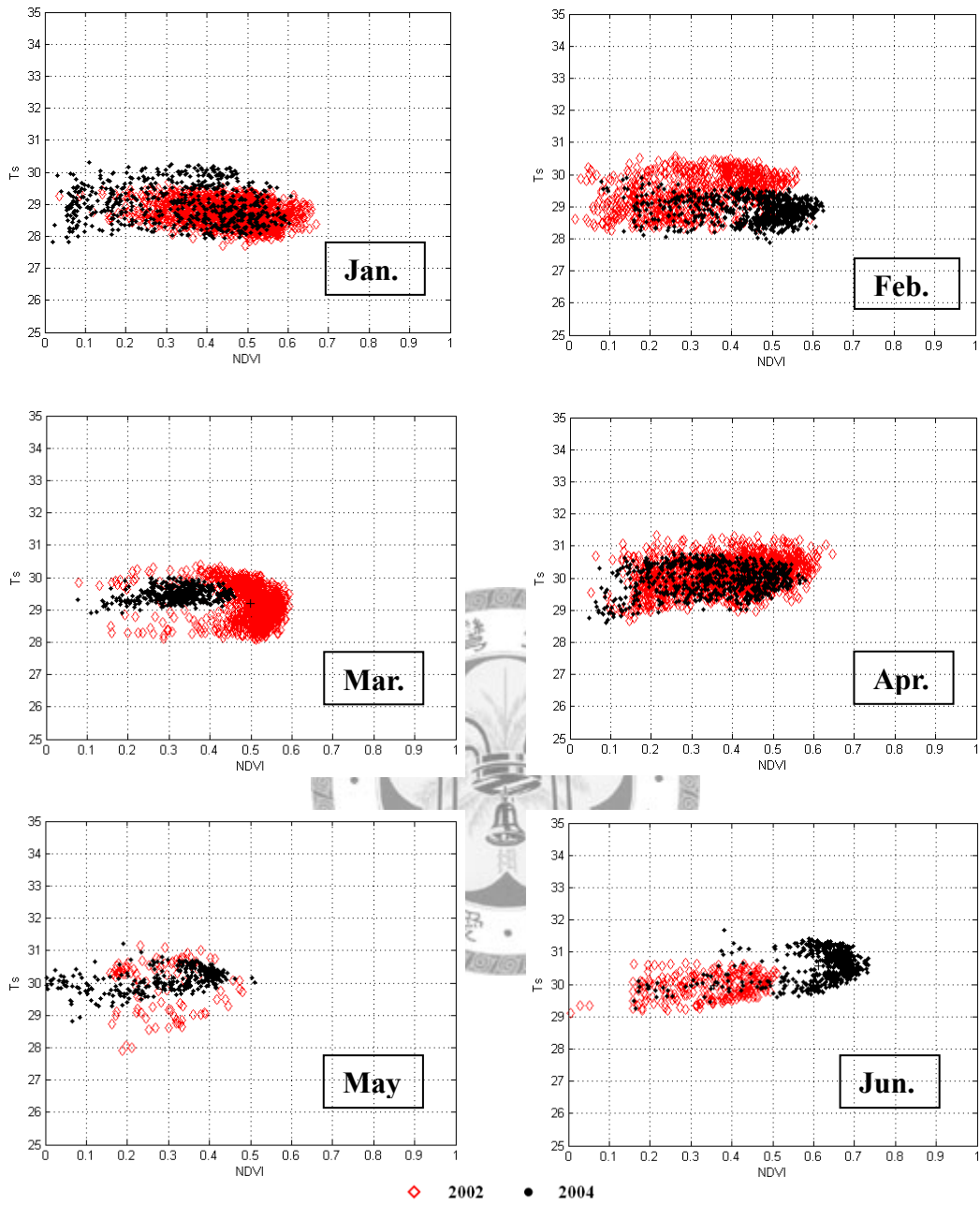


Figure 4-15 Comparison of drought year and non-drought year for 12 months.

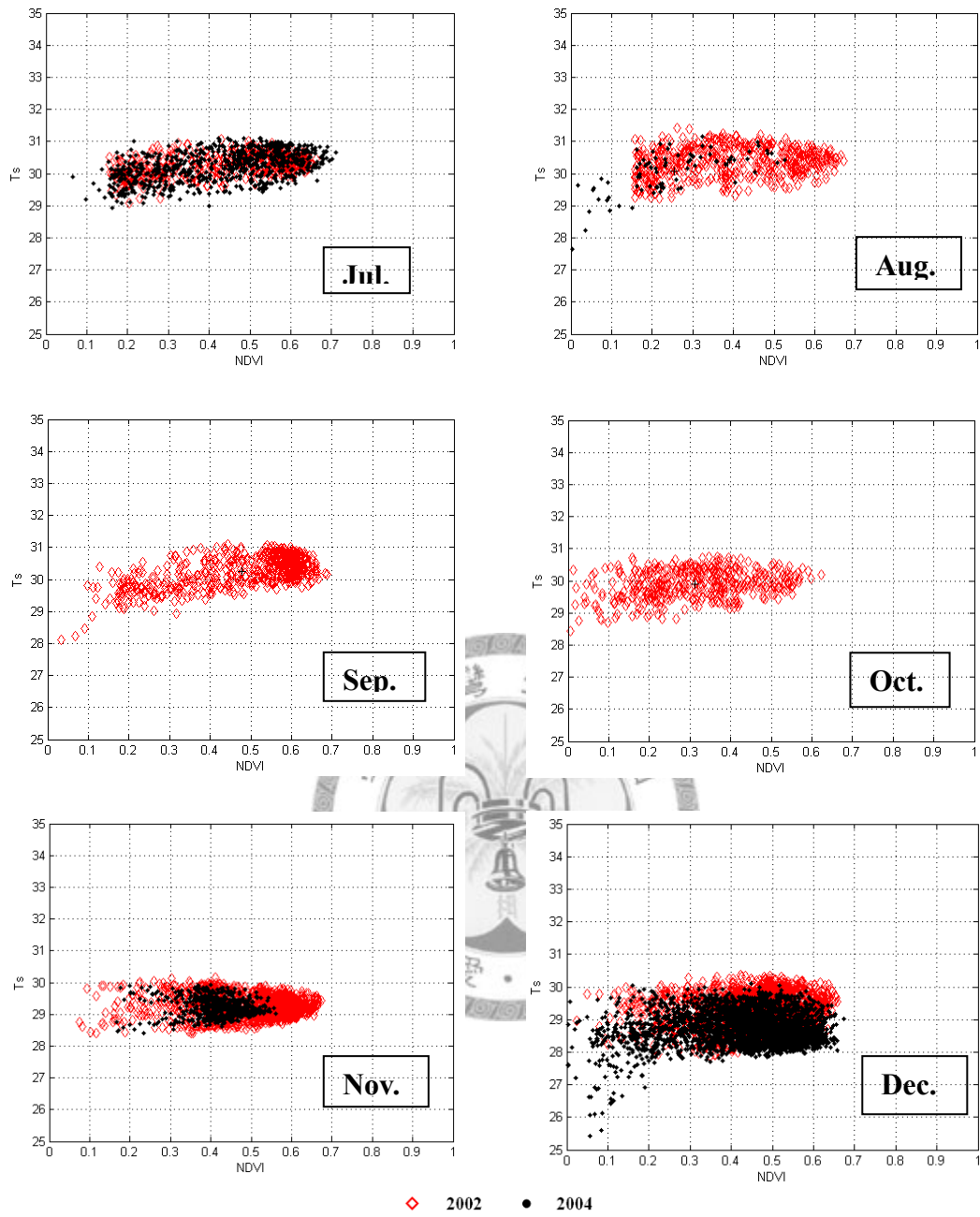


Figure 4-15 Comparison of drought year and non-drought year for 12 months (Continued).

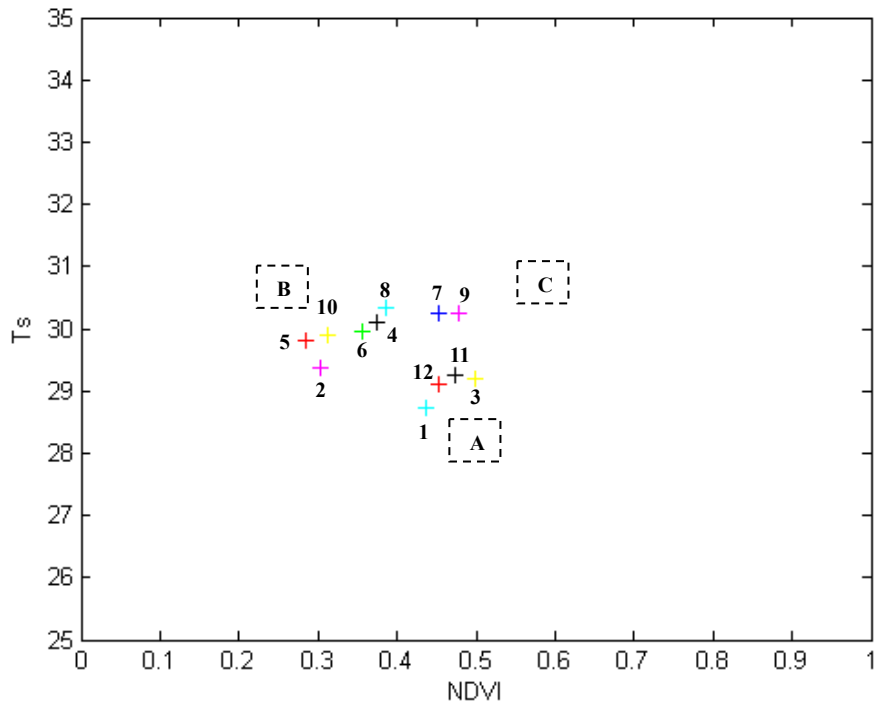


Figure 4-16 Vegetation dynamics of 2002 in VI-Ts space.

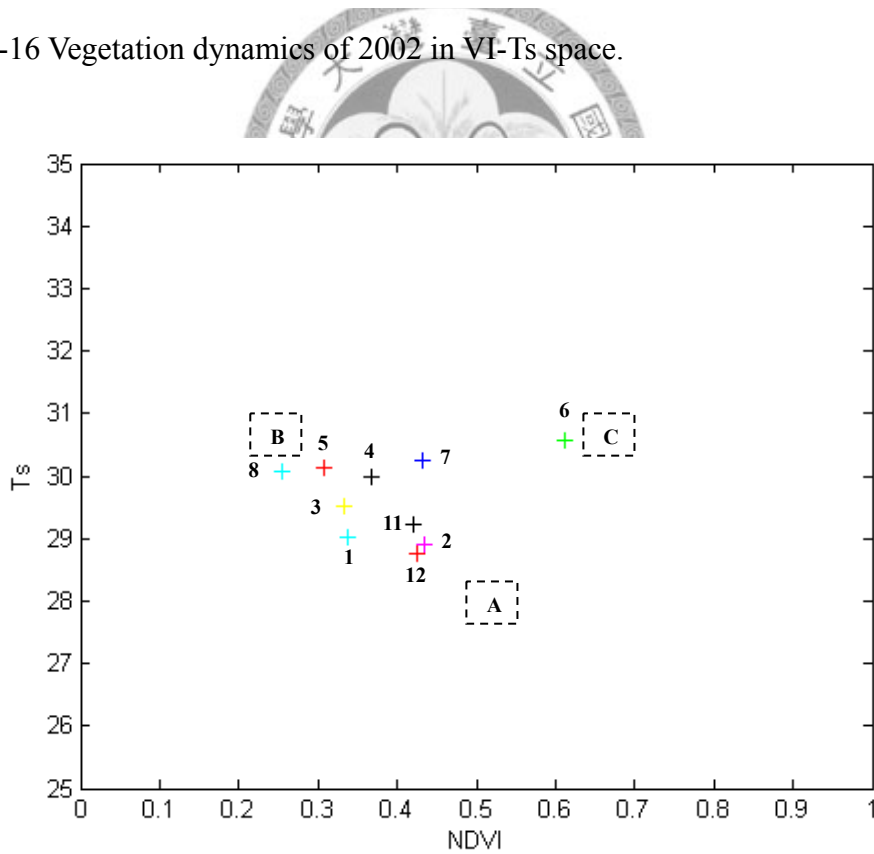


Figure 4-17 Vegetation dynamics of 2004 in VI-Ts space.

season comes, the distribution moves to point B due to the increased temperature and the water stress of vegetation. During a wet and warm season, which is a vegetation growing season, the vegetation dynamics moves to point C. With another wet and cold season, the trend of the vegetation dynamics forms a triangular cycle. With the prior knowledge of biophysical characteristics of vegetation during a drought event, high temperature and low vegetation index value, the triangular cycle is assumed to move from the lower right corner to the upper left corner. However, the AVHRR data used in Figure 4-16 and Figure 4-17 do not show a clear pattern that supports this assumption. Therefore, more data are needed in the future to validate this assumption and quantify drought severity.

#### 4.5 Conclusions

In this study, we classified drought severity into four classes using NDVI values derived from SPOT images. The relationship between NDVI values derived from SPOT images and AVHRR images was also discussed. The AVHRR images for 2002 and 2004 were used to assess the dynamics of vegetation growing conditions in VI-Ts space. A new concept to assess drought conditions in VI-Ts space was proposed to upgrade the previous concept of the VI-Ts diagram. A few concluding remarks are made, as follows.

- (1) From a meteorological perspective, the SPI value at the GaoYi station in the upstream basin of the Shihmen reservoir shows that 2002 was a drought year, and the rest of the years, from 1999 to 2004, can be considered non-drought (or wet) years.
- (2) The NDVI value distributions in the upstream basin of the Shihmen reservoir which were derived from SPOT images, taken in each May from 1999 to 2004,

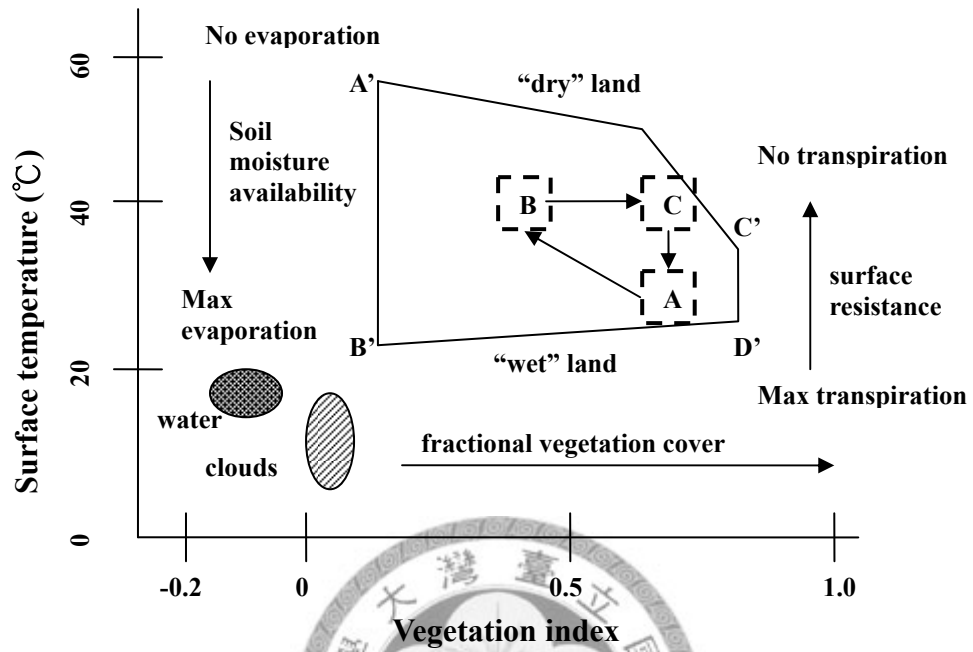


Figure 4-18 An upgraded version of the schematic plot of VI-Ts space.



are applied for classification of drought severity. The relationship between the standardized cumulative SPI and the average NDVI is most significant when the cumulative period is three months. The drought categories by NDVI are proposed which is corresponding to the drought categories by SPI original proposed by McKee (1993).

(3) A linear relationship between the NDVI values derived from filtered SPOT images and AVHRR images is proposed in this study. This linear relationship may be applied for comparative purposes in vegetation studies using multi-resolution images. The relationships between the NDVI derived from filtered SPOT images and the land coverage ratio are also illustrated in this study.

(4) By comparing the dynamics of vegetation of 2002 and 2004 in VI-Ts space, the facts higher temperatures and lower vegetation indices were shown in the VI-Ts space. Based on the result, an assumption is proposed in this study, which is that the dynamics of vegetation growing conditions in VI-Ts space reveals a triangle shape (formed by points A, B, and C). The shape and location of the triangle in the VI-Ts space may vary with the drought condition. An upgrade of the concept of the VI-Ts diagram (Figure 4-6) has also been proposed in this study. However, more data are needed to validate the assumption and quantify drought severity in the future.

## References

- Chung, Y. L., Chen, C.T., Hsi, C.N., Liu, S.M. (2005). Study of MODIS imager band extraction applied to drought monitoring. *Taiwan Journal of Forest Science*, 20(3), 239-247.
- Gallo, K. P., McNab, A. L., Karl, T. R., Brown, J. F., Hood, J. J., Tarpley, J. D. (1993). The Use of NOAA AVHRR Data for Assessment of the Urban Heat-Island Effect. *Journal of Applied Meteorology*, 32(5), 899-908.

- Gitelson, A. A. and Merzlyak, M. N. (1997). Remote estimation of chlorophyll content in higher plant leaves. *International Journal of Remote Sensing*, 18(12), 2691-2697.
- Idso, S. B. (1982). Non-water-stress baselines: A key to measuring and interpreting plant water stress. *Agricultural Meteorology*, 27, 59-70.
- Idso, S. B., Jackson, R. D., Reginato, R. J. (1977). Remote-Sensing of Crop Yields. *Science*, 196(4285), 19-25.
- Jupp, D. L. B., Tian, G., McVicar, T.R., Qin, Y., Li, F. (1998). *Monitoring soil moisture and drought using AVHRR satellite data I: Theory*. CSIRO Earth Observation Centre Technique Report. Canberra. 98.1.
- Kogan, F. N. (1995). Application of vegetation index and brightness temperature for drought detection. *Advances in Space Research*, 15(11), 91-100.
- Kogan, F. N. (1995). Droughts of the late 1980s in the United States as derived from NOAA polar-orbiting satellite data. *Bulletin of the American Meteorological Society*, 76(5), 655-668.
- Kogan, F. N. (1997). Global drought watch from Space. *Bulletin of the American Meteorological Society*, 78(4), 621-636.
- Kogan, F. N. (1998a). Global drought and flood-watch from NOAA polar-orbiting satellites. *Advances in Space Research*, 21(3), 477-480.
- Kogan, F. N. (1998b). A typical pattern of vegetation conditions in southern Africa during El Niño years detected from AVHRR data using three-channel numerical index. *International Journal of Remote Sensing*, 19(18), 3689-3695.
- Kogan, F. N. (2000). *Contribution of remote sensing to drought early warning*. Early Warning Systems for Drought Preparedness and Drought Management, Proceedings, (1037), 75-87.
- Lana, X. S., C., and Beugueño, A. (2001). Patterns of monthly rainfall shortage and excess in terms of the standardized precipitation index. *International Journal of Climatology*, 21, 1669-1691.
- Lin, C. Y. (2007). *Study on drought variability and frequency in Taiwan*. Master Thesis of Department of hydraulic & Ocean Engineering. Tainan, National Cheng Kung University.
- Liu, Q. Y. (1994). *Study on drought lead time prediction*. Master Thesis of Department

of Agricultural Engineering. Taipei, National Taiwan University.

- McKee, T. B., Doesken, N.J., and Kleist, J. (1993). *The relationship of drought frequency and duration to time scales*. Eighth Conference on Applied Climatology. Anaheim, California.
- McVicar, T. R., and Jupp, D.L.B., Yang, X., Tian, G. (1992). *Linking regional water balance models with remote sensing*. In Proceedings of the 13th Asian Conference on Remote Sensing. Ulaanbaatar, Mongolia: B6.1-B6.6.
- McVicar, T. R., and Jupp, D.L.B. (1998). The current and potential operational uses of remote sensing to aid decisions on drought exceptional circumstances in Australia: A review. *Agricultural Systems*, 57(3), 399-468.
- Moran, M. S., Clarke, T.R., Inoue, Y., Vidal, A. (1994). Estimating crop water deficit using the relation between surface-air temperature and spectral vegetation index. *Remote sensing of environment*, 49, 246-263.
- Nemani, R., Pierce, L., Running, S., Goward, S. (1993). Developing satellite-derived estimates of surface moisture status. *Journal of Applied Meteorology*, 32, 548-557.
- Price, J. C. (1990). Using spatial context in satellite data to infer regional scale evapotranspiration. *IEEE transactions on geoscience and remote sensing*, 28(5), 940-948.
- Saunders, R. W., and Kriebel, K.T. (1988). An improved method for detection clear sky and cloudy radiances from AVHRR data. *International Journal of Remote Sensing*, 9(1), 123-150.
- Su, Y. F. (2004). *Remote sensing monitoring of paddy water stress*. Master Thesis of Department of Harbor and River Engineering Keelung, National Taiwan Ocean University.
- Unganai, L. S., and Kogan, F.N. (1998). Southern Africa's recent droughts from Space. *Advances in Space Research*, 21(3), 507-511.
- Unganai, L. S., and Kogan, F.N. (1998). Drought monitoring and corn yield estimation in southern Africa from AVHRR data. *Remote sensing of environment*, 63(2), 219-232.
- Welch, R. M., Sengupta, S.K., and Chen, D.W. (1988). Cloud field classification based upon high spatial resolution textural features 1. Gray level co-occurrence matrix approach. *Journal of geophysical research*, 93(D10), 12663-12681.

## Chapter 5 Summary and future work

In this dissertation, we utilized various remote sensing techniques to extract information from remotely-sensed electromagnetic signal. These techniques include retrieval of surface reflectance, surface temperature estimation using Split Window Technique, landcover type classification by maximum likelihood classifier and cloud screening with texture variable and cloud top temperature. For most of remote sensing applications, remote sensing techniques cooperate with statistical method and digital image process techniques to monitor and assess natural resources.

In the dissertation, water quality, air temperature and drought effect on forest were monitored and assessed using multisensor images. For water quality study, we thought that the water surface reflectance, instead of at-sensor signal, is better to construct the water quality estimation model. Natural water body is a mixture of water and other constituents including suspended solids, dissolved organic matters, zooplankton, etc. These constituents affect the water surface reflectance in different wavelengths. The wavelength-dependent combined effect of individual constituents on the sea surface reflectance does not be taken into consideration in conventional univariate model. Therefore, the multivariate water quality model was proposed in this study. The multivariate model not only keeps the physical properties of natural water but also yields more accurate water quality estimation results.

In Chapter three, we reviewed the details of surface temperature estimation method, split window technique, and the relationship between surface and air temperatures. Multi-sensor images, SPOT and AVHRR, were utilized to assess the effect of landcover type changes on ambient air temperature within 1.21 km square area. A new method for assessment of landcover effect on ambient air temperature using remote

sensing images is proposed in this study. The proposed method takes into consideration the existing local landcover pattern and successfully applied in northern Taiwan. The proposed method enable decision maker to set scenarios of landcover changes and yield the resultant changing of ambient air temperature.

In chapter four we utilized SPOT and AVHRR images to assess drought effect on forest. The SPI was used to describe the precipitation anomalies and quantify drought condition. The relationship between the standardized cumulative SPI and the forest average NDVI, in May, was most significant when the cumulative period is three months. The drought categories result from NDVI values are corresponding to the drought categories result from the SPI originally was proposed by McKee in 1993. The linear relationship between the NDVI values derived from filtered SPOT image and AVHRR image was also presented. By comparing the dynamics of vegetation of year 2002 and year 2004 in VI-Ts space using AVHRR data, the facts of that the higher temperature and lower vegetation index were shown in the VI-Ts space. An assumption was suggested that the dynamics of vegetation grown condition in VI-Ts space reveals a triangle shape (form by point A, B, and C in Figure 4-18). The shape and location of the triangle in VI-Ts space may vary with drought condition. However, more data were needed to validate the assumption and quantify drought severity. Drought monitoring is always a tough job for scientists and needs continual effort to realize and monitor drought phenomenon.

## 簡歷

蘇元風

Email address: [d93622004@ntu.edu.tw](mailto:d93622004@ntu.edu.tw)

### 學歷

- 臺灣大學 生物環境系統工程學系 博士(2004年9月~2009年1月)
- 海洋大學 河海工程學系 碩士(2002年9月~2004年6月)
- 海洋大學 河海工程學系 學士(1998年9月~2002年6月)

### 著作

#### 學位論文

- 博士論文：「衛星遙測應用於環境評估之研究」，2009年1月。(指導教授：鄭克聲博士)
- 碩士論文：「遙測應用於水稻水份逆境監測之研究」，2004年6月。(指導教授：黃文政博士)

#### 期刊論文

1. Su, Y.F., J.J. Liou, J.C. Hou, W.C. Hung, S.M. Hsu, Y.T. Lien, M.D. Su, K.S. Cheng, Y.F. Wang, (2008), A multivariate model for coastal water quality mapping using satellite images. *Sensors*, Vol. 8, pp. 6321-6339. (SCI)
2. Cheng, K.S., Y.F. Su, F.T. Kuo, W.C. Hung, J.L. Chiang, (2007), Assessing the effect of landcover on air temperature using remote sensing images – A pilot study in northern Taiwan, *Landscape and Urban Planning*, Vol. 85, pp. 85-96. (SCI)
3. 蘇元風、吳宜珍、蘇明道、鄭克聲，(2008)，SPOT 衛星影像應用於近岸水質推估模式建立與評估，*農業工程學報*(已接受)。
4. 蘇元風、劉俊志、侯如真、洪維均、許淑媚、連以婷、蘇明道、鄭克聲，(2008)，衛星遙測應用於員山子分洪隧道出口海岸水質監測，*農業工程學報*(已接受)。